



University Transportation Research Center - Region 2

# Final Report

## Full-Scale Investigation of Wind-Induced Vibrations of Mast-Arm Traffic Signal Structures

Performing Organization: Rensselaer Polytechnic  
Institute

August 2014



Sponsors: Research and Innovative Technology  
Administration / USDOT (RITA), New York State Department of  
Transportation

## University Transportation Research Center - Region 2

The Region 2 University Transportation Research Center (UTRC) is one of ten original University Transportation Centers established in 1987 by the U.S. Congress. These Centers were established with the recognition that transportation plays a key role in the nation's economy and the quality of life of its citizens. University faculty members provide a critical link in resolving our national and regional transportation problems while training the professionals who address our transportation systems and their customers on a daily basis.

The UTRC was established in order to support research, education and the transfer of technology in the field of transportation. The theme of the Center is "Planning and Managing Regional Transportation Systems in a Changing World." Presently, under the direction of Dr. Camille Kamga, the UTRC represents USDOT Region II, including New York, New Jersey, Puerto Rico and the U.S. Virgin Islands. Functioning as a consortium of twelve major Universities throughout the region, UTRC is located at the CUNY Institute for Transportation Systems at The City College of New York, the lead institution of the consortium. The Center, through its consortium, an Agency-Industry Council and its Director and Staff, supports research, education, and technology transfer under its theme. UTRC's three main goals are:

### Research

The research program objectives are (1) to develop a theme based transportation research program that is responsive to the needs of regional transportation organizations and stakeholders, and (2) to conduct that program in cooperation with the partners. The program includes both studies that are identified with research partners of projects targeted to the theme, and targeted, short-term projects. The program develops competitive proposals, which are evaluated to insure the most responsive UTRC team conducts the work. The research program is responsive to the UTRC theme: "Planning and Managing Regional Transportation Systems in a Changing World." The complex transportation system of transit and infrastructure, and the rapidly changing environment impacts the nation's largest city and metropolitan area. The New York/New Jersey Metropolitan has over 19 million people, 600,000 businesses and 9 million workers. The Region's intermodal and multimodal systems must serve all customers and stakeholders within the region and globally. Under the current grant, the new research projects and the ongoing research projects concentrate the program efforts on the categories of Transportation Systems Performance and Information Infrastructure to provide needed services to the New Jersey Department of Transportation, New York City Department of Transportation, New York Metropolitan Transportation Council, New York State Department of Transportation, and the New York State Energy and Research Development Authority and others, all while enhancing the center's theme.

### Education and Workforce Development

The modern professional must combine the technical skills of engineering and planning with knowledge of economics, environmental science, management, finance, and law as well as negotiation skills, psychology and sociology. And, she/he must be computer literate, wired to the web, and knowledgeable about advances in information technology. UTRC's education and training efforts provide a multidisciplinary program of course work and experiential learning to train students and provide advanced training or retraining of practitioners to plan and manage regional transportation systems. UTRC must meet the need to educate the undergraduate and graduate student with a foundation of transportation fundamentals that allows for solving complex problems in a world much more dynamic than even a decade ago. Simultaneously, the demand for continuing education is growing – either because of professional license requirements or because the workplace demands it – and provides the opportunity to combine State of Practice education with tailored ways of delivering content.

### Technology Transfer

UTRC's Technology Transfer Program goes beyond what might be considered "traditional" technology transfer activities. Its main objectives are (1) to increase the awareness and level of information concerning transportation issues facing Region 2; (2) to improve the knowledge base and approach to problem solving of the region's transportation workforce, from those operating the systems to those at the most senior level of managing the system; and by doing so, to improve the overall professional capability of the transportation workforce; (3) to stimulate discussion and debate concerning the integration of new technologies into our culture, our work and our transportation systems; (4) to provide the more traditional but extremely important job of disseminating research and project reports, studies, analysis and use of tools to the education, research and practicing community both nationally and internationally; and (5) to provide unbiased information and testimony to decision-makers concerning regional transportation issues consistent with the UTRC theme.

**Project No(s):** 55505-01-04

**Project Date:** August 2014

**Project Title:** Full-Scale Investigation of Wind-Induced Vibrations of Mast-Arm Traffic Signal Structures

**Project's Website:**

<http://utrc2.org/research/projects/wind-induced-vibrations-mast-arm-traffic-signal>

**Principal Investigator(s):**

**Dr. Michael O'Rourke**

**Dr. Christopher Letchford**

Rensselaer Polytechnic Institute

**Performing Organization(s):** Rensselaer Polytechnic Institute

**Sponsor(s):**

New York State Department of Transportation (NYSDOT)  
Research and Innovative Technology Administration /  
USDOT (RITA)

To request a hard copy of our final reports, please send us an email at [utrc@utrc2.org](mailto:utrc@utrc2.org)

**Mailing Address:**

University Transportation Research Center  
The City College of New York  
Marshak Hall, Suite 910  
160 Convent Avenue  
New York, NY 10031  
Tel: 212-650-8051  
Fax: 212-650-8374  
Web: [www.utrc2.org](http://www.utrc2.org)

## Board of Directors

The UTRC Board of Directors consists of one or two members from each Consortium school (each school receives two votes regardless of the number of representatives on the board). The Center Director is an ex-officio member of the Board and The Center management team serves as staff to the Board.

### City University of New York

*Dr. Hongmian Gong - Geography*  
*Dr. Neville A. Parker - Civil Engineering*

### Clarkson University

*Dr. Kerop D. Janoyan - Civil Engineering*

### Columbia University

*Dr. Raimondo Betti - Civil Engineering*  
*Dr. Elliott Sclar - Urban and Regional Planning*

### Cornell University

*Dr. Huaizhu (Oliver) Gao - Civil Engineering*  
*Dr. Mark A. Turnquist - Civil Engineering*

### Hofstra University

*Dr. Jean-Paul Rodrigue - Global Studies and Geography*

### Manhattan College

*Dr. Anirban De - Civil & Environmental Engineering*  
*Dominic Esposito - Research Administration*

### New Jersey Institute of Technology

*Dr. Steven Chien - Civil Engineering*  
*Dr. Jyoung Lee - Civil & Environmental Engineering*

### New York Institute of Technology

*Dr. Nada Marie Anid - Engineering & Computing Sciences*  
*Dr. Marta Panero - Engineering & Computing Sciences*

### New York University

*Dr. Mitchell L. Moss - Urban Policy and Planning*  
*Dr. Rae Zimmerman - Planning and Public Administration*

### Polytechnic Institute of NYU

*Dr. John C. Falcocchio - Civil Engineering*  
*Dr. Kaan Ozbay - Civil Engineering*

### Rensselaer Polytechnic Institute

*Dr. José Holguín-Veras - Civil Engineering*  
*Dr. William "Al" Wallace - Systems Engineering*

### Rochester Institute of Technology

*Dr. J. Scott Hawker - Software Engineering*  
*Dr. James Winebrake - Science, Technology, & Society/Public Policy*

### Rowan University

*Dr. Yusuf Mehta - Civil Engineering*  
*Dr. Beena Sukumaran - Civil Engineering*

### Rutgers University

*Dr. Robert Noland - Planning and Public Policy*

### State University of New York

*Michael M. Fancher - Nanoscience*  
*Dr. Catherine T. Lawson - City & Regional Planning*  
*Dr. Adel W. Sadek - Transportation Systems Engineering*  
*Dr. Shmuel Yahalom - Economics*

### Stevens Institute of Technology

*Dr. Sophia Hassiotis - Civil Engineering*  
*Dr. Thomas H. Wakeman III - Civil Engineering*

### Syracuse University

*Dr. Riyad S. Aboutaha - Civil Engineering*  
*Dr. O. Sam Salem - Construction Engineering and Management*

### The College of New Jersey

*Dr. Thomas M. Brennan Jr. - Civil Engineering*

### University of Puerto Rico - Mayagüez

*Dr. Ismael Pagán-Trinidad - Civil Engineering*  
*Dr. Didier M. Valdés-Díaz - Civil Engineering*

## UTRC Consortium Universities

The following universities/colleges are members of the UTRC consortium.

City University of New York (CUNY)  
Clarkson University (Clarkson)  
Columbia University (Columbia)  
Cornell University (Cornell)  
Hofstra University (Hofstra)  
Manhattan College  
New Jersey Institute of Technology (NJIT)  
New York Institute of Technology (NYIT)  
New York University (NYU)  
Polytechnic Institute of NYU (Poly)  
Rensselaer Polytechnic Institute (RPI)  
Rochester Institute of Technology (RIT)  
Rowan University (Rowan)  
Rutgers University (Rutgers)\*  
State University of New York (SUNY)  
Stevens Institute of Technology (Stevens)  
Syracuse University (SU)  
The College of New Jersey (TCNJ)  
University of Puerto Rico - Mayagüez (UPRM)

*\* Member under SAFETEA-LU Legislation*

## UTRC Key Staff

**Dr. Camille Kamga:** *Director, UTRC*  
*Assistant Professor of Civil Engineering, CCNY*

**Dr. Robert E. Paaswell:** *Director Emeritus of UTRC and Distinguished Professor of Civil Engineering, The City College of New York*

**Herbert Levinson:** *UTRC Icon Mentor, Transportation Consultant and Professor Emeritus of Transportation*

**Dr. Ellen Thorson:** *Senior Research Fellow, University Transportation Research Center*

**Penny Eickemeyer:** *Associate Director for Research, UTRC*

**Dr. Alison Conway:** *Associate Director for New Initiatives and Assistant Professor of Civil Engineering*

**Nadia Aslam:** *Assistant Director for Technology Transfer*

**Dr. Anil Yazici:** *Post-doc/ Senior Researcher*

**Nathalie Martinez:** *Research Associate/Budget Analyst*

# Full-Scale Investigation of Wind-Induced Vibrations of Mast-Arm Traffic Signal Structures



by

Hung Nguyen Sinh, Michelle Riedman

Dr. Christopher Letchford, Dr. Michael O'Rourke

August 2014



1. Report No. C-10-07		2. Government Accession No.		3. Recipient's Catalog No.	
4. Title and Subtitle Full-Scale Investigation of Wind-Induced Vibrations of Mast-Arm Traffic Signal Structures				5. Report Date August 2014	
				6. Performing Organization Code	
7. Author(s) Michael O'Rourke Chris Letchford				8. Performing Organization Report No.	
9. Performing Organization Name and Address  Rensselaer Polytechnic Institute Civil and Environmental Engineering 110 8 <sup>th</sup> Street Troy, NY 12180				10. Work Unit No.	
				11. Contract or Grant No. 1111 0000	
12. Sponsoring Agency Name and Address NYS Department of Transportation 50 Wolf Road Albany, New York 12232				13. Type of Report and Period Covered	
				14. Sponsoring Agency Code	
15. Supplementary Notes Project funded in part with funds from the Federal Highway Administration					
16. Abstract Because of their inherent flexibility and low damping ratios, cantilevered mast-arm traffic signal structures are susceptible to wind-induced vibrations. These vibrations cause structural stresses and strains to develop in a cyclical fashion which can lead to reduced service life due to fatigue and, in extreme cases, full collapse. In 2001, after the collapse of several of these structures throughout the United States, American Association of State Highway and Transportation Officials (AASHTO) code standards were updated to include fatigue provisions for traffic signal supporting structures. In New York State, there is particular concern regarding structures spanning longer than 14 meters which currently do not meet these updated fatigue provisions. To address this concern, a full-scale experiment was conducted using an existing 25 meter mast-arm traffic signal structure, located in Malta, NY, in which the response of the structure was observed in relation to in-situ wind conditions. In previous studies, high-amplitude vertical vibrations of mast-arm traffic signal structures have been shown to be due to vortex shedding, a phenomenon in which alternately shed, low-pressure vortices induce oscillating forces onto the mast-arm causing a cross-wind response. When the frequency of vortices being shed from the mast-arm corresponds to the natural frequency of the structure, a resonant condition is created. The resonant condition causes the long-lasting, high-amplitude vibrations, which may lead to the fatigue failure of these structures. Turbulence in the approach flow is known to affect the cohesiveness of vortex shedding. Results from this full-scale experiment indicate that the surrounding terrain conditions, which affect the turbulence intensity of the wind, greatly influence the likelihood of occurrence of long-lasting, high-amplitude vibrations and also impact whether reduced service life due to fatigue is likely to be a concern.					
17. Key Words Traffic signal, vibrations, mast arm traffic signal				18. Distribution Statement No restrictions	
19. Security Classif. (of this report) Unclassified		20. Security Classif. (of this page) Unclassified		21. No. of Pages 120	
				22. Price	

**Disclaimer**

The contents of this report reflect the views of the authors, who are responsible for the facts and the accuracy of the information presented herein. The contents do not necessarily reflect the official views or policies of the New York State Department of Transportation, the United States Department of Transportation or the Federal Highway Administration. This report does not constitute a standard, specification or regulation. This document is disseminated under the sponsorship of the Department of Transportation, University Transportation Centers Program, in the interest of information exchange. The U.S. Government and NYSDOT assume no liability for the contents or use thereof.

## **Acknowledgement**

The Rensselaer team would like to gratefully acknowledge the assistance, direction and review comments received from NYSDOT team. Specifically we wish to acknowledge NYSDOT project manager Harry White, as well as Thomas Hoffman, Jonathan Kunin and finally Erica Westhuis. "

Thanks for your help.

# CONTENTS

LIST OF TABLES . . . . .	v
LIST OF FIGURES . . . . .	vi
ABSTRACT . . . . .	x
1. INTRODUCTION . . . . .	1
1.1 Mast-Arm Traffic Signal Structures . . . . .	1
1.2 Research Problem Statement . . . . .	2
1.3 Vortex Shedding . . . . .	3
1.4 Previous Research . . . . .	4
1.5 Research Objective . . . . .	6
1.6 Report Outline . . . . .	6
2. EXPERIMENTAL SETUP . . . . .	8
2.1 Experiment Introduction . . . . .	8
2.1.1 Site Information . . . . .	8
2.1.2 Structure Geometry . . . . .	9
2.2 Instrumentation . . . . .	10
2.2.1 Overview . . . . .	10
2.2.2 Accelerometers . . . . .	10
2.2.3 Anemometer . . . . .	12
2.2.4 Lock-Box and Power Supply . . . . .	14
2.2.5 Data Logger . . . . .	15
2.2.6 Field Computer . . . . .	15
2.2.7 Software . . . . .	15
2.3 Installation . . . . .	16
3. DYNAMIC CHARACTERISTICS . . . . .	18
3.1 Introduction . . . . .	18
3.2 Finite Element Model . . . . .	18
3.2.1 FEM Geometry . . . . .	18
3.2.2 Material Properties . . . . .	19
3.2.3 Mesh Properties . . . . .	19

3.2.4	Traffic Signals . . . . .	21
3.2.5	Boundary Conditions . . . . .	21
3.2.5.1	Longitudinal Bolt Stiffness . . . . .	22
3.2.5.2	Transverse Bolt Stiffness . . . . .	24
3.3	FEM Results . . . . .	26
3.3.1	Natural Frequencies . . . . .	26
3.3.2	Mode Shapes . . . . .	27
3.4	Free Vibration Tests . . . . .	28
3.4.1	Method . . . . .	28
3.4.2	Natural Frequencies . . . . .	28
3.4.3	Damping Ratios . . . . .	29
3.5	Comparison of Results . . . . .	32
3.6	Estimated Critical Wind Speed . . . . .	33
4.	WIND AND VIBRATION DATA . . . . .	34
4.1	Introduction . . . . .	34
4.2	Methodology . . . . .	34
4.2.1	Applying Baseline Correction . . . . .	36
4.2.2	Removing Below Threshold Data . . . . .	37
4.2.3	Removing Erroneous Acceleration Values (Spikes and Zeros) . . . . .	38
4.3	Results . . . . .	39
4.4	Discussion . . . . .	44
4.4.1	Vortex Shedding . . . . .	44
4.4.2	Terrain . . . . .	45
4.4.3	Turbulence Intensity . . . . .	46
4.5	Conclusion . . . . .	48
5.	WIND DATA ANALYSIS . . . . .	50
5.1	Introduction . . . . .	50
5.2	Wind Rose Definition . . . . .	50
5.3	Historical Data . . . . .	51
5.3.1	Site Locations . . . . .	51
5.3.2	Data Validation . . . . .	52
5.3.3	Methodology and Historical Wind Roses . . . . .	53
5.3.4	Fitted Probability Distributions . . . . .	54



5.4	Project Data . . . . .	57
5.4.1	Methodology and Project Wind Roses . . . . .	57
5.4.2	Discussion and Comparison with Historical Data . . . . .	58
6.	MAST-ARM VIBRATION MODEL . . . . .	62
6.1	Introduction . . . . .	62
6.2	Eigenvalue Analysis . . . . .	62
6.3	On Site Vibration "Pluck Test" Method . . . . .	65
6.4	Approximate Energy Method, Rayleigh's Method . . . . .	68
6.5	Conclusion . . . . .	69
7.	FATIGUE LIFE ESTIMATION . . . . .	71
7.1	Introduction . . . . .	71
7.2	Fatigue . . . . .	71
7.3	Stress Range . . . . .	73
7.4	Probability distribution for mast arm tip displacement . . . . .	81
7.5	Fatigue life estimation . . . . .	82
7.6	Conclusion . . . . .	86
	LITERATURE CITED . . . . .	87
	APPENDICES	
A.	NYSDOT PLANS - MALTA, NY MAST-ARM STRUCTURE . . . . .	89
B.	NATURAL FREQUENCY HAND CALCULATIONS . . . . .	93
C.	DYNAMIC CHARACTERISTICS - ADDITIONAL FIGURES . . . . .	96
D.	WIND ROSES USING NCDC DATA . . . . .	102
E.	WIND ROSES USING BEST FIT WEIBULL MODEL . . . . .	106
F.	CIRCULAR AVERAGE FORMULATION . . . . .	110

## LIST OF TABLES

3.1	Material Properties . . . . .	19
3.2	Applied Traffic Signals . . . . .	21
3.3	Longitudinal Bolt Stiffness Parameters . . . . .	24
3.4	Lateral Bolt Stiffness Parameters . . . . .	25
3.5	FEM Natural Frequencies . . . . .	26
3.6	Damping Ratios . . . . .	32
3.7	Natural Frequency Comparison . . . . .	33
5.1	Airport Site Information . . . . .	52
5.2	Anemometer Height Changes . . . . .	52
5.3	Best-fit distribution parameters for each direction . . . . .	56
6.1	Material Properties . . . . .	63
6.2	Applied Traffic Signals . . . . .	65
7.1	Stress Range and Number of cycles Values . . . . .	84
7.2	Number of cycles associating with each stress range . . . . .	85
7.3	Number of cycles associating with each equivalent step . . . . .	85

## LIST OF FIGURES

1.1	Cantilevered Mast-Arm Traffic Signal Structure . . . . .	1
1.2	Mast-Arm Connection Detail . . . . .	2
1.3	Idealized Vortex Shedding Illustration . . . . .	4
2.1	Instrumented Traffic Signal Structure in Malta, NY . . . . .	8
2.2	Project Location Map . . . . .	9
2.3	Instrumentation Layout and Sensor Orientations . . . . .	10
2.4	Installed Accelerometer with Mounting Bracket . . . . .	11
2.5	Mounting Bracket 2 . . . . .	12
2.6	Installed Anemometer . . . . .	13
2.7	Lock Box Setup . . . . .	14
2.8	Installation Photograph . . . . .	17
3.1	FEM Components . . . . .	19
3.2	C3D8R Element . . . . .	20
3.3	FEM Mesh . . . . .	20
3.4	Structural Bolt Detail . . . . .	22
3.5	Constant Frictional Force Along Bolt with Corresponding Linearly Vary- ing Force Profile . . . . .	23
3.6	Bolt Detail with Stress Profile for Lateral Displacement . . . . .	26
3.7	Fundamental Mode of Vibration - Vertical Direction . . . . .	27
3.8	Fundamental Mode of Vibration - Horizontal Direction . . . . .	28
3.9	Pluck Test (Z-Direction, Test 2): Acceleration Time History . . . . .	29
3.10	Pluck Test (Z-Direction, Test 2): Fourier Amplitude Spectrum . . . . .	30
3.11	Pluck Test (Z-direction, Test 2): Overlaid Decay Envelope . . . . .	31
3.12	Pluck Test (Z-direction, Test 2): Y and Z Accelerations . . . . .	32

4.1	Instrumented Traffic Signal Structure in Malta, NY . . . . .	34
4.2	Instrumentation Layout and Sensor Orientations . . . . .	35
4.3	Acceleration Baseline Correction . . . . .	37
4.4	Acceleration Time History Showing Erroneous Readings . . . . .	38
4.5	Vertical Response vs. Wind Speed - Raw Data . . . . .	39
4.6	Vertical Response vs. Wind Speed - Filtered Data . . . . .	40
4.7	Horizontal Response vs. Wind Speed - Raw Data . . . . .	40
4.8	Horizontal Response vs. Wind Speed - Filtered Data . . . . .	41
4.9	Time History Response . . . . .	41
4.10	Vertical Response vs. Perpendicular Wind Speed - Filtered Data . . . .	42
4.11	Horizontal Response vs. Perpendicular Wind Speed - Filtered Data . .	43
4.12	Vertical vs. Horizontal Response at Tip of Mast-Arm . . . . .	45
4.13	Terrain Surrounding Malta, NY Structure . . . . .	46
4.14	Terrain Surrounding Tests at TTU . . . . .	47
4.15	Observed Turbulence Intensity Distribution at Malta, NY . . . . .	48
5.1	Location Map: Sites Used for Wind Analysis . . . . .	51
5.2	Cumulative Probability Distribution Matrix Example . . . . .	53
5.3	Observed Wind Rose for Albany, NY using Historical NCDC Data . . .	54
5.4	Best-Fit Distributions for Albany, NY (All directions included) . . . .	55
5.5	Fitted Wind Rose for Albany, NY using the WB distribution . . . . .	57
5.6	Observed Wind Rose at Malta, NY (0° is Project North) . . . . .	58
5.7	Observed Wind Rose at Malta, NY: 0.5 m/s Wind Speed Increment (0° is Project North) . . . . .	59
5.8	Observed Project Wind Rose Rotated to True North . . . . .	60
5.9	Project Wind Rose Overlaid on Site Map . . . . .	61
6.1	Time History Response: a)Measured horizontal acceleration at mast- arm tip, b)Measured vertical acceleration at mast-arm tip, c)Measured wind speed, d)Measured wind direction . . . . .	63

6.2	Fourier Amplitude Spectrum: a)Mast arm acceleration, b)Wind speed .	64
6.3	Traffic Signal Structure Geometry . . . . .	65
6.4	Excitation Test - Z-direction (Test 2): Acceleration Time History Response . . . . .	66
6.5	Excitation Test - Z-direction (Test 2): Fourier Amplitude Spectrum . .	67
7.1	Stress-number of cycles curves for various connection detail catagories of ASTM A572 Gr 65 Steel (from Kacin, Rizzo, Tajari, 2010) . . . . .	72
7.2	Stress time history . . . . .	73
7.3	Two Load Distributions Considered: a)Uniform Load, b)Point Load . .	74
7.4	Mast-arm Cross Section . . . . .	75
7.5	Fourier Amplitude Spectrum for Mast-arm Acceleration Response . . .	76
7.6	Calculated Tip mast-arm motion for June 26, 2012 Data . . . . .	80
7.7	Inverse CDF method . . . . .	81
7.8	Cumulative Histogram and Cumulative Density Function for tip displacement response . . . . .	82
7.9	Miner's Rule . . . . .	83
A.1	NYSDOT Plans (1 of 3) . . . . .	90
A.2	NYSDOT Plans (2 of 3) . . . . .	91
A.3	NYSDOT Plans (3 of 3) . . . . .	92
B.1	Lambda Values . . . . .	94
C.1	Second Mode of Vibration - Vertical Direction . . . . .	96
C.2	Second Mode of Vibration - Horizontal Direction . . . . .	96
C.3	Third Mode of Vibration - Vertical Direction . . . . .	97
C.4	Pluck Test (Y-Direction, Test 1): Acceleration Time History . . . . .	97
C.5	Pluck Test (Y-Direction, Test 2): Acceleration Time History . . . . .	98
C.6	Pluck Test (Z-Direction, Test 1): Acceleration Time History . . . . .	98
C.7	Pluck Test (Z-Direction, Test 2): Acceleration Time History . . . . .	99
C.8	Pluck Test (Y-Direction, Test 1): Fourier Amplitude Spectrum . . . . .	99



C.9	Pluck Test (Y-Direction, Test 2): Fourier Amplitude Spectrum . . . . .	100
C.10	Pluck Test (Z-Direction, Test 1): Fourier Amplitude Spectrum . . . . .	100
C.11	Pluck Test (Z-Direction, Test 2): Fourier Amplitude Spectrum . . . . .	101
D.1	Observed Wind Rose for Albany, NY . . . . .	102
D.2	Observed Wind Rose for Binghamton, NY . . . . .	102
D.3	Observed Wind Rose for Buffalo, NY . . . . .	103
D.4	Observed Wind Rose for Dutchess, NY . . . . .	103
D.5	Observed Wind Rose for Hartford, CT . . . . .	104
D.6	Observed Wind Rose for Long Island, NY . . . . .	104
D.7	Observed Wind Rose for Portland, ME . . . . .	105
D.8	Observed Wind Rose for Syracuse, NY . . . . .	105
E.1	Model Wind Rose for Albany, NY . . . . .	106
E.2	Model Wind Rose for Binghamton, NY . . . . .	106
E.3	Model Wind Rose for Buffalo, NY . . . . .	107
E.4	Model Wind Rose for Dutchess, NY . . . . .	107
E.5	Model Wind Rose for Hartford, CT . . . . .	108
E.6	Model Wind Rose for Long Island, NY . . . . .	108
E.7	Model Wind Rose for Portland, ME . . . . .	109
E.8	Model Wind Rose for Syracuse, NY . . . . .	109

## ABSTRACT

Because of their inherent flexibility and low damping ratios, cantilevered mast-arm traffic signal structures are susceptible to wind-induced vibrations. These vibrations cause structural stresses and strains to develop in a cyclical fashion which can lead to reduced service life due to fatigue and, in extreme cases, full collapse.

In 2001, after the collapse of several of these structures throughout the United States, American Association of State Highway and Transportation Officials (AASHTO) code standards were updated to include fatigue provisions for traffic signal supporting structures. In New York State, there is particular concern regarding structures spanning longer than 14 meters which currently do not meet these updated fatigue provisions. To address this concern, a full-scale experiment was conducted using an existing 25 meter mast-arm traffic signal structure, located in Malta, NY, in which the response of the structure was observed in relation to in-situ wind conditions.

In previous studies, high-amplitude vertical vibrations of mast-arm traffic signal structures have been shown to be due to vortex shedding, a phenomenon in which alternately shed, low-pressure vortices induce oscillating forces onto the mast-arm causing a cross-wind response. When the frequency of vortices being shed from the mast-arm corresponds to the natural frequency of the structure, a resonant condition is created. The resonant condition causes the long-lasting, high-amplitude vibrations which may lead to the fatigue failure of these structures.

Turbulence in the approach flow is known to affect the cohesiveness of vortex shedding. Results from this full-scale experiment indicate that the surrounding terrain conditions, which affect the turbulence intensity of the wind, greatly influence the likelihood of occurrence of long-lasting, high-amplitude vibrations and also impact whether reduced service life due to fatigue is likely to be a concern.

# CHAPTER 1

## INTRODUCTION

### 1.1 Mast-Arm Traffic Signal Structures

Cantilevered mast-arm traffic signal structures, such as the one shown in Figure 1.1, are commonly used as supports for traffic signals throughout the United States due to their practical and economic design. These structures consist of two primary structural elements: the horizontal element (referred to as the ‘mast-arm’) and the vertical element (referred to as the ‘vertical post’). These elements are typically made from galvanized steel with hollow circular or polygonal cross sections and tapered diameters.



**Figure 1.1: Cantilevered Mast-Arm Traffic Signal Structure [1]**

The mast-arm and vertical post are connected via a ‘mast-arm connection detail’ in which the mast-arm is welded at its end to a set of base plates which are in turn bolted to the vertical post. A typical mast-arm connection detail is shown in

Figure 1.2. Mast-arm traffic signal structures are flexible with fundamental resonant frequencies typically around 1 Hz and have extremely low damping ratios which are often less than 1% of critical damping [2].



**Figure 1.2: Mast-Arm Connection Detail**

## **1.2 Research Problem Statement**

Because of their inherent flexibility, mast-arm traffic signal structures are prone to vibrations under wind loading. As a result of their low damping once these vibrations are initiated, the structures typically undergo a large number of cycles before the vibrations decay. Beyond simply being distracting to passing motorists, these continued vibrations cause structural stresses and strains to occur in a cyclical manner which can reduce the service life of the structure via fatigue.

In some cases, this fatigue can lead to a complete collapse of the mast-arm traffic signal structure. Several such collapses have occurred in recent years including over a dozen in the state of Missouri [3] as well as several others in Wyoming, California, and Texas [4]. Case studies of these types of failures indicate that the failures occurred primarily due to fatigue at the welded connection between the mast-arm and the base plate [5]. The fatigue cracks at the welds were observed to initiate on top of the arms which can be associated with the bending effect of

the mast-arms in the vertical plane. It is also important to note that the failures of these structures do not occur during extreme-event wind conditions [6]. Instead, the failures are due to fatigue crack growth due to the accumulation of damage caused by the wind-induced vibrations.

The failure of several mast-arm structures prompted the inclusion of Section 11 - “Fatigue Design” into the 2001 and later editions of The American Association of State Highway and Transportation Officials (AASHTO) Standard Specifications for Structural Supports for Highway Signs, Luminaires, and Traffic Signals [7]. In this provision, AASHTO requires fatigue design for infinite life in which fatigue stresses must not exceed the allowable constant-amplitude fatigue threshold limits for the structural detail in question.

### **1.3 Vortex Shedding**

A commonly observed mechanism causing the large-amplitude vertical vibrations of mast-arm traffic signal structures is called vortex shedding. Vortex shedding occurs when flow across a bluff body causes low-pressure vortices with alternating directions of rotation (and on opposite sides of the mast-arm) to be shed into the body’s wake [8]. This alternating change in pressure distribution creates oscillating forces on the body perpendicular to the direction of flow causing the body to vibrate in a cross-flow response as illustrated in Figure 1.3. In the case of a mast-arm traffic signal structure, normally horizontal wind flow perpendicular to the length of the mast-arm causes vibration of the mast-arm in the vertical direction. Vortex shedding occurs most coherently when the flow approaching the bluff body is uniform with low turbulence. In contrast, turbulence in the approach flow (i.e variation in wind velocity) results in variation in the shedding frequency even though the strengths of the vortices are maintained [8].



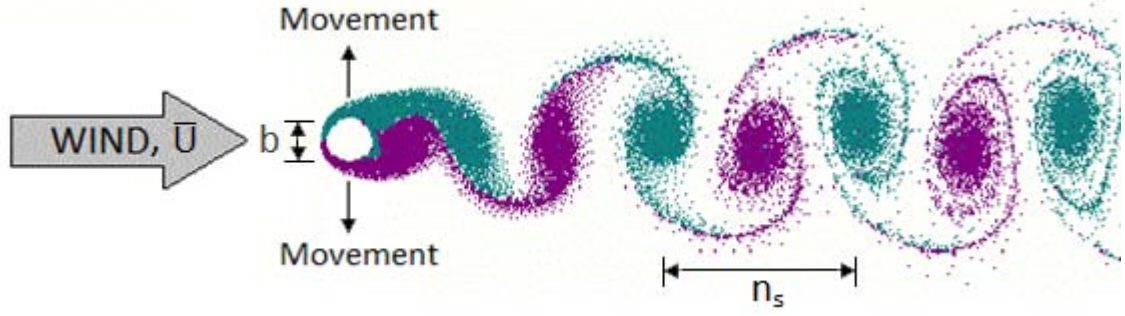


**Figure 1.3: Idealized Vortex Shedding Illustration**

This is due to the fact that the vortex shedding frequency ( $n_s$ , rad/s) is directly proportional to the mean wind speed ( $\bar{U}$ ) and inversely proportional to the width of the bluff-body (diameter of the mast-arm) ( $b$ ). The vortex shedding frequency can be expressed as a non-dimensional parameter, the Strouhal number ( $St$ ) which is typically equal to 0.2 for circular shapes [8]. This expression is shown in Equation 1.1.

$$St = \frac{n_s b}{\bar{U}} \quad (1.1)$$

If the frequency at which the vortices are shed roughly corresponds to the natural frequency of the structure, a resonant condition is reached and vibrations with high amplitudes can occur. In some cases, the vibrations of the body itself may enhance the strength of the vortices and may also alter the vortex shedding frequency tending to couple it with the natural frequency of the structure and creating a phenomenon known as ‘lock-in’ [8].

## 1.4 Previous Research

Previous studies have shown evidence of vortex shedding as the mechanism responsible for large-amplitude vibrations of mast-arm traffic signal structures. Of particular note are two studies conducted at Texas Tech University (TTU) [9, 10].

The first of these studies performed full scale experiments utilizing two out-of-service cantilever mast-arm traffic signal structures which were tested at Reese Technology Center Facilities of the Wind Sciences and Engineering Research Center of TTU [9]. These structures had mast-arms with lengths equal to 18.3 m and 13.4 m. Each of the structures had signals with back plates mounted horizontally along the mast-arm. Wind data was recorded by a sonic anemometer mounted above each mast arm while vibrations at the tip of each mast-arm were recorded by video cameras which tracked the motion of an infrared target.

Through this TTU experiment, it was observed that large amplitude vertical vibrations of the mast-arms occurred, for the most part, at particular low wind speed ranges (between 5 and 10 mph), and that as the wind speed increased above that range, the amplitude of the vertical vibrations decreased. Having these large vibrations over a specific wind speed range reflects the typical behavior of vibrations induced by vortex shedding. In the TTU study, it was also observed that higher amplitude vertical oscillations have a higher probability of occurring when the wind speed is steady (i.e. has low turbulence).

As a follow up to this TTU study, a second study, conducted at the same TTU facilities, investigated the wind-induced vibrations of mast-arm traffic signal structures with a variety of mast-arm cross sections and signal cluster configurations [10]. Three configurations were used which are listed as follows: mast-arm with a circular cross section with signals mounted horizontally, mast-arm with a circular cross section with signals mounted vertically, and mast-arm with a 16-sided cross-section with signals mounted vertically. The full scale data collected from this TTU study suggested that for all three systems, the large-amplitude vibrations were induced by ‘lock-in’ vortex-shedding.

## 1.5 Research Objective

In New York State, previously designed and installed mast-arm traffic signal structures longer than 14 m no longer meet the fatigue provisions of the updated AASHTO code [1]. There is concern that these relatively new structures will not provide long-term reliable and safe service. For this reason, the New York State Department of Transportation (NYSDOT) commissioned Research Project No. C-10-07, “Determining Remaining Fatigue Life of In-Situ Mast-Arm Traffic Signal Supports”. This project is a collaborative effort between Rensselaer and NYSDOT and has three primary goals:

- Conduct a thorough investigation (through a full-scale experiment) of the response of a given, in-situ mast-arm traffic signal structure to actual, observed wind conditions
- Indicate a projected ‘safe life’ of this given structure
- Develop a general methodology that can be used to assess the remaining fatigue life of cantilevered mast-arm traffic signal structures throughout New York State

## 1.6 Report Outline

This final report documents the results obtained in relation to these larger NYSDOT project goals.

Chapter 2 introduces an overview of the experimental setup and includes information about the structure under study. Chapter 3 provides the dynamic characteristics of the structure which were estimated by a finite element model and confirmed by free vibration tests. Chapter 4 summarizes the wind vs. mast-arm response data obtained from the full-scale experiment, discusses the experimental

data and turbulence intensity and its effect on vortex shedding. Chapter 5 presents a probability analysis of the wind data obtained through this experiment as well as a comparison with historical data from a nearby National Weather Service station. Chapter 6 presents three methods for estimating natural frequency of structures. Chapter 7 presents the Miner's rule for estimating fatigue life of the structure.

## CHAPTER 2

### EXPERIMENTAL SETUP

#### 2.1 Experiment Introduction

In order to study of the effects of wind induced vibrations on mast-arm traffic signal structures, a full scale experiment was performed on an in-situ cantilevered traffic signal structure located in Malta, NY. To perform this experiment, sensors were installed on the structure in order to monitor wind speed and wind direction along with the corresponding vibrations of the mast-arm. The data obtained from these sensors was recorded through an on-site data acquisition system and collected during weekly site visits for analysis.

##### 2.1.1 Site Information

The traffic signal structure used for the full scale experiments is shown in Figure 2.1. The structure is located at the intersection of Eastline Road and State Route 67 in Malta, NY in a suburban environment typical of Upstate New York.



**Figure 2.1: Instrumented Traffic Signal Structure in Malta, NY**



The mast-arm of this traffic signal structure spans across the shorter of the two diagonals of the skewed intersection with the vertical post located at the north-east corner of the intersection and the free end of the mast-arm extending to the southwest corner as shown in Figure 2.2.



Figure 2.2: Project Location Map [11]

### 2.1.2 Structure Geometry

The traffic signal structure studied has a cantilevered mast-arm spanning 25 m in length making it one of the longest in New York State. The mast-arm of this structure has a tapered diameter ranging from 432 mm at its fixed end to 288 mm at its free end. The vertical post for this structure is 5.8 m tall and has a tapered diameter ranging from 457 mm at the base to 421 mm at the top. Full geometry details for the traffic signal structure are outlined in a set of construction plans provided by NYSDOT (Appendix A).

## 2.2 Instrumentation

### 2.2.1 Overview

Sensors, including one 3-component anemometer and two 3-component accelerometers, were installed on the traffic signal structure to measure wind speed, wind direction, and vibrations of the mast-arm. These sensors were connected to a data logger which was stored in a weatherproof lock-box mounted to the structure. The data logger, in combination with a field laptop, was used to collect and store data from these sensors as individual 15-minute long time history files. An overall layout of the instrumentation is shown in Figure 2.3.

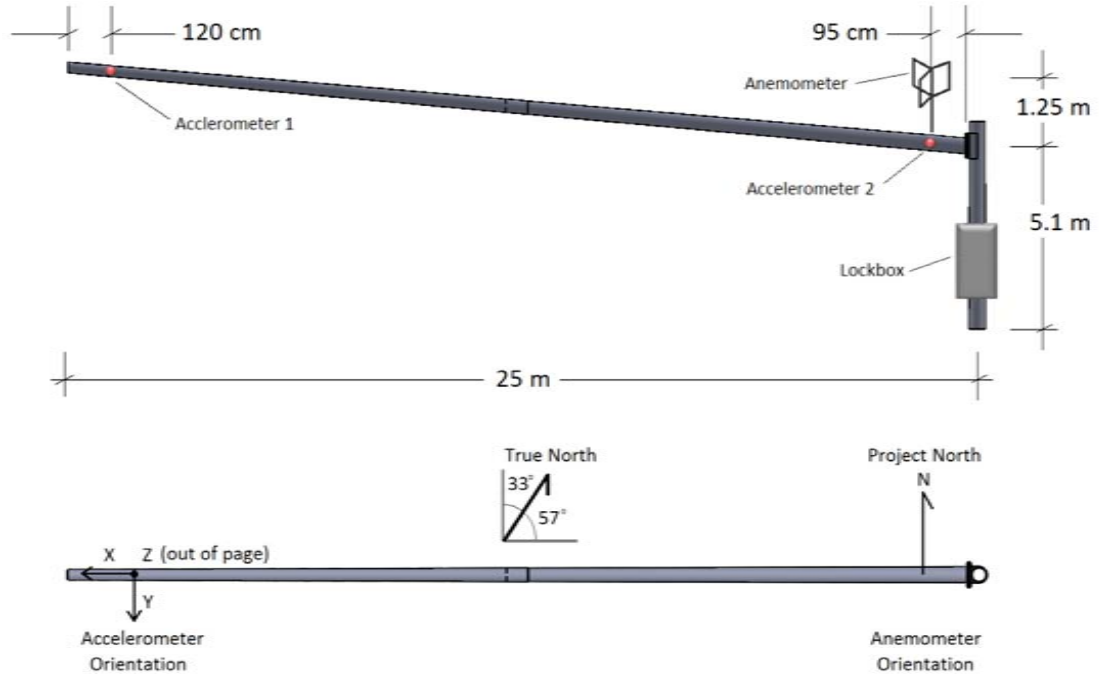
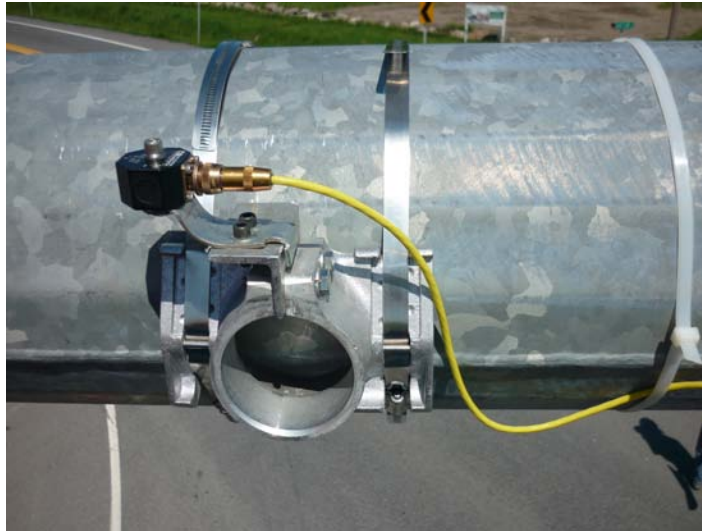


Figure 2.3: Instrumentation Layout and Sensor Orientations

### 2.2.2 Accelerometers

Two Wilcoxon Research Model 993A tri-axial accelerometers (Meggit Sensing Systems) were used to measure the vibrations of the traffic signal structure. Both accelerometers were placed on the mast-arm with one accelerometer (accelerometer

1) located 120 cm from the free end of the mast-arm and the second (accelerometer 2) located near the vertical pole (95 cm from the face of the end-plate). The Wilcoxon accelerometers have a range of  $\pm 50$  g, a sensitivity of  $1.5 \times 10^{-4}$  g, and are able to record data at frequencies up to 2,000 Hz. The accelerometers were oriented such that the x-axis corresponded with the horizontal motion along the length of the mast-arm, the y-axis corresponded to the horizontal motion perpendicular to the length of the mast-arm, and the z-axis corresponded to the vertical motion as shown in Figure 2.3. The accelerometers were bolted to a mounting bracket provided by NYSDOT which was in turn secured to the structure using a set of hose clamps as shown in Figure 2.4. During installation, the accelerometers were aligned and leveled in all three directions using a bubble level and an aligning stick. Multi-conductor, shielded J9T4 cables were used to connect the accelerometers to P703BT tri-axial power units and to the data logger. Power was supplied to these units by LA704B line adapter power supplies. The shielded cables, power units, and power supplies were all supplied by Meggit Sensing Systems.



**Figure 2.4: Installed Accelerometer with Mounting Bracket**

Shortly after its installation, the accelerometer located near the fixed end of

the mast-arm (accelerometer 2) malfunctioned. The purpose of this sensor was to confirm that the structure vibrates in its fundamental mode. Instead, this was confirmed visually and through spectral analysis of the response.

### 2.2.3 Anemometer

To capture wind data, a Model 81000 3-component Ultrasonic Anemometer (R.M. Young Company) was used. This anemometer is able to detect instantaneous wind velocity changes up to 40 m/s, has a sensitivity of 0.01 m/s, and is able to record data at frequencies up to 32 Hz. The anemometer continuously records wind velocities in three directions ( $u, v, w$ ) and uses these to calculate wind speed, elevation angle (wind direction with respect to the horizontal plane), and azimuth angle (wind direction in horizontal plane with respect to project North). The anemometer was attached to a 40 mm diameter galvanized aluminum pipe which was in turn attached to the mast-arm close to the vertical pole using the same mounting bracket which holds accelerometer 2 as shown in Figure 2.5.



**Figure 2.5: Mounting Bracket 2**

The anemometer sat 125 cm above the centerline of the mast-arm in order to minimize turbulence caused by the mast-arm and surrounding electrical wires. This

positioned the anemometer 6.36 m from the ground. A photograph of the installed anemometer is shown in Figure 2.6. It should be noted that the utility pole seen in this photograph (located 3.0 m from the vertical post of the traffic signal structure with a diameter of 35 cm) was not anticipated to cause significant interference in acquiring wind data since it is not located in a prevailing wind direction with respect to the anemometer.



**Figure 2.6: Installed Anemometer**

The anemometer was oriented so that the north direction was aligned perpendicular to the orientation of the mast-arm creating a Project-North which was offset from True North by  $33^\circ$  as shown in Figure 2.3. An 8-conductor shielded cable (Model 18660, R.M. Young Company) was used to connect the anemometer to the data logger.



#### 2.2.4 Lock-Box and Power Supply

A weatherproof lock-box, mounted on the post of the traffic signal structure, was supplied by NYSDOT and used to house the data acquisition system and power supplies. A standard 110 Volt AC power outlet was available inside of the weatherproof lock-box. To supply power to the various devices, a TRC Electronics RS-15-24 power supply was used. This power supply converted the 110 Volt AC power from the outlet to the 24 Volt DC power required for the anemometer, the power channel units for the accelerometers, and the data logger. Figure 2.7 shows the setup inside the lock-box.

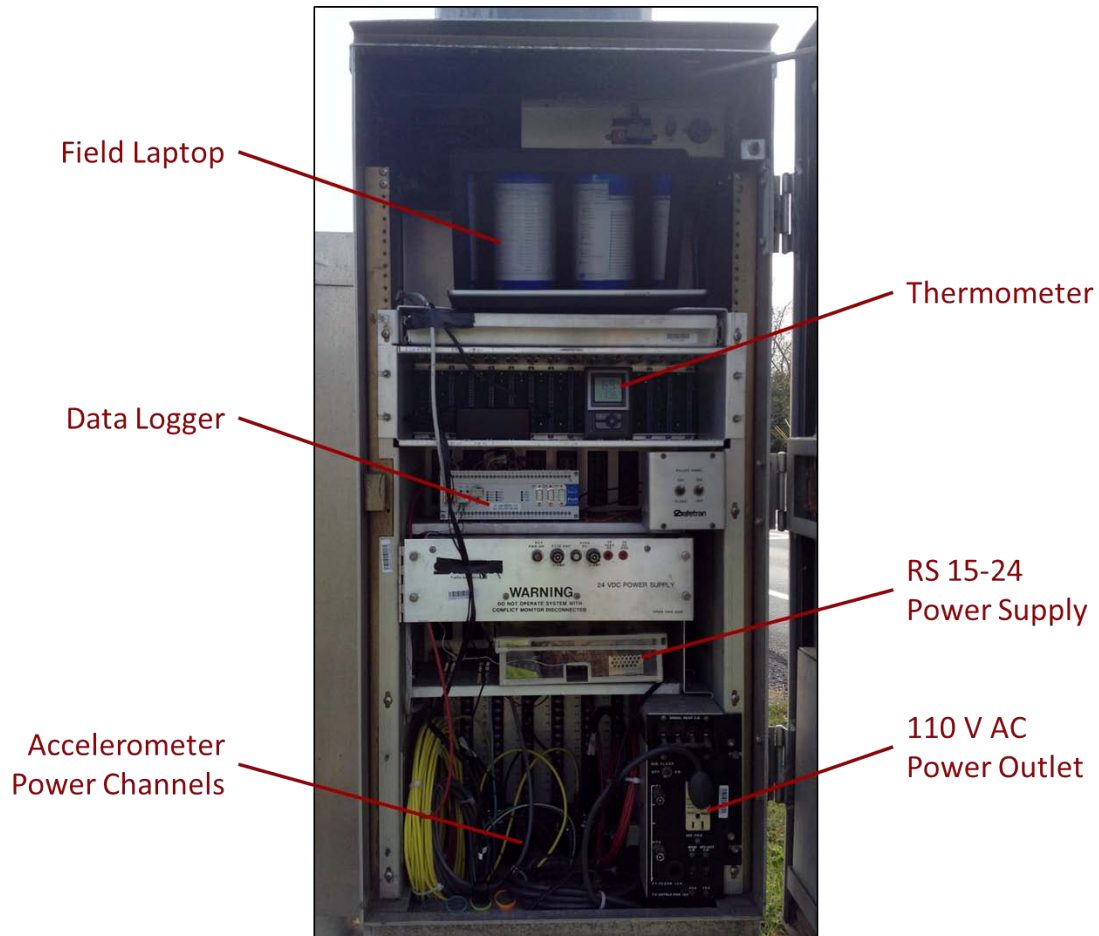


Figure 2.7: Lock Box Setup

### **2.2.5 Data Logger**

The CAS (Computer Aided Solutions) ProfiMessage Data Logger with the ADVT module was chosen as part of the data acquisition system for this project. The ADVT module is an add on that allows the data logger to have 15 analog ports. Using the data logger, 9 channels of data, along with a corresponding date and time stamp, were collected at a rate of 23 Hz. These channels of data included accelerations in the x,y, and z directions from each of the two accelerometers along with wind speed, elevation angle, and azimuth angle from the anemometer. Prior to the development of the system it was estimated that a sampling rate between 20 Hz and 25 Hz would be adequate to fully capture the motion of the mast-arm. The data logger has discrete values for possible sampling rates with 23 Hz being the only rate within the appropriate range.

### **2.2.6 Field Computer**

The Dell semi-rugged Latitude E6430 ATG Laptop was used as the field computer. This computer was chosen for its ability to safely operate within an extreme range of temperatures (0 to 32 °C or 32 to 95 °F), an important consideration for the Upstate New York climate. An indoor/outdoor thermometer was used to record the high and low temperatures reached both inside and outside of the lock-box between each site visit to ensure safe operating conditions were kept for the field computer. The computer communicated with the data logger via an Ethernet cable.

### **2.2.7 Software**

Both components of the data acquisition system (the data logger and the field computer) used ProfiSignal software developed by Delphin Technology. The software on the data logger was set to continuously record voltages collected by the three sensors and convert these voltages to useful data in engineering units. The

software on the computer was programmed to then save 15-minute increments of this continuously recorded data into individual time history files which were saved using the following naming convention:

*RawDataY###-M#-D#\_h#-m#-s#.hds*

Where:

- Y# = four digit year
- M# = two digit month
- D# = two digit day
- h# = two digit hour (in 24-hour clock format, local time)
- m# = two digit minute
- s# = two digit second

The parameters listed represent the date and time at the beginning of the 15-minute data increment.

## 2.3 Installation

The equipment installation took place on Thursday, May 17th, 2012 between the hours of 10:00 AM and 3:00 PM. Donnelly Construction Inc. (Mechanicville, NY) provided the traffic control during the equipment installation. A project specific Work Zone Traffic Control Plan (WZTCP) consistent with NYSDOT Standard Sheet 619-61 was developed and approved by NYSDOT prior to the installation date. During the installation, the two mounting brackets were secured onto the mast-arm. Shielded electrical wiring was strung from each of the sensors to the data logger located inside the lock-box. This wiring was secured to the mast-arm



and the vertical post by 150 cm nylon cable ties. To access the mast-arm, a boom lift, operated by a member of the research team, was used. Figure 2.8 shows a photograph taken during the installation. Because of the restricted time in which lane closures were allowed, the data logger and power supplies were installed and set up in the lock-box concurrent with the installation of the sensors on the mast-arm. After these two tasks were completed, the wiring from the sensors was connected to the data logger and the final programming of the data logger took place.



**Figure 2.8: Installation Photograph**

After installation was complete, free vibration (excitation) tests were performed. Further details concerning these tests are provided in Chapter 3.

## CHAPTER 3

### DYNAMIC CHARACTERISTICS

#### 3.1 Introduction

Prior to choosing the instrumentation plan for the full scale experiments, a finite element computer model (FEM) was created in order to estimate the natural frequencies and mode shapes for the first and higher modes of the traffic signal structure studied. This model was created using ABAQUS/CAE, a commercially available software package used for finite element analysis. The natural frequency results from the finite element model were compared with the experimentally measured natural frequencies obtained through free vibration tests or 'pluck tests'.

#### 3.2 Finite Element Model

##### 3.2.1 FEM Geometry

Dimensions of the traffic signal structure for use in the finite element model were taken from construction plans provided by NYSDOT which are included in Appendix A. Measurements of the structure were also taken during the installation of the sensors and indicate that the structure was constructed in accordance with the contract drawings. The finite element model of the structure consisted of six individually created parts joined together using tied (no slip and no rotation) conditions applied to the surfaces between connecting parts of the structure to create one assembly. These six parts include two parts for the mast-arm (one for each side of the existing slip joint connection), the vertical post, and three parts for the connection detail between the mast-arm and the vertical post. These parts are shown in an 'exploded' view in Figure 3.1. Details such as the taper of the mast-arm, the

taper of the vertical post, the mast-arm connection details, and the mast-arm slip joint detail were included in the model.

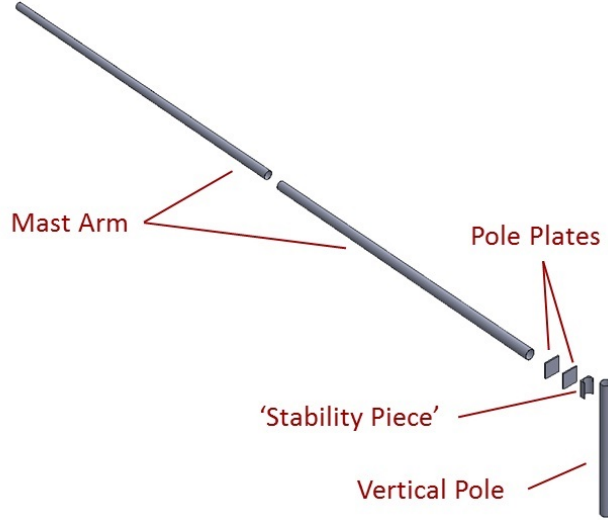


**Figure 3.1: FEM Components**

### 3.2.2 Material Properties

Typical material properties for ASTM A572 Gr 65 steel, as specified on the plans provided, were used and applied as solid homogeneous sections throughout the model. These properties are summarized in Table 3.1.

**Table 3.1: Material Properties**

Material Property	Value (English Unit)	Value (SI unit)
Mass Density	490 lbs/ft <sup>3</sup>	7850 kg/m <sup>3</sup>
Young's Modulus	29000 ksi	200 GPa
Poisson's Ratio	0.25	0.25

### 3.2.3 Mesh Properties

General purpose three-dimensional linear hexahedral elements were used for the model's mesh. Specifically, type C3D8R elements were used each consisting of 8 nodes, 6 faces, and a single integration point located in the center of the element as shown in Figure 3.2.

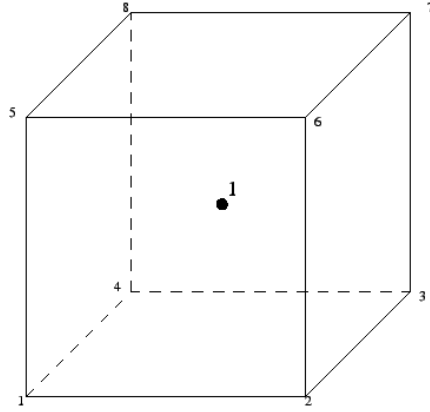


**Figure 3.2: C3D8R Element**

A moderate number of 3156 nodes and 1649 elements were used in the model to provide a balance between accuracy and computational cost. The elements used for the mast-arm were sized such that the arm was sectioned into 50 segments along its length (each with a length equal to 20 in ( or 0.5 meters)) and 8 segments around its circumference. The connection detail between the mast-arm and the vertical post was meshed with a higher nodal density to ensure an accurate calculation of stresses and strains, as this region will experience the highest magnitude of stresses. The resulting mesh is shown in Figure 3.3.

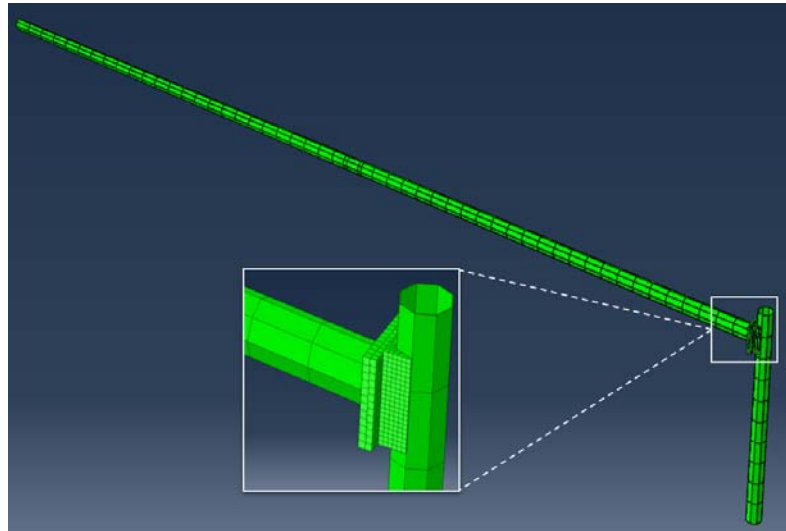


**Figure 3.3: FEM Mesh**

### 3.2.4 Traffic Signals

Traffic signals were assumed to act as point masses and were added to the finite element model as such. The locations of the traffic signals along the length of the mast-arm were estimated from a combination of photographs and field measurements since these dimensions were not given on the NYSDOT plans provided. The masses of the traffic signals were estimated to be 27 kg for the single sets of signals [12] and 54 kg for the multi-sets and were applied along the centerline of the mast-arm. The estimated locations and masses of the traffic signals used for the finite element model are summarized in Table 3.2.

**Table 3.2: Applied Traffic Signals**

Estimated Location (measured from free end of mast-arm) [ft]	Point Mass Applied [lbs]
26.2	59.5
39.4	119.0
44.3	59.5
55.8	119.0
59.0	59.5
67.3	119.0
73.8	59.5

### 3.2.5 Boundary Conditions

The NYSDOT plans indicated that the traffic signal structure is attached to the foundation by four bolts which provide flexibility in each of the three Cartesian directions by a combination of their tensile, flexural, and shear behavior. This flexibility was modeled through the application of springs to the base of the FEM structure. These springs had independent stiffness values which were specified for the x, y, and z directions. Figure 3.4, shows a bolt detail for the structure, which consists of a portion of the bolt embedded in concrete ( $L_2$ ), and a portion of the bolt above the surface of the concrete pad ( $L_1$ ).

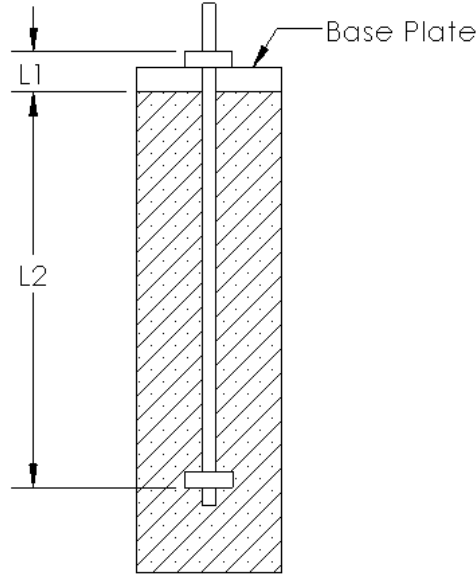


**Figure 3.4: Structural Bolt Detail**

#### **3.2.5.1 Longitudinal Bolt Stiffness**

The longitudinal stiffness of the bolts (stiffness in the vertical direction) is due to tensile behavior and can be expressed by Equation 3.1 where  $E$  is Young's modulus,  $A$  is the cross-sectional area of the bolt, and  $L_e$  is the effective length.

$$k = \frac{P}{\Delta} = \frac{EA}{L_e} \quad (3.1)$$

To estimate the effective length of the anchor bolt, a constant-friction condition was assumed for the portion of the bolt embedded in concrete in which the axial force in the anchor bolt is zero at the end and the full maximum value at the top. (Figure 3.5).

Integrating the linearly varying strain along the length of the anchor bolt gives the displacement at the top of the bolt. From this integration, it can be shown that the resulting displacement is equivalent to that of an anchor bolt with a constant maximum force ( $P$ ) applied over half the anchor bolt. The displacement expression can then be written as the displacement resulting from a constant maximum force

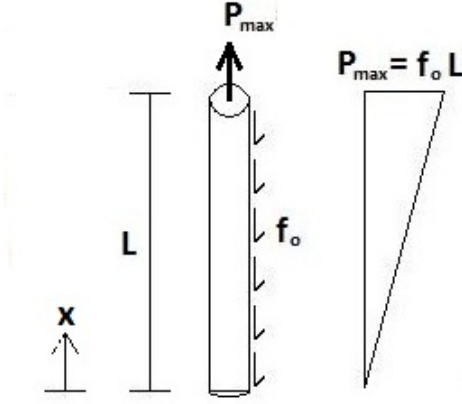


**Figure 3.5: Constant Frictional Force Along Bolt with Corresponding Linearly Varying Force Profile**

( $\frac{P_{max}L}{AE}$ ) but with an effective length,  $L_e$ , equal to  $L_2/2$ . The integration is shown in equations 3.2 to 3.7 below.

$$\Delta = \int_0^{L_2} \epsilon(x) dx. \quad (3.2)$$

$$\Delta = \int_0^{L_2} \frac{P(x)}{AE} dx. \quad (3.3)$$

$$\Delta = \int_0^{L_2} \frac{f_o x}{AE} dx. \quad (3.4)$$

$$\Delta = \frac{f_o L_2^2}{2AE} \quad (3.5)$$

$$\Delta = \frac{P_{max}(L_2/2)}{AE} \quad (3.6)$$

$$\Delta = \frac{P_{max}(L_e)}{AE}, \text{ where } L_e = \frac{L_2}{2} \quad (3.7)$$

Since the effective length resulting from this derivation (Equation 3.7) corresponded only to the portion of the bolt embedded in the concrete,  $L_1$  was also added resulting in the final effective length expression shown in Equation 3.8.

$$L_e = L_1 + \frac{L_2}{2} \quad (3.8)$$

To calculate the longitudinal bolt stiffness, Equation 3.8 was substituted into the stiffness formula shown in Equation 3.1. The parameters used for the calculation along with the resulting longitudinal bolt stiffnesses used in the FEM are listed below in Table 3.3.

**Table 3.3: Longitudinal Bolt Stiffness Parameters**

Property	Value
Young's Modulus, E	29000 ksi
Cross Sectional Area, A	3.95 in <sup>2</sup>
$L_1$	4.7 in
$L_2$	36 in
Effective Length, $L_e$	41 in
Stiffness, $k_z$	3.36 x 10 <sup>7</sup> lb/ft

### 3.2.5.2 Transverse Bolt Stiffness

The transverse stiffnesses of the base fixity (stiffnesses in both of the lateral directions) is due to a combination of flexural and shear behavior of the bolts and can be expressed by Equation 3.13. In this equation E is Young's modulus, G is the Shear Modulus, A is the cross-sectional area of the bolt, and  $L_e$  is the effective length. This expression can be derived from the equilibrium equation shown in Equation 3.9, the constitutive relations shown in Equations 3.10 [13] and 3.11 [14], and the stiffness equation shown in Equation 3.12.

$$\Delta = \Delta_{flex} + \Delta_{shear} \quad (3.9)$$



$$\Delta_{flex} = \frac{FL_e^3}{12EI} \quad (3.10)$$

$$\Delta_{shear} = \frac{FL_e}{AG} \quad (3.11)$$

$$k = \frac{F}{\Delta} \quad (3.12)$$

$$k = \frac{1}{\frac{L_e^3}{12EI} + \frac{L_e}{AG}} \quad (3.13)$$

Figure 3.6 shows the bolt detail for this structure, along with a stress profile for the portion of the bolt embedded in the concrete that resists a horizontal load. For the purposes of this investigation, it was estimated that  $L_2$  was approximately equal to twice  $L_1$ . The resulting effective length is listed in Table 3.4 below along with a summary of the parameters used in the calculation of the lateral stiffness of the bolts. The resulting stiffness, also listed in Table 3.4, was applied to each of the four bolts in both the x and y-directions.

**Table 3.4: Lateral Bolt Stiffness Parameters**

Property	Value
Young's Modulus, E	29000 ksi
Shear Modulus, G	11500 ksi
Cross Sectional Area, A	3.95 in <sup>2</sup>
$L_1$	4.7 in
$L_2$	9.4 in
Effective Length, $L_e$	14.1 in
Stiffness, $k_x$ , $k_y$	1.7 x 10 <sup>6</sup> lb/ft

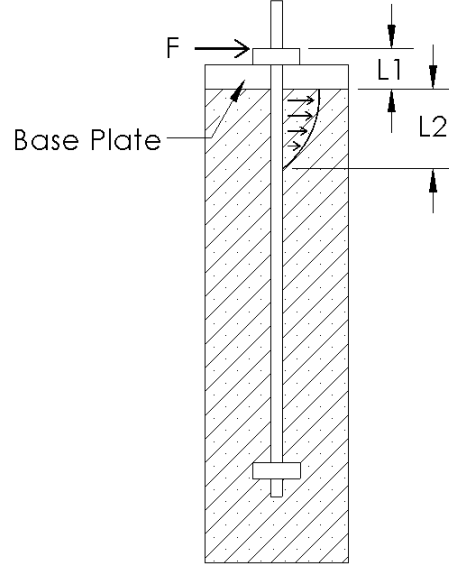


**Figure 3.6: Bolt Detail with Stress Profile for Lateral Displacement**

### 3.3 FEM Results

#### 3.3.1 Natural Frequencies

Once created, the finite element model was analyzed with an Eigensolver built into ABAQUS to determine the natural frequencies and mode shapes of the structure. Through this analysis, it was calculated that the traffic signal structure would have a fundamental natural frequency of 0.51 Hz for vibration in both the vertical direction and the horizontal direction. These fundamental frequencies, along with natural frequencies corresponding to higher modes of vibration, are summarized in Table 3.5.

**Table 3.5: FEM Natural Frequencies**

Mode	Vibration Direction	Natural Frequency, $f_n$ [Hz]
1 <sup>st</sup>	Vertical	0.51
1 <sup>st</sup>	Horizontal	0.51
2 <sup>nd</sup>	Vertical	2.1
2 <sup>nd</sup>	Horizontal	2.3
3 <sup>rd</sup>	Vertical	3.6
3 <sup>rd</sup>	Horizontal	4.1

In order to validate the results from the FEM during the initial stages of the project (before field tests), hand calculations were performed to estimate the natural frequency of the mast-arm of the structure. The results from these hand calculations were compared to a FEM of the mast-arm alone. The method used for these hand calculations, along with a comparison with the FEM result for the mast-arm's natural frequency, is detailed in Appendix B.

### 3.3.2 Mode Shapes

Following the natural frequency calculations, corresponding mode shapes were plotted for visualization purposes. The fundamental mode shapes for vibrations in both the vertical and horizontal directions are shown in Figures 3.7 and 3.8.

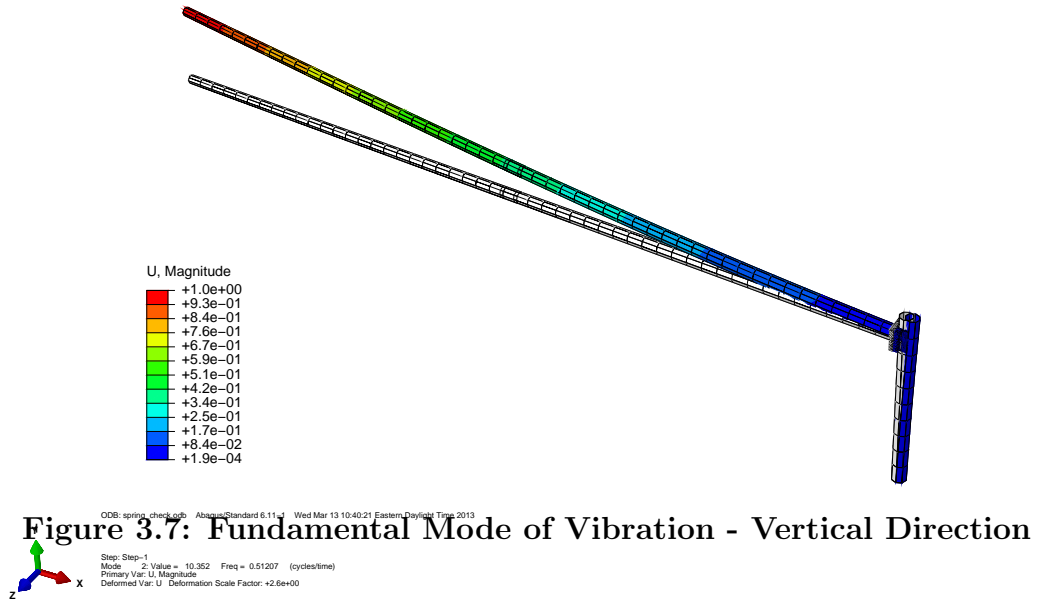


**Figure 3.7: Fundamental Mode of Vibration - Vertical Direction**

Additionally, higher mode shapes were produced through the finite element analysis. Several of these higher mode shapes are included in Appendix C.

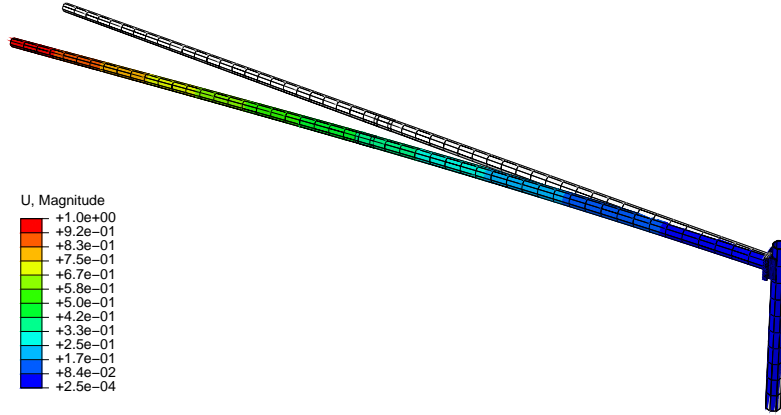


**Figure 3.8: Fundamental Mode of Vibration - Horizontal Direction**

## 3.4 Free Vibration Tests

### 3.4.1 Method

Directly following the installation of the sensors and the data acquisition system, free vibration tests (‘pluck tests’) were performed in order to experimentally determine the natural frequencies and damping ratios of the traffic signal structure in both the horizontal (y) and vertical (z) directions. To conduct these tests, the tip of the mast-arm was accessed via a boom lift and the structure was excited into a resonant response before being released into free vibration. During this free vibration phase, the accelerations at the tip of the mast-arm were recorded through the data acquisition system, immediately viewed on site, and saved for further analysis. A free vibration test was repeated twice for each direction at which point it was determined that the data collected was consistent and that no additional tests were necessary.

### 3.4.2 Natural Frequencies

The data collected from the free vibration tests was used to plot Fourier amplitude spectra in order to determine the fundamental natural frequency of the

structure in the horizontal and vertical directions. In the case of free vibration, the first peak seen on a Fourier amplitude spectrum indicates the natural frequency of the system. The pluck test results indicated that the structure has a natural frequency of 0.49 Hz in the horizontal (y) direction and 0.52 Hz in the vertical (z) direction. The acceleration time history response and corresponding Fourier amplitude spectrum for one free vibration test in the z-direction are shown in Figures 3.9 and 3.10 below. Additional plots are provided for the remaining free vibration tests in Appendix C.

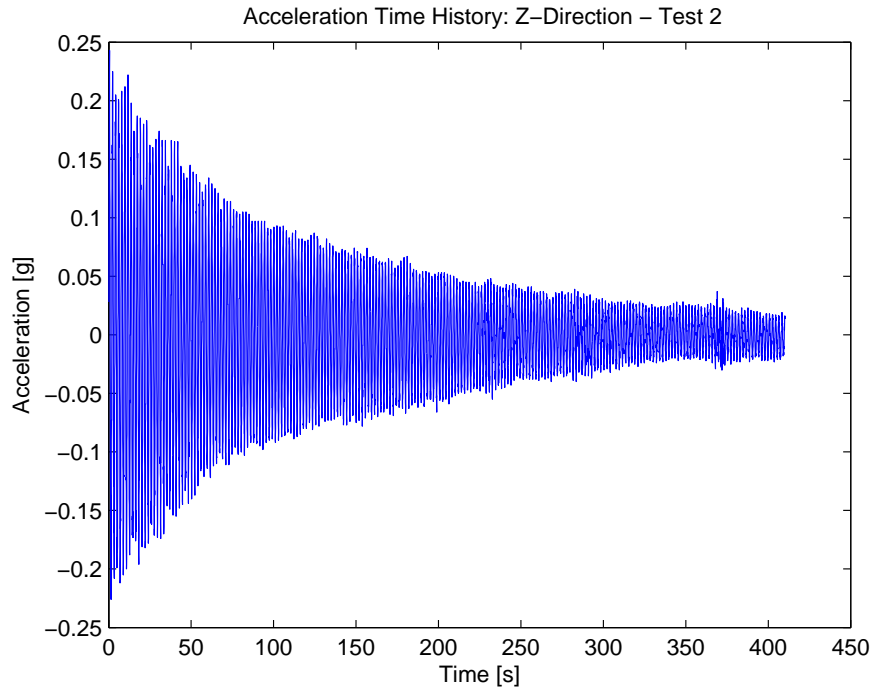


**Figure 3.9: Pluck Test (Z-Direction, Test 2): Acceleration Time History**

### 3.4.3 Damping Ratios

The damping ratios of the structure for vibration in each direction were calculated using the acceleration time history data from the free vibration tests and the logarithmic decrement method shown in Equation 3.14.

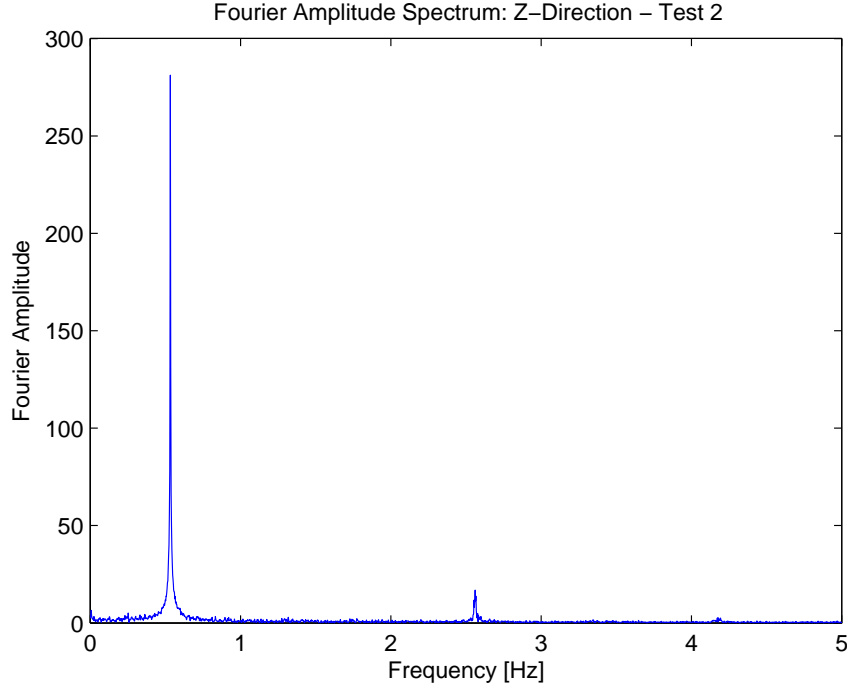


**Figure 3.10: Pluck Test (Z-Direction, Test 2): Fourier Amplitude Spectrum**

$$\xi = \frac{\ln(\ddot{u}_i/\ddot{u}_{i+j})}{2j\pi} \quad (3.14)$$

In this equation,  $\ddot{u}_i$  and  $\ddot{u}_{i+j}$  are the accelerations at two given peaks in the acceleration time history and  $j$  is the number of cycles between the two peaks. To avoid experimental error, numerous peaks were used for the damping ratio calculations. The damping ratio of any given structure is dependent on the structure's amplitude of vibration. This is because at different vibration amplitudes, different mechanisms for dissipating energy are engaged. For this structure, high amplitude vibrations were defined as those having a magnitude above 0.10 g for the z-direction and 0.05 g for the y-direction.

Table 3.6 summarizes the damping ratios obtained from the free vibration tests. Figure 3.11 shows the decay envelope obtained from the calculated damping

ratios for the z-direction overlaid on the acceleration time history response for a free vibration test in the z-direction. In addition, Figure 3.12 shows simultaneous vibrations in the y and z-directions during a pluck test in the z-direction. The small amplitude of the vibrations in the y-direction can mostly be attributed to noise from the accelerometer indicating that there was no energy transfer to other vibrational modes during the pluck test and that the decay of the vibrations in the z-direction was solely due to damping.

Determining accurate damping ratios is relatively difficult to do with experimental data, resulting in data that varied from test to test. However, the important conclusion was reached that this structure has very little damping. During the free vibrations tests, the structure oscillated for upwards of 10 minutes before the vibrations were dissipated.

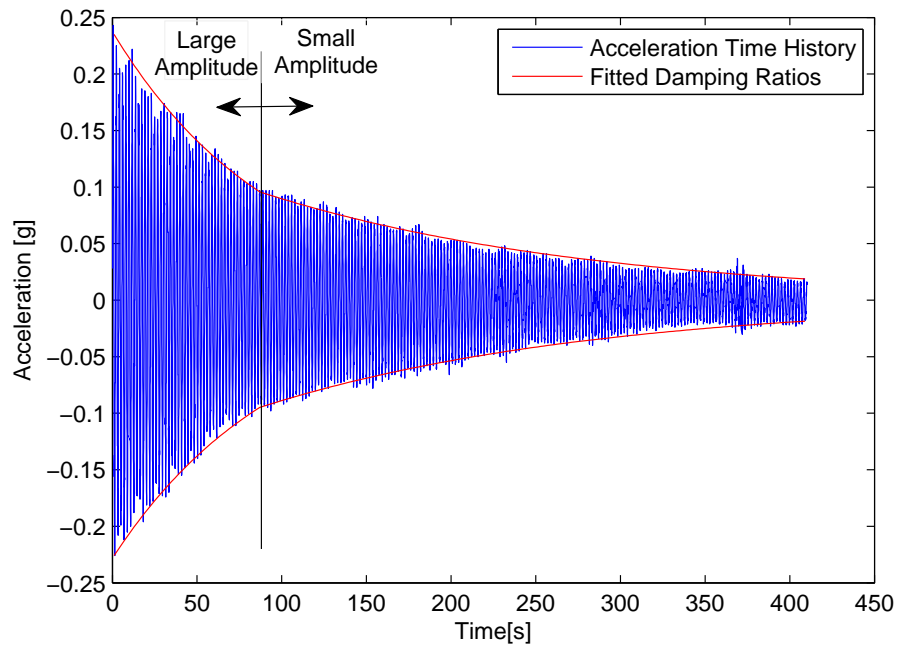


**Figure 3.11: Pluck Test (Z-direction, Test 2): Overlaid Decay Envelope**

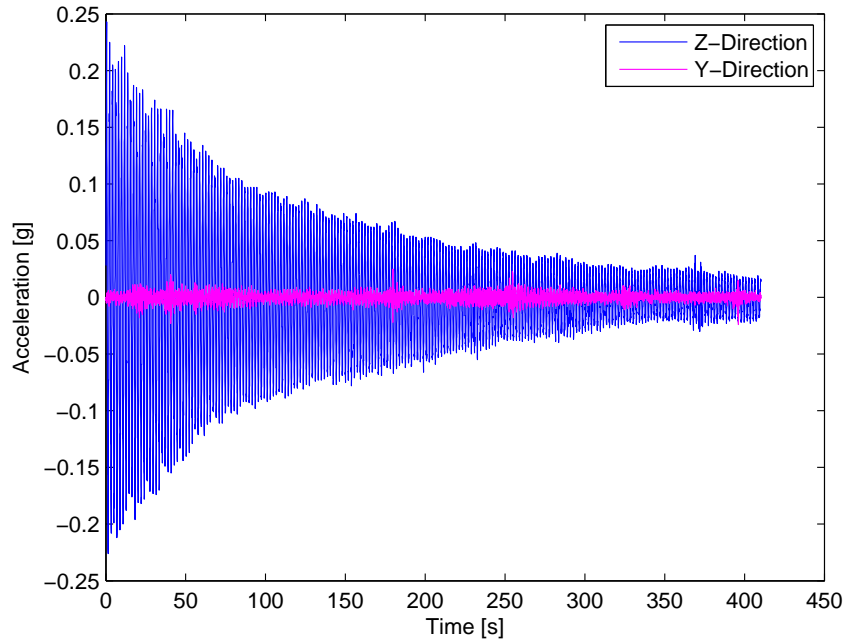


Figure 3.12: Pluck Test (Z-direction, Test 2): Y and Z Accelerations

Table 3.6: Damping Ratios

Test	High Amplitude	Low Amplitude
Z1	0.22%	0.18%
Z2	0.33%	0.16%
<b>Z Average</b>	<b>0.28%</b>	<b>0.17%</b>
Y1	0.51%	0.54%
Y2	0.72%	0.42%
<b>Y Average</b>	<b>0.62%</b>	<b>0.48%</b>

### 3.5 Comparison of Results

Table 3.7 provides a comparison of the natural frequencies calculated from the finite element model to those determined experimentally from the free vibration tests. As shown in this table, there is reasonable agreement between the two fundamental frequency values for each direction with errors less than 5%. It should be noted, however, that if an assumption of fully fixed boundary conditions is made, rather than considering foundational flexibility due to the anchor bolts, the natural frequencies in both directions are overestimated by the FEM with an especially



unacceptable error (32.0%) for the y-direction.

**Table 3.7: Natural Frequency Comparison**

	Vertical (Z-direction)	Horizontal (Y-direction)
Free Vibration Tests	0.53 Hz	0.50 Hz
FEM: Semi-Rigid BC	0.51 Hz	0.51 Hz
Percent Error	3.8%	2.0%
FEM: Fully Fixed BC	0.55 Hz	0.66 Hz
Percent Error	7.8%	32.0%

### 3.6 Estimated Critical Wind Speed

When vortex shedding is observed as the mechanism responsible for large amplitude vibrations of the mast-arm in the vertical direction, the largest of these vibrations occur due to a resonant condition at which the vortex shedding frequency is equal to the natural frequency of the structure. Results from the free vibration tests were used along with the vortex shedding expression (Equation 3.15) to estimate a critical wind speed at which resonance was most likely to occur. The Strouhal number ( $St$ ) was taken to be 0.2, a typical value for circular shapes [8]. Since the mast-arm of the structure of study is tapered, an average diameter of 14.2 in (or 0.360 m) was used for the width of the bluff-body ( $b$ ).

$$n_s = \frac{St\bar{U}}{b} \quad (3.15)$$

The resulting estimated critical wind speed corresponding to resonance for this particular structure ( $\bar{U}$ ) was 13.2 mph (or 5.9 m/s).

## CHAPTER 4

### WIND AND VIBRATION DATA

#### 4.1 Introduction

A full scale investigation of wind-induced vibrations of mast-arm traffic signal structures was undertaken using a signal structure located in Malta, NY (Figure 4.1). The cantilevered mast-arm of this structure extends 82 feet (25 meters) making it one of the longest in NY state. This chapter presents analysis of the wind and vibration data obtained from this investigation. The data used in this chapter was collected between June 5th, 2012 and August 22nd, 2013. Hence it represents over a full year of vibration data



**Figure 4.1: Instrumented Traffic Signal Structure in Malta, NY**

#### 4.2 Methodology

Wind data was collected through an on-site anemometer which continuously measures wind speed and wind direction at a rate of 23 Hz. The corresponding vibrations of the mast-arm, also collected at sampling rate of 23 Hz, are measured

through an accelerometer (Accelerometer 1, Figure 4.2) located near the free end of the mast-arm. Accelerometer 2 (shown in Figure 4.2) malfunctioned, and has not been used for analysis. Additional information regarding the instrumentation setup and the data acquisition process is included in the Chapter 2, however, as a quick reference, Figure 4.2 is included below to show schematics of the layout and orientations of the instrumentation

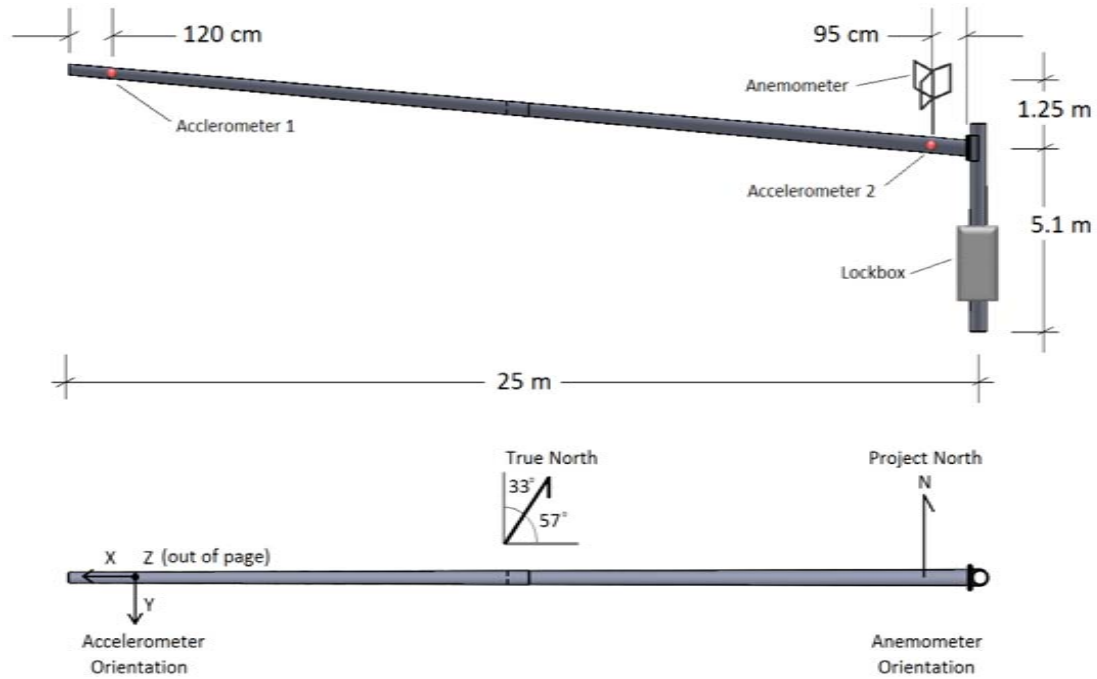


**Figure 4.2: Instrumentation Layout and Sensor Orientations**

Data from the sensors is collected into individual 15-minute time history files which are stored on a laptop located in the lockbox and are downloaded during weekly site visits. For analysis, the raw time history data were divided into 60-second increments for which incremental summary statistics were calculated. These summary statistics included RMS (root mean square) accelerations for the two primary directions of vibration (y and z), average wind speed (arithmetic mean over 60 seconds), average wind elevation angle (arithmetic mean over 60 seconds), average wind direction (circular average over 60 seconds), and turbulence intensity.

Note that the 60 second averaging interval allows for a better direct comparison with the results from similar experiments conducted at Texas Tech University [9, 10].

Turbulence intensity was included as a summary statistic, and is defined as the ratio of the standard deviation of the wind speed to its mean value as expressed in Equation 4.1 below [3].

$$I_u = \frac{\sigma_u}{\bar{U}} \quad (4.1)$$

where  $\sigma_u$  is the standard deviation of the wind speed and  $\bar{U}$  is the mean wind speed over 60 seconds.

Turbulence in the approach flow tends to make the shedding of vortices less coherent and any particular critical wind speed less sustained, with the level of turbulence directly influencing the likelihood of long-lasting, high-amplitude vibrations potentially capable of causing fatigue damage.

Several quality assurance measures have been undertaken in order to ensure that uncontaminated data is used for analysis. These measures include removing data that is below thresholds of interest, performing baseline corrections, and removing erroneous spikes and stalled/zero readings in the time history records. These measures are outlined as follows

#### **4.2.1 Applying Baseline Correction**

The acceleration records showed oscillations about a non-zero horizontal axis which was likely due to the accelerometer not being perfectly level in the field. To correct this problem, baseline corrections were applied to the acceleration records through the use of high-pass filters. High-pass filters attenuate low frequency components of the acceleration signal while preserving any high-frequency components. An example comparison between an uncorrected and corrected acceleration time

history record is shown in Figure 4.3.

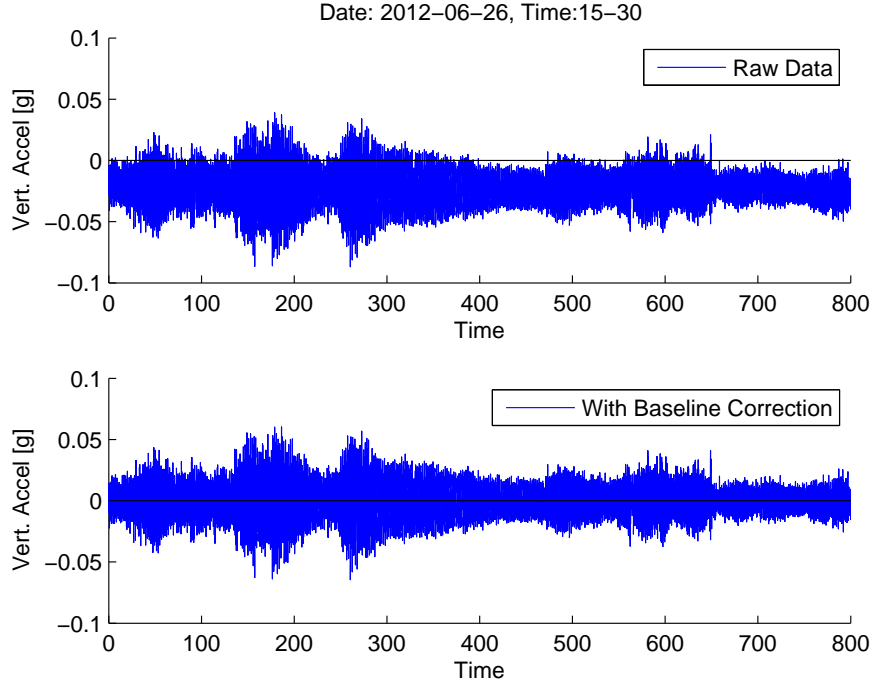


**Figure 4.3: Acceleration Baseline Correction**

#### 4.2.2 Removing Below Threshold Data

With the exception of analysis involving probability distributions (such as the wind data analysis presented in Chapter 5) in which all data was considered, low wind speeds which resulted in negligible accelerations of the mast-arm were below thresholds of interest for this investigation. For this reason, 15-minute data files which did not contain any 30-second increments with an average wind speed greater than 3.0 m/s were removed from the dataset. Considering 30-second incremental wind speeds (instead of 15-minute average wind speeds) ensured that small time periods of noteworthy data were not lost even though longer term (15-minute) average values were relatively small. Approximately 70 percent of the 15-minute data files were removed from the data set in this manner which vastly decreased the required computational time.

### 4.2.3 Removing Erroneous Acceleration Values (Spikes and Zeros)

Due to the nature of the electronics within accelerometers, occasionally large erroneous spikes were seen in the accelerations time history files. To ensure that uncontaminated data was used for analysis, incremental summary statistics for 60-second data segments which contained these spikes were removed from the data set. Acceleration records were searched for such spikes by locating 60-second data segments which contained any accelerations greater than 4 times the RMS acceleration for that segment. As an example, for the time history record shown in Figure 4.4, this method removed the data between 690 and 720 seconds because of the acceleration spike seen just before the 700 second mark.

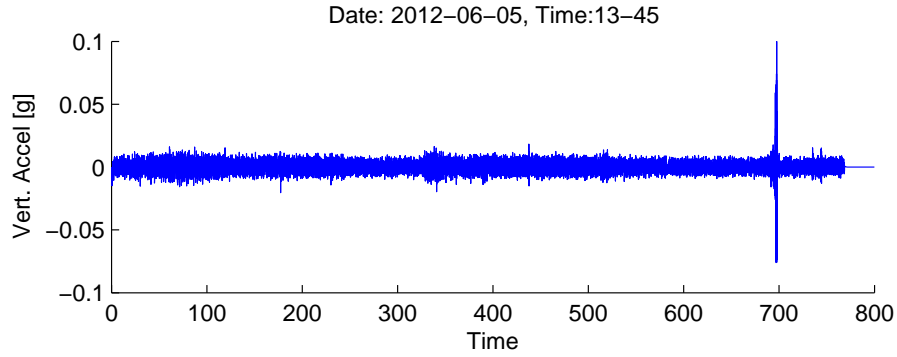


**Figure 4.4: Acceleration Time History Showing Erroneous Readings**

An additional quality assurance step was taken to remove any time segments during which the system ‘froze’ while recording data. An example of this is seen during the last 30-seconds of the time history shown in 4.4. These segments were isolated by identifying erroneous zero measurements for accelerations.

After filtering out these contaminated portions of the acceleration data (including the erroneous spikes and zero values), RMS accelerations (for 60 second time increments) corresponding to vertical vibrations (z-direction, cross-wind response) and horizontal vibrations (y-direction, along-wind response) of the mast-arm were

plotted against 60 second average wind speeds. For comparison, Figures 4.5 and 4.7 show raw data plots for vertical and horizontal vibrations while Figures 4.6 and 4.8 contain the filtered quality assured data. It should also be noted that all four of these graphs include baseline corrections for the acceleration data.

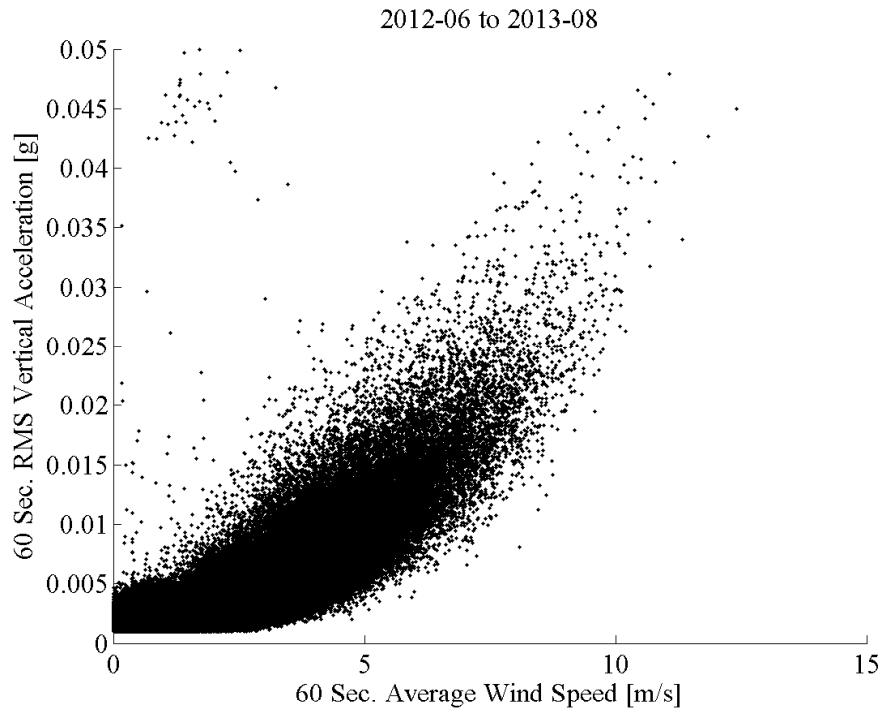


**Figure 4.5: Vertical Response vs. Wind Speed - Raw Data**

### 4.3 Results

Figure 4.9 shows an example of a 15-minute time history file which contains the vertical and horizontal accelerations at the tip of the mast-arm (top and second plots respectively), the wind speed (third plot), and the wind direction or azimuth angle (bottom plot). Between the 600 and 700 second mark in this time history file, critical wind conditions for vortex shedding were reached (wind speed approximately equal to 6 m/s and angle of attack approximately  $360^\circ$  or perpendicular to the mast arm), and correspondingly, a burst of relatively higher vertical accelerations was

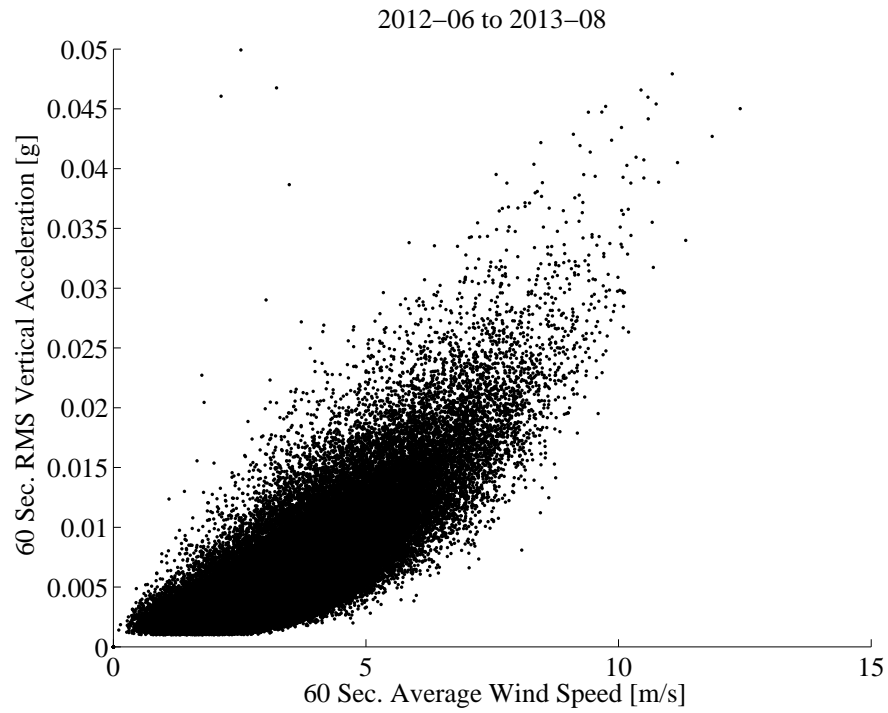


**Figure 4.6: Vertical Response vs. Wind Speed - Filtered Data**

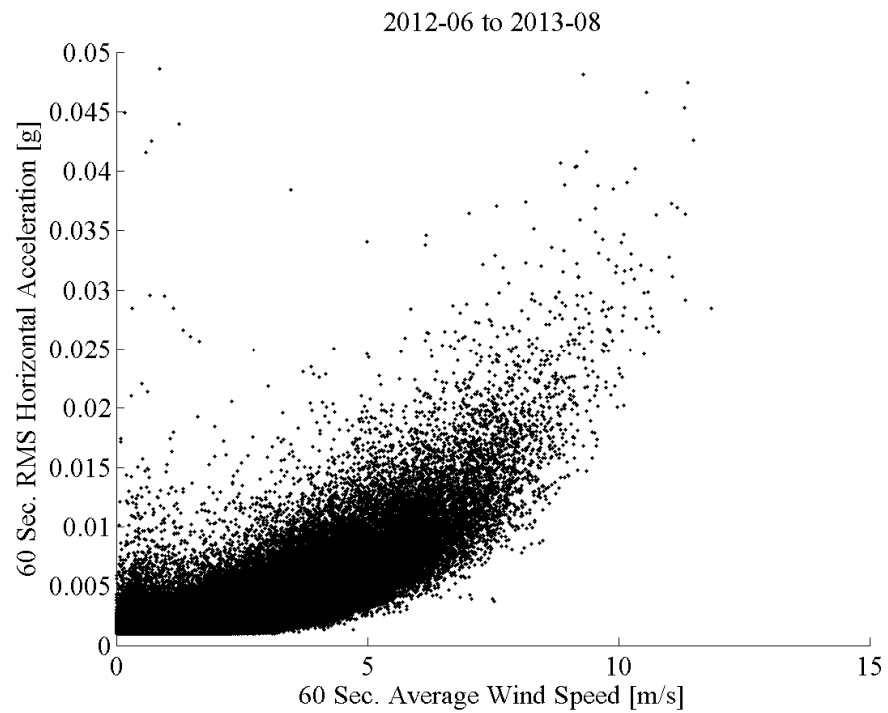


**Figure 4.7: Horizontal Response vs. Wind Speed - Raw Data**



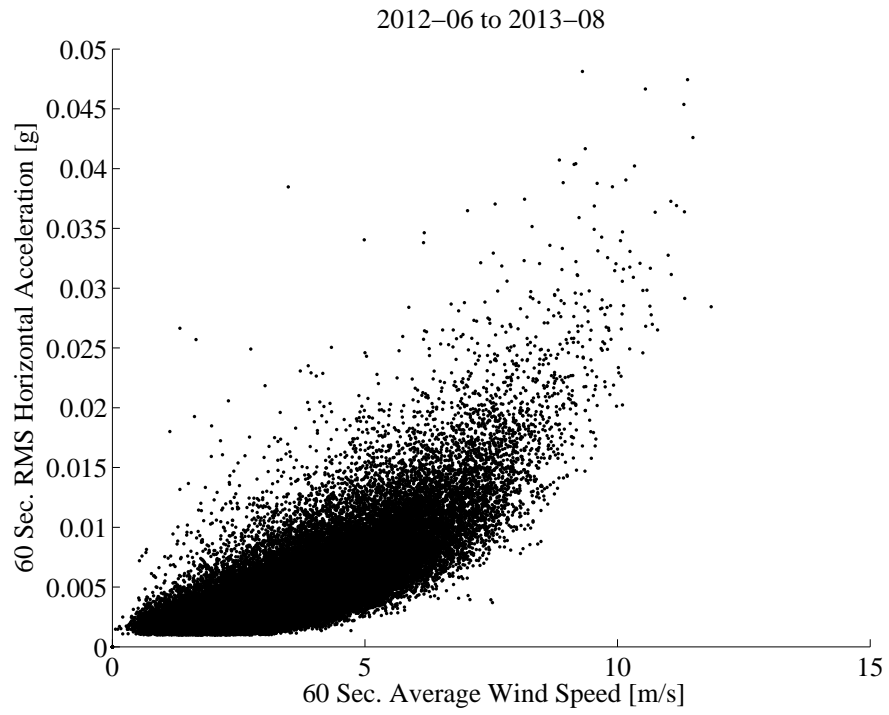


Figure 4.8: Horizontal Response vs. Wind Speed - Filtered Data

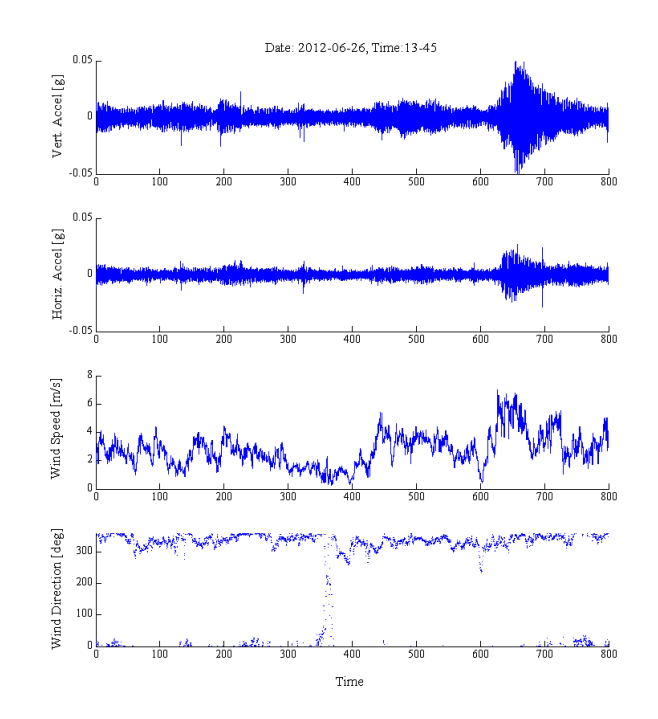
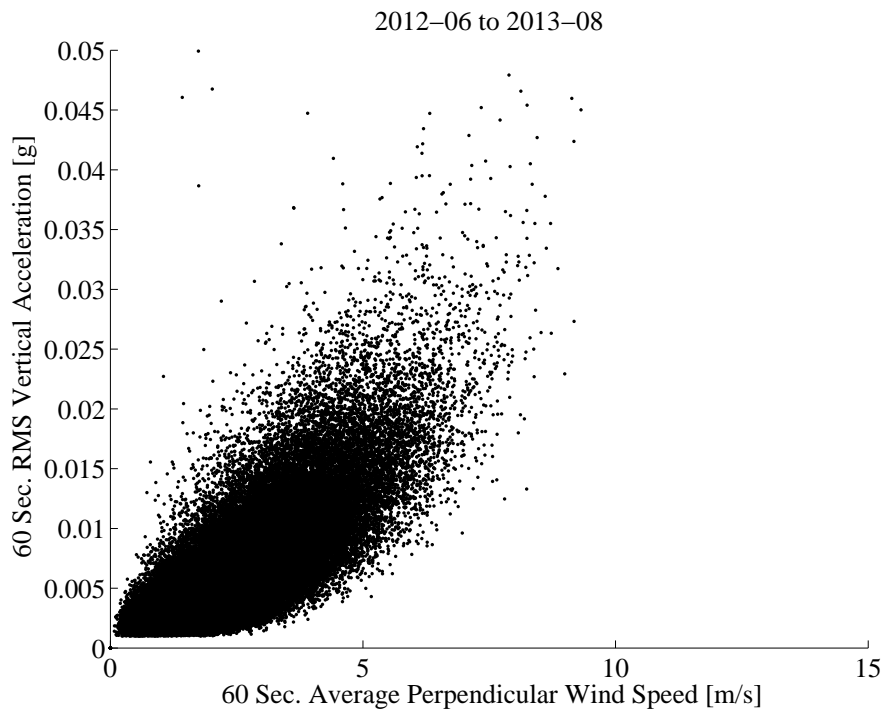


Figure 4.9: Time History Response

observed consistent with a vortex shedding phenomenon. In Figure 4.9, the large vibrations begin near the 630 second mark when the wind speed first approaches the critical wind speed. The response built up for roughly 30 seconds as the wind velocity remained approximately constant but began to ring-down at 660 seconds when the wind speed dropped below the critical velocity

The response of the mast arm is a combined function of parameters including wind speed and wind direction rather than just the scalar wind speed. RMS vertical and horizontal accelerations were plotted against 60-second mean perpendicular wind speeds, i.e. the component of the wind acting perpendicular to the length of the mast-arm as shown in Figures 4.10 and 4.11.



**Figure 4.10: Vertical Response vs. Perpendicular Wind Speed - Filtered Data**

As one would expect, since the perpendicular wind speed is less than or equal to the scalar wind speed, the RMS acceleration for a given scalar wind speed (Figure 4.6 & 4.8) are less than for a given perpendicular wind speed (Figures 4.10 & 4.11).

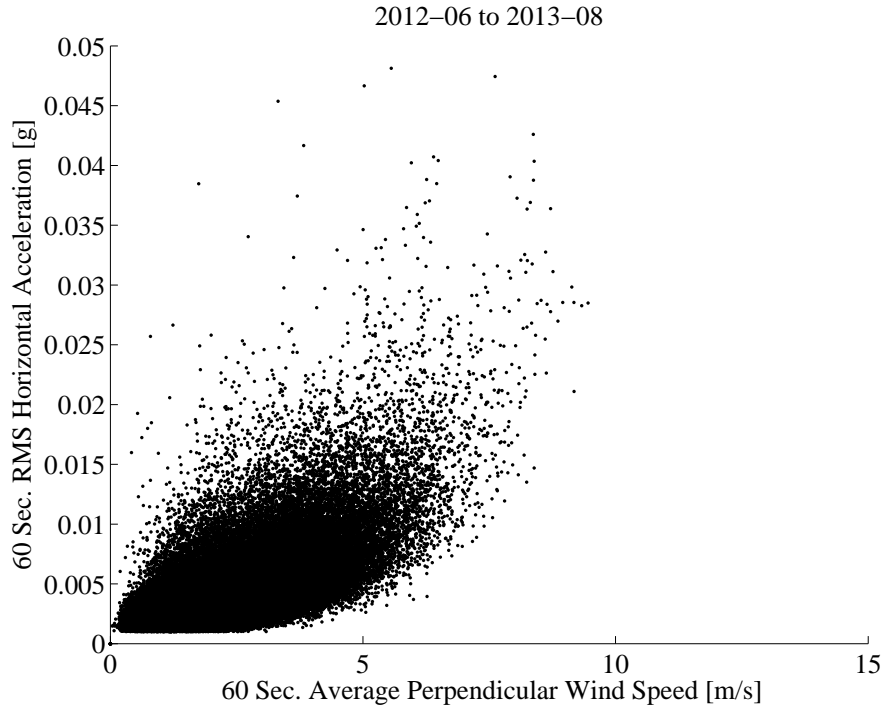


**Figure 4.11: Horizontal Response vs. Perpendicular Wind Speed - Filtered Data**

Finally note that there is a significant amount of scatter in Figure 4.6 through 4.11. That is, there is a comparatively large amount of variation in the RMS acceleration for a given 60 second average scalar wind speed (Figure 4.6 & 4.8) or a given perpendicular wind speed (Figures 4.10 & 4.11). This is due to the low damping in the signal support system and the high turbulence in the wind flow. This is illustrated by the response history in Figure 4.9 . As noted above there is a ring down period of relatively high mast arm response beginning at roughly 660 seconds in the record. Due to the low structural damping (damping ratio of roughly 0.2% for vertical motion and 0.55% for horizontal motion) the ring-down period last about 140 seconds (from 660 seconds to 800 seconds). Hence the mast arm response is higher than one would expect for the comparatively low wind speed during the ring down period.

## 4.4 Discussion

### 4.4.1 Vortex Shedding

The results obtained from the full-scale investigation show a general relationship between the response of the structure and wind speed. In addition, isolated instances of vortex shedding responses of the mast arm were observed (e.g. between roughly 630 and 660 seconds in Figure 4.9). Lacking from these results, however, were a large number of significant high amplitude vibrations at a sustained wind velocity of 13.2 mph, the estimated critical wind speed corresponding to resonance through a vortex shedding phenomenon. That is, significantly higher vibration amplitudes would have been observed if the wind velocity was sustained, for example, after the 660 second mark in Figure 4.9.

In addition, time history plots of the vertical vs. horizontal response at the tip of the mast-arm during estimated critical wind conditions showed a near circular motion rather than a response primarily in the vertical direction typical of vortex shedding induced vibrations. Figure 4.12 shows a 15-minute time history response which was observed during estimated critical wind speeds.

The absence of sustained high amplitude vibrations and the observation of bidirectional motion during estimated critical wind speeds indicate that although it is still likely that vortices were being shed from the mast-arm, the wind speed or direction changed before full resonance response could be achieved. Note that the number of cycles of motion at the critical velocity needed to reach 95% of the full resonance response is 240 cycles for a damping ratio of 0.2 %. For a structure with a natural frequency of 0.50 Hz, 240 cycles corresponds to two minutes of sustained wind speed. Recall that there were only 30 seconds of sustained wind speed for the record in Figure 4.9. This differs considerably from the results obtained at Texas Tech University (TTU) in which significant long-lasting large vibrations at

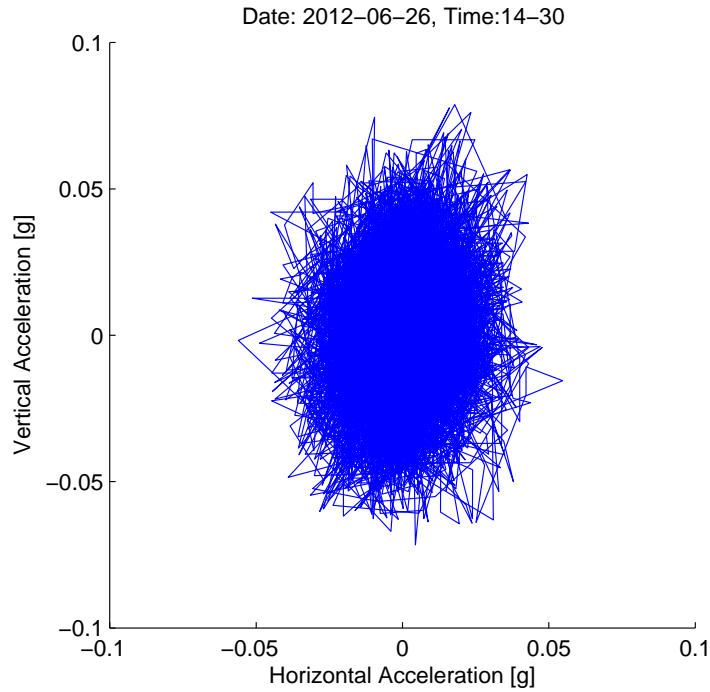


**Figure 4.12: Vertical vs. Horizontal Response at Tip of Mast-Arm**

certain wind speed and direction ranges, reflecting typical vortex shedding induced behavior, were observed [9, 10].

#### 4.4.2 Terrain

A likely reason for the differences seen between this investigation and the tests conducted at TTU is due to the differences in terrain which surround the field sites. These differences in terrain are shown via a set of aerial images of the experimental sites in Figures 4.13 and 4.14.

At the experimental site in Malta, NY, the site conditions are classified by Exposure Category B which is characterized as “urban and suburban areas, wooded areas, or other terrain with numerous closely spaced obstructions having the size of single-family dwellings or larger” [16]. At the TTU experiment site, the surrounding terrain are classified as Exposure Category C which is described as “open terrain with scattered obstructions having heights generally less than 30 ft including flat



Figure 4.13: Terrain Surrounding Malta, NY Structure [11]

#### 4.4.3 Turbulence Intensity

The amount of surface roughness, which is characterized by the ASCE Exposure Category, influences the turbulence intensity of the wind given in Equation 4.1[8].

The ASCE 7-10 Load Standard [16] includes a direct relationship between the turbulence intensity and the surrounding terrain through an exposure category parameter ( $c$ ). This formula, shown in Equation 4.2, also corrects for height differences between the equivalent height of the structure  $\bar{z}$  (ft) and the standard 33 ft (10 m) height.

$$I_{\bar{z}} = c \left( \frac{33}{\bar{z}} \right)^{1/6} \quad (4.2)$$

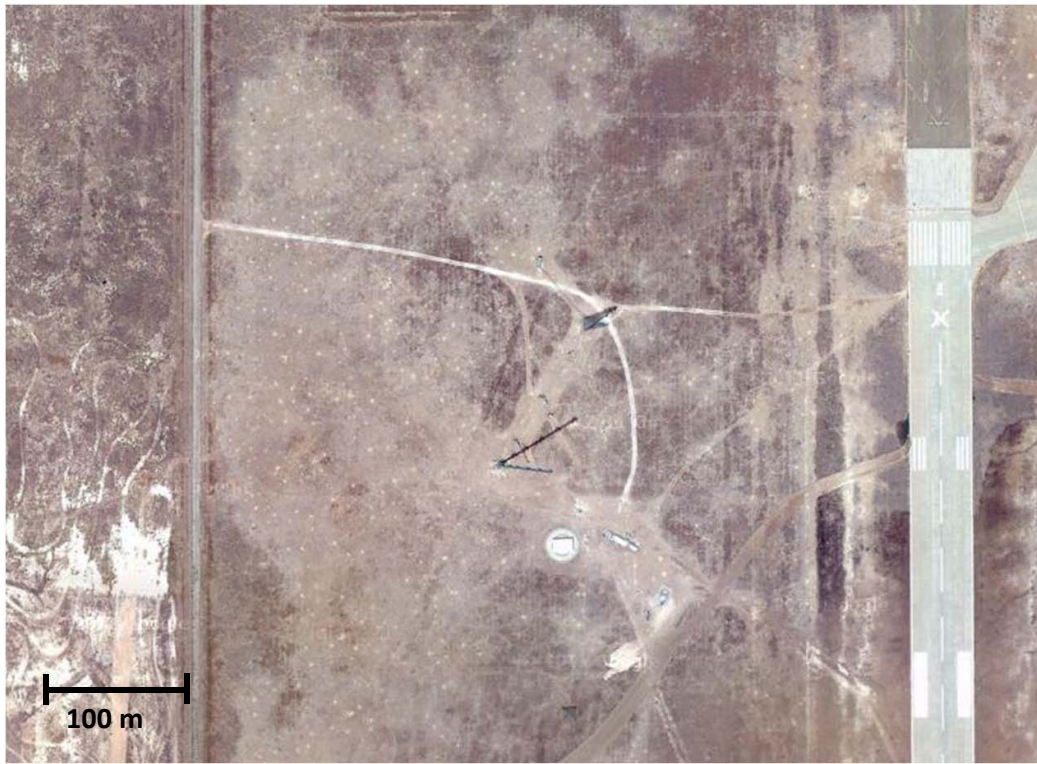


**Figure 4.14: Terrain Surrounding Tests at TTU [17]**

The turbulence intensities observed at the full-scale experiment site in Malta, NY are shown in Figure 4.15, a probability distribution plot of observed turbulence intensities based on 60-second values. The majority of the turbulence intensities for this project ranged from 0.1 to 0.4 (10 to 40%) with the average turbulence intensity equal to 0.32. This average turbulence intensity matches the expected turbulence intensity from ASCE 7-10 for Exposure Category B at a height of 21 ft (6.4 m) using the ASCE 7-10 specified exposure category parameter ( $c$ ) equal to 0.3 for Exposure Category B.

In contrast to the high turbulence intensity values observed in Malta, NY, much lower turbulence intensities were seen in the experiments conducted at TTU. The majority of the turbulence intensities fell in the 0 to 0.1 (0 to 10%) range [18]. In addition, results from TTU showed that the high amplitude vibrations occurred during low turbulent wind conditions with the highest of these vibrations occurring



at a turbulence intensity around 7% [10]. These low turbulent conditions were rarely observed in the Malta, NY study as indicated in Figure 4.15.

Because turbulence in the approach flow tends to make the shedding of vortices less coherent, the high turbulence wind observed in this full-scale experiment is likely the reason why high-amplitude vertical vibrations, which typically reflect a vortex shedding behavior, were not observed. Hence without this full resonant response, the structure is unlikely to experience prolonged high-amplitude vibrations.

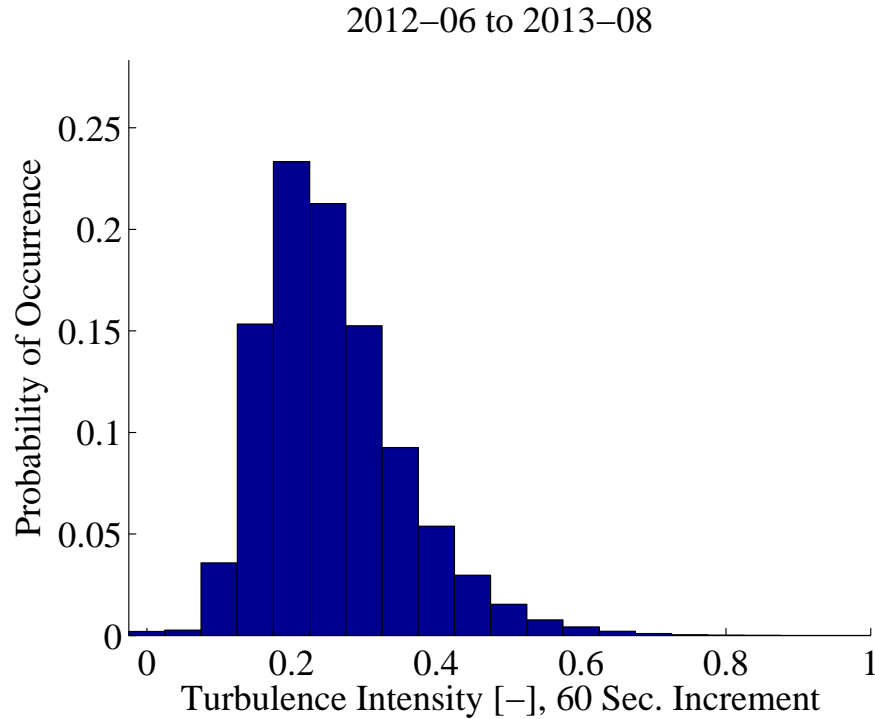


**Figure 4.15: Observed Turbulence Intensity Distribution at Malta, NY**

## 4.5 Conclusion

Wind and vibration data from the full scale experiment was collected over an 14 month period during which a general relationship was observed between the wind speed component acting perpendicular to the mast-arm and vibrations in both the vertical and horizontal directions. Occasionally, moderately large amplitude vertical



vibrations associated with a vortex shedding phenomenon were observed, however, sustained critical wind velocities leading to full structural resonance were not observed. When comparing the results obtained by this full-scale experiment to the results obtained from similar experiments at Texas Tech University (TTU), which do show sustained vortex shedding behavior, it was observed that there were significant differences in the turbulence intensities observed at the two project sites. These turbulence intensity differences were caused by distinctly different surrounding site conditions as categorized by the ASCE 7-10 Exposure Categories.

## CHAPTER 5

### WIND DATA ANALYSIS

#### 5.1 Introduction

A component of the investigation of wind-induced vibrations of mast-arm traffic signal structures is the analysis of historical data to determine mean wind speed climatology for New York State. Data was obtained from the National Climatic Data Center (NCDC) for 8 first order National Weather Service (NWS) stations. In addition, similar wind data analysis was performed for project specific wind data gathered from the full scale experiment site in Malta, NY (See Chapter 2 and Chapter 4). This chapter presents the results obtained through these analyses and compares project specific wind data and historical wind data for Albany, NY, the first order weather station nearest to the experimental site

#### 5.2 Wind Rose Definition

For both the project specific and NCDC wind data, directional analysis was undertaken and presented in the form of wind roses which shows the probability (displayed on the radial axis) that the wind blows from a particular direction (as indicated by the circumferential axis) exceeding a particular speed (as indicated by the color band and legend). A circular wind rose would indicate that wind with a particular velocity is equally likely to come from any direction. In contrast, for sites with dominant wind directions, the wind rose becomes increasingly non-circular pointing towards these prevailing directions.

A wind rose (having a directional component in comparison to a traditional probability distribution function which includes only wind speed data), is particu-

larly important for this study due to the fact that higher amplitude vibrations of the mast-arm occur when the angle of attack of the wind is near perpendicular to the mast-arm. In contrast, wind parallel to the arm results in relatively smaller vibrations

## 5.3 Historical Data

### 5.3.1 Site Locations

To complete the historical wind data analysis, 8 locations, having (NWS) first order stations were chosen. These airport sites are located in or near New York State and are shown on a location map in Figure 5.1. Details about these locations including the airport station names, coordinates, elevations, and the data periods are provided in Table 5.1 Because all of the chosen stations are located at airports,

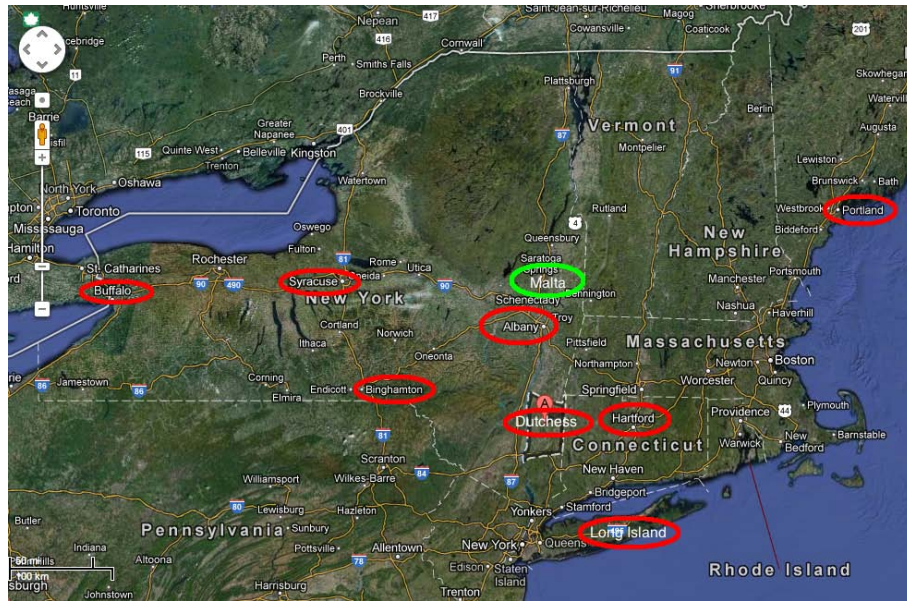


Figure 5.1: Location Map: Sites Used for Wind Analysis

the surrounding areas are reasonably well exposed, providing reliable consistent standardized data. For analysis, mean hourly wind speeds were collected for each location from the NCDC website database which can be located at the following

URL: <http://www.ncdc.noaa.gov/oa/climate/isd/index.php>. The 'mean hourly' wind speeds located in this database are recorded as 2-minute means at the top of each hour. When necessary, conversion from knots to m/s was undertaken (1 kt = 0.5144 m/s).

**Table 5.1: Airport Site Information**

Location	Airport Station	Lat.	Long.	Elevation[ft]	Data period	
					Start	End
Albany, NY	Albany County	42.743	-73.809	292	1/1/1973	2/31/2010
Binghamton, NY	Greater Binghamton	42.207	-75.98	1638	1/1/1973	7/1/2012
Buffalo, NY	Buffalo Niagara Intt	42.941	-78.736	705	5/18/1977	7/6/2012
Dutchess Co. NY	Dutchess County	41.627	-73.884	162	1/1/1973	7/6/2012
Hartford, CT	Bradley Intl	41.938	-72.683	179	1/1/1973	12/31/2010
Long Island, NY	Long Island MacArthur	40.794	-73.102	99	1/1/1973	7/31/2012
Portland, ME	Portland Intl	43.65	-70.3	63	1/1/1973	12/31/2010
Syracuse, NY	Syracuse Hancock Intl	43.111	-76.104	417	5/28/1968	7/6/2012

### 5.3.2 Data Validation

During the observation period, anemometer heights changed, especially after the introduction of ASOS (Automated Surface Observing System) in the 1990s. ASOS introduced a new system with more consistent observing practices, coding, and reporting standards for surface weather observations [20]. Table 5.2 records the anemometer height changes for each location. To account for these changes in

**Table 5.2: Anemometer Height Changes**

Location	Since	Anemometer height [ft]	Since	Anemometer height [ft]
Albany, NY	01/08/1963	20	08/01/1995	32.8
Binghamton, NY	01/21/1958	22	11/01/1995	26
Buffalo, NY	05/18/1977	33	12/01/1995	32.8
Dutchess Co. NY	11/16/1976	20	09/27/2000	26
Hartford, CT	08/15/1979	33	04/01/1996	32.8
Long Island, NY	12/15/1964	20	08/01/1999	26
Portland, ME	05/28/1963	21	11/01/1993	32.8
Syracuse, NY	10/06/1964	20	08/01/1994	26

anemometer heights, all data was converted to standard 33 ft (10 m) height using

the ASCE 7-10 power law shown in Equation 5.1.

$$\frac{V_z}{V_{z=33'}} = \left(\frac{z}{33}\right)^{\bar{\alpha}} \quad (5.1)$$

In this equation,  $z$  is the height of the anemometer [ft] and  $\bar{\alpha}$  is a power law exponent based on exposure category. For exposure C (airports), this constant is equal to  $1/6.5$  ( $= 0.154$ ).

Only ASOS data has been used in analyzing mean wind speed climatology because of the consistent approach to data recording afforded by the automated technology.(i.e for Albany from 08/01/1995 to 12/31/2010).

### 5.3.3 Methodology and Historical Wind Roses

Using the mean-hourly wind speeds downloaded from the NCDC database, a cumulative frequency distribution matrix was created for each location wherein each matrix cell indicates the frequency of a wind speed being exceeded from a certain direction within the data set. As one might expect, for a given wind direction the probability is a decreasing function of wind speed. A portion of a matrix for Albany NY is shown in Figure 5.2 below. The values in this matrix were then plotted radially to create the wind rose The resulting wind rose for Albany, NY is shown

		Wind Speed					
Wind Direction		>1 m/s	>2 m/s	>3 m/s	>4 m/s	>5 m/s	>6 m/s
	0	0.0416	0.0381	0.0245	0.0132	0.0064	0.0039
	10	0.0308	0.0281	0.0198	0.0123	0.0069	0.0044
	20	0.0236	0.0214	0.0153	0.0099	0.0052	0.003
	30	0.0143	0.0124	0.0079	0.0047	0.0025	0.0016
	40	0.0115	0.0098	0.0053	0.0026	0.0012	0.0006
	50	0.0079	0.0064	0.003	0.0015	0.0007	0.0003
	60	0.0068	0.0052	0.0021	0.0008	0.0003	0.0001
	70	0.0053	0.0039	0.0014	0.0005	0.0002	0.0001
	80	0.0043	0.0028	0.0007	0.0003	0.0001	0.0001
	90	0.0049	0.0035	0.001	0.0004	0.0001	0.0001
		⋮					

Figure 5.2: Cumulative Probability Distribution Matrix Example

in Figure 5.3, while wind roses for all locations are located in Appendix D. For Albany, NY, the strongest, most frequent winds come from the south (170°), the northwest (290°), and, to a lesser extent, the north (10°). Wind speeds are plotted in m/s ( $1\text{m/s} = 2.24\text{mph}$ )

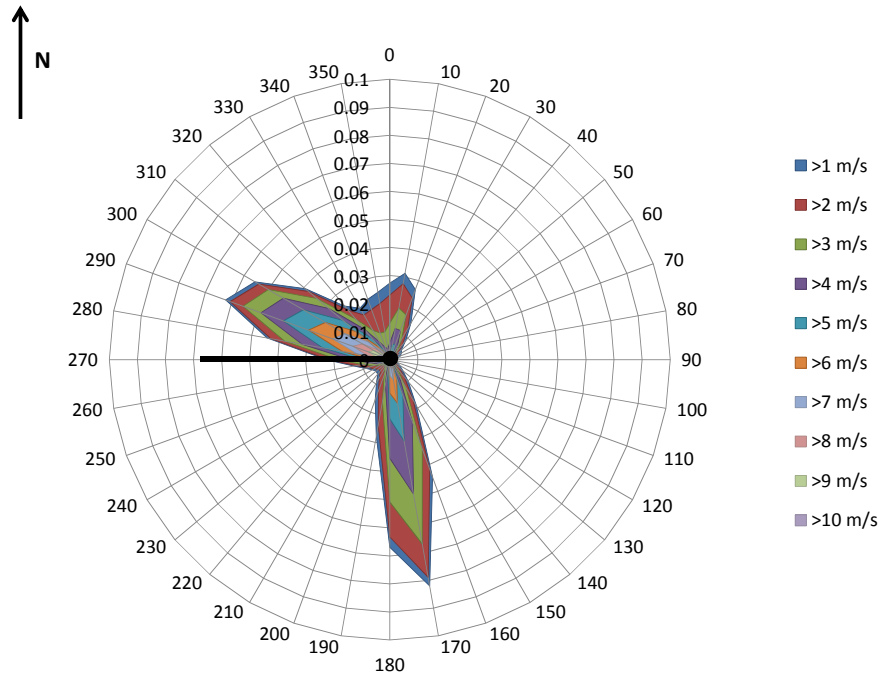


**Figure 5.3: Observed Wind Rose for Albany, NY using Historical NCDC Data**

#### 5.3.4 Fitted Probability Distributions

The observed cumulative frequency distributions were fitted with probability distribution functions in order to advance the analysis.

Best-fit distributions for all directions were established using the inverse CDF method. Among methods for finding best-fit probability distributions, the inverse Cumulative Distribution Function (CDF) method [21] was selected because it is easily programmed and provides a simple, graphical technique that can be generalized for any distribution form without the need for specific types of plotting papers.

Figure 5.4 shows that the best-fit distribution for all directions at Albany is a Weibull distribution as this distribution is closest to the 1:1 reference line.

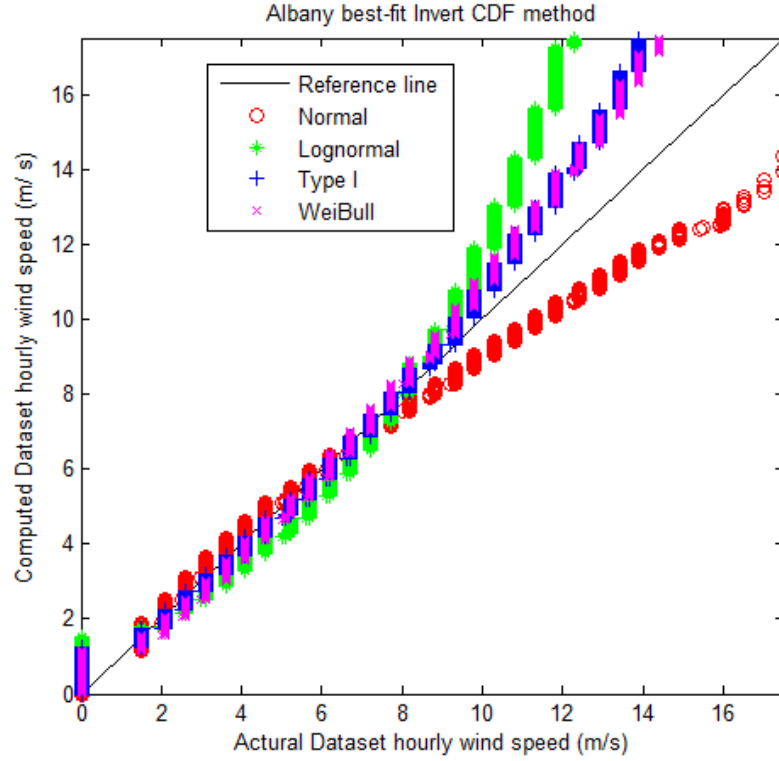


**Figure 5.4: Best-Fit Distributions for Albany, NY (All directions included)**

Best-fit probability distributions were also obtained for each  $10^\circ$  direction band (i.e.  $10^\circ, 20^\circ, \dots, 360^\circ$ ). The results from this analysis for the Albany, NY station are shown in the Table 5.3 where WB, TPI and Log indicate Weibull, Type 1 and Lognormal respectively. Through this analysis, it is shown that the best-fit distribution type differs for each direction. However, in order to use a consistent model the Weibull distribution was selected when modeling all of the wind speed directional distributions. When considering all directions, the Weibull distribution formula is shown in Equation 5.2. In Equation 5.2, A equal to 1 - the percentage of

calms (zero wind speed), while  $k$  and  $c$  are Weibull distribution parameters.

$$P(V > V_0) = A \times \exp [-(V_0/c)]^k \quad (5.2)$$

When considering specific wind directions, the following relation applies:

$$P(V > V_0, \theta) = A(\theta) \times \exp [-(V_0/c(\theta))]^{k(\theta)} \quad (5.3)$$

where:  $A(\theta)$  is the probability of wind in the  $\theta$  direction sector

( $\sum A(\theta) = A$ ) while  $k(\theta)$ ,  $c(\theta)$  are the Weibull distribution parameters in the  $\theta$  direction sector.

**Table 5.3: Best-fit distribution parameters for each direction**

Direction (°)	Best-fit Distribution	Weibull Parameters			Direction (°)	Best-fit Distribution	Weibull Parameters		
		$A(\theta)$	$c(\theta)$	$k(\theta)$			$A(\theta)$	$c(\theta)$	$k(\theta)$
All	WB	0.804	3.668	1.319					
10	TPI	0.031	3.962	2.402	190	TPI	0.028	3.830	2.249
20	TPI	0.027	4.183	2.391	200	Log	0.015	3.133	2.503
30	WB	0.015	3.908	2.301	210	Log	0.010	3.118	2.442
40	TPI	0.009	3.667	2.216	220	TPI	0.007	3.225	2.162
50	TPI	0.005	3.337	2.098	230	Log	0.006	3.570	2.198
60	Log	0.005	3.027	2.132	240	Log	0.007	3.956	2.080
70	Log	0.004	2.921	1.958	250	TPI	0.009	4.573	2.162
80	Log	0.003	2.771	2.114	260	TPI	0.013	5.022	2.275
90	Log	0.002	2.652	2.374	270	TPI	0.023	5.587	2.267
100	Log	0.002	2.368	2.609	280	WB	0.044	6.271	2.336
110	Log	0.003	2.718	1.811	290	WB	0.062	6.844	2.519
120	TPI	0.004	2.785	2.421	300	WB	0.056	6.728	2.596
130	TPI	0.006	2.929	2.348	310	WB	0.039	6.127	2.468
140	WB	0.010	3.319	2.317	320	WB	0.025	5.107	2.302
150	WB	0.019	4.003	2.373	330	TPI	0.021	4.012	2.132
160	Log	0.045	4.742	2.545	340	Log	0.023	3.374	2.359
170	WB	0.082	5.010	2.744	350	TPI	0.024	3.224	2.588
180	WB	0.067	4.760	2.554	360	TPI	0.027	3.472	2.391

Using the Weibull probability distribution parameters, the "fitted" wind rose is presented in Figure 5.5 for Albany, NY. Note that it is quite close to the "observed" rose in Figure 5.3. Fitted (model) wind roses for all locations are included in Appendix E.



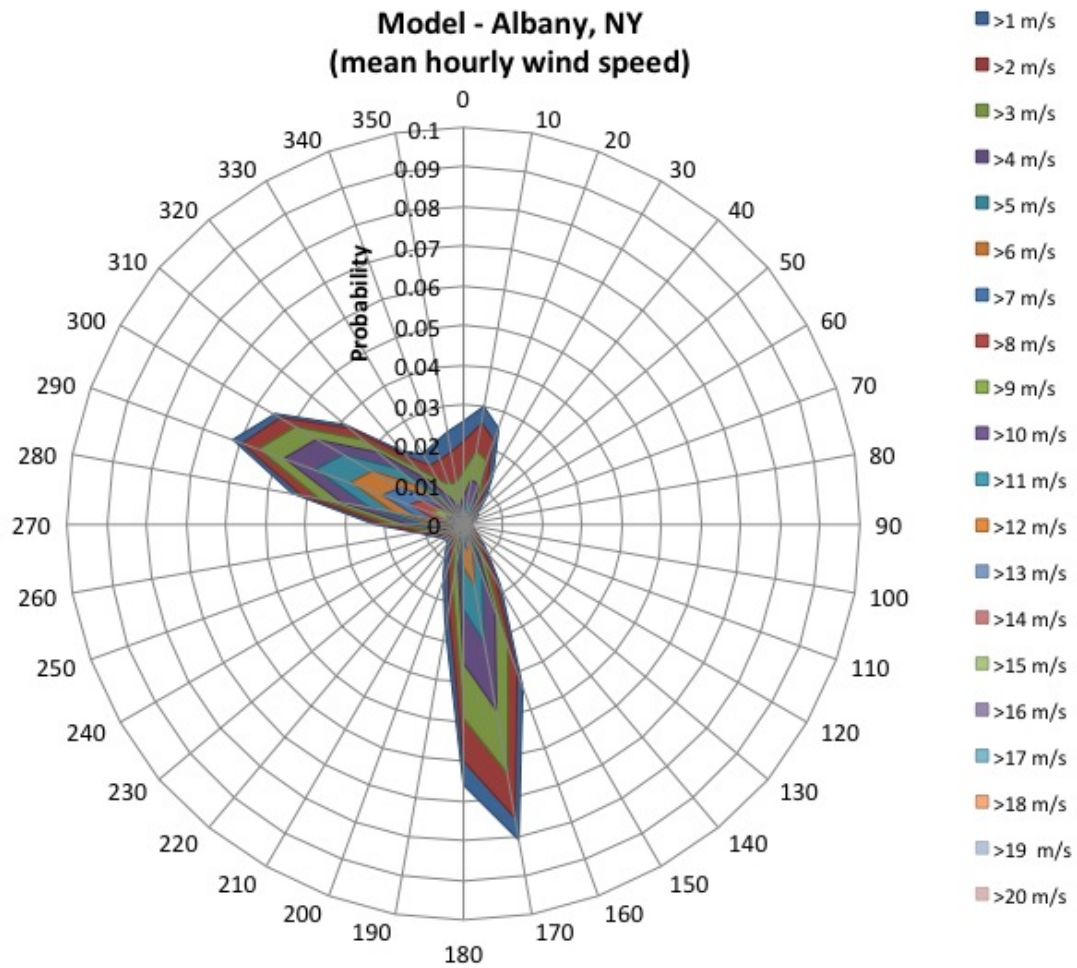


Figure 5.5: Fitted Wind Rose for Albany, NY using the WB distribution

## 5.4 Project Data

### 5.4.1 Methodology and Project Wind Roses

A Malta site specific wind rose was created using data collected between the months of June 2012 and August 2013. Wind data summary statistics were calculated for each 30 second increment of data during these months. These statistics included average wind speed (using an arithmetic mean) and average wind direction (using circular averaging techniques outlined in Appendix F).

These summary statistics were used to create a cumulative frequency distri-

bution matrix in the manner described in Section 5.3.3 of this report. The values in this matrix were then plotted radially to create the project wind rose shown in Figure 5.6. In addition, this same information was plotted in Figure 5.7 using a 0.5 m/s wind speed increment in order to better visualize the data.

It should be noted that although time increments with low wind speeds were removed from the data set used for most of the vibration analysis in Chapter 4, the entire data set was used to create this wind rose.

#### 5.4.2 Discussion and Comparison with Historical Data

For both of the Malta site wind roses shown in Figure 5.6 and 5.7, the wind direction angle is taken with respect to Project North, which is based on the orientation of the mast arm, rather than True North. For this investigation, Project North is defined as being perpendicular to the length of the mast arm and offset from True North by  $33^\circ$  as shown in Figure 2.3.

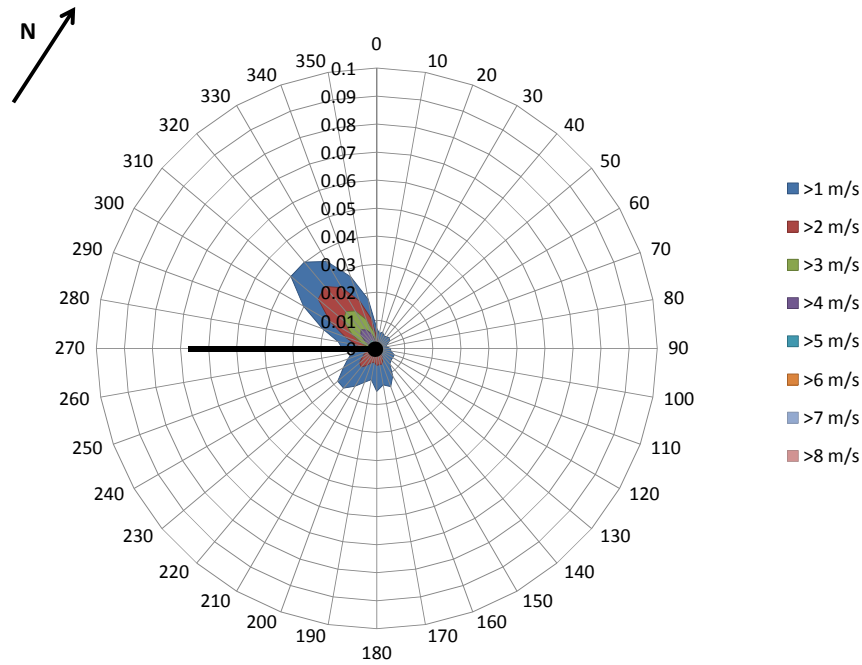
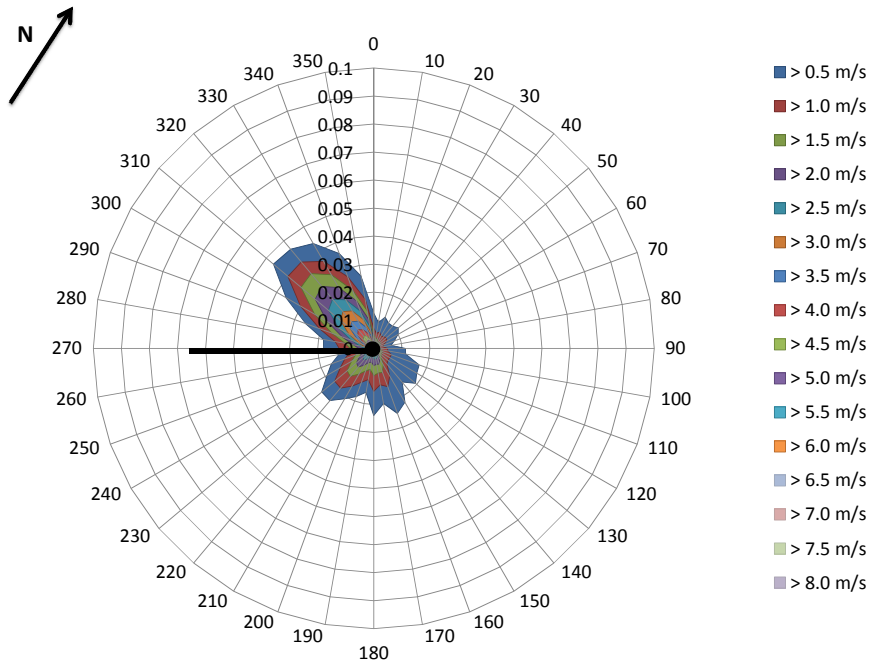


Figure 5.6: Observed Wind Rose at Malta, NY ( $0^\circ$  is Project North)

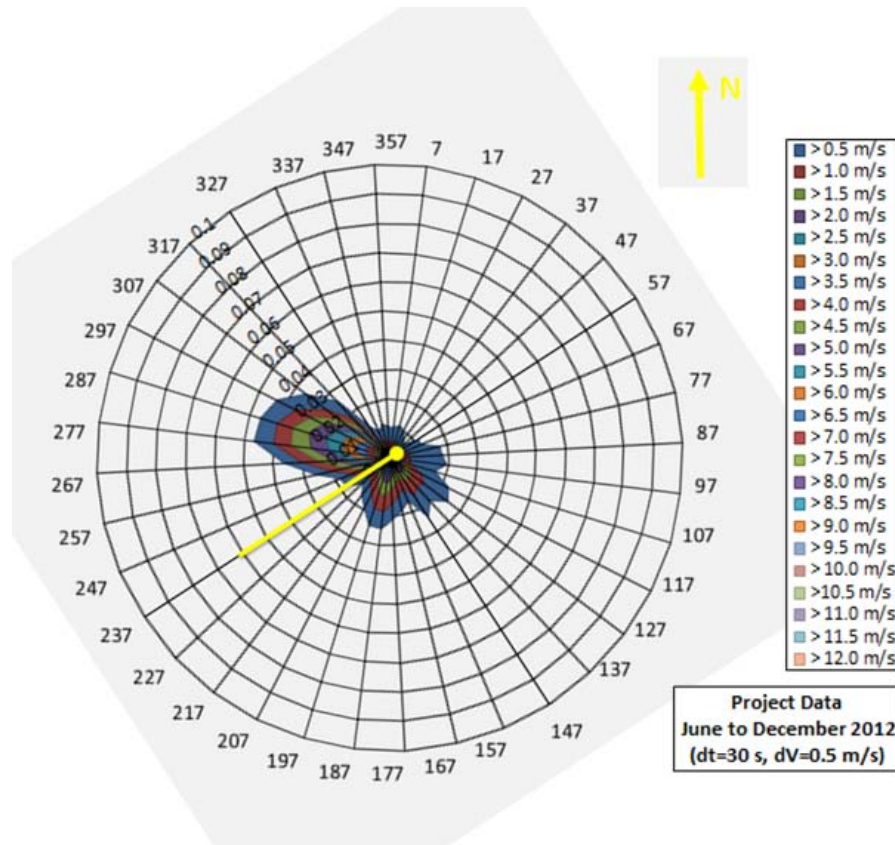


**Figure 5.7: Observed Wind Rose at Malta, NY: 0.5 m/s Wind Speed Increment (0° is Project North)**

Therefore, to compare the project wind roses with the historical wind roses, the project wind rose was rotated  $-33^\circ$ . This rotated wind rose is shown in Figure 5.8 and the angles shown on the circumferential axis represent the angle with respect to True North.

By comparing the historical long-term wind rose at Albany Airport to the site specific at Malta NY, one finds that the wind speeds collected at Malta during this 14 months investigation are lower than those observed at Albany Airport. This is to be expected due to the relatively sheltered site conditions at the investigation site in Malta, NY.

In addition to lower wind speed magnitudes, the directional distribution (as shown by the shape of the wind roses) is altered between the historical airport data and the site specific data. The major prevailing wind direction (approximately  $320^\circ$  from Project North or  $290^\circ$  from True North at Albany) is evident in the Malta wind



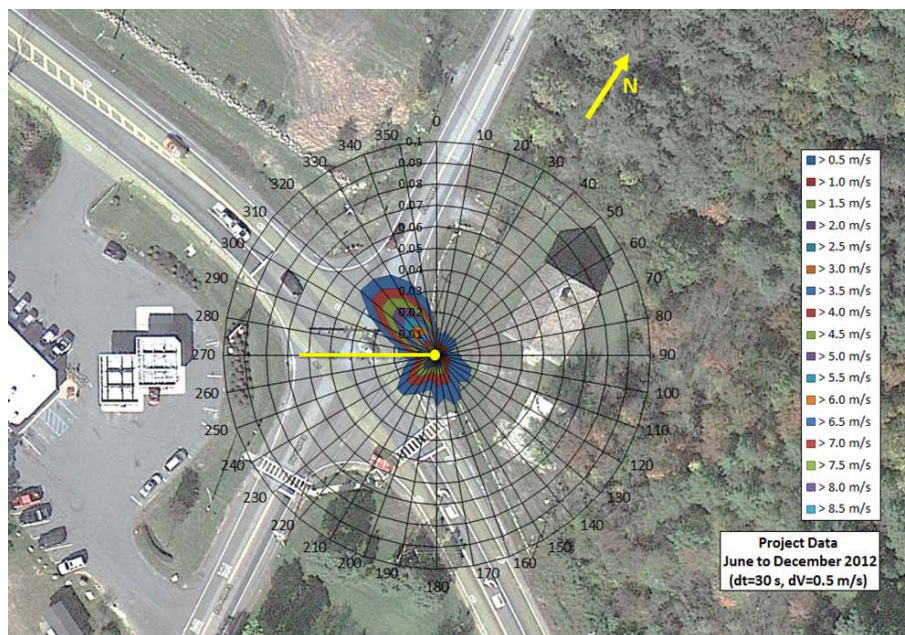


Figure 5.9: Project Wind Rose Overlaid on Site Map

## CHAPTER 6

### MAST-ARM VIBRATION MODEL

#### 6.1 Introduction

The natural frequency of the structure is one of the two most important dynamic characteristics of Mast-Arm structures. As mentioned in Chapter 2, the instrumentation measures the acceleration response of the Mast-Arm. However, the fatigue life determination requires the displacement response (as will be shown in Chapter 7). Figure 6.1 shows a sample of the vertical and horizontal acceleration response of the mast arm and the corresponding wind speed and direction. Figure 6.2 show the Fourier Amplitude spectrum for both the mast-arm accelerations as well as the wind speed. Note that the mast-arm vibration is nominally at its natural frequency (0.52 Hz for vertical direction and 0.50 Hz for horizontal direction) whereas the fluctuating component of wind speed is at much low frequency (roughly around 0.05 Hz). Since the mast-arm response is at its natural frequency, one needs the natural frequency to convert from the measured acceleration response to the displacement response.

There are three main methods to determine the natural frequency of a mast-arm structure; eigenvalue analysis of a computerized structural model, approximate energy methods suitable for hand calculation, and physical observation of the free vibration response. All three methods are described in this chapter.

#### 6.2 Eigenvalue Analysis

The Chapter 3 presents a detailed description of the eigenvalue analysis of the Malta test structure. That information is summarized herein. The mast arm

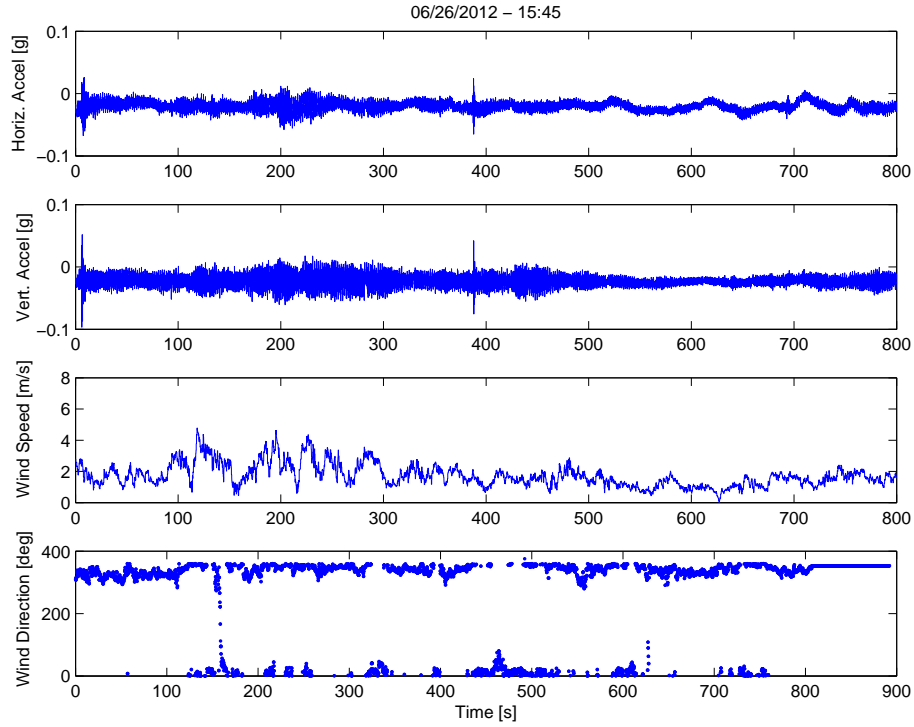


**Figure 6.1: Time History Response: a)Measured horizontal acceleration at mast-arm tip, b)Measured vertical acceleration at mast-arm tip, c)Measured wind speed, d)Measured wind direction**

structure was made of ASTM A572 Gr 65 steel, as specified on the plans provided. Details about material properties are summarized in Table 6.1. Figure 6.3 shows

**Table 6.1: Material Properties**

Material Property	Value [SI Units]	Value [English Units]
Mass Density	7850 kg/m <sup>3</sup>	490 pcf
Young's Modulus	200 GPa	29,000 ksi
Poisson's Ratio	0.25	0.25

the structure geometry. The traffic signal structure has a cantilevered mast-arm spanning 25 m (82 ft) in length and a tapered diameter ranging from 432 mm (17 in) at the fixed end to 288 mm (11.3 in) at the free end of the mast arm. The vertical post which supports the mast-arm is 5.8 m (19 ft) tall and has a tapered diameter ranging from 457 mm (18 in) at the base to 421 mm (16.6 in) at the top.



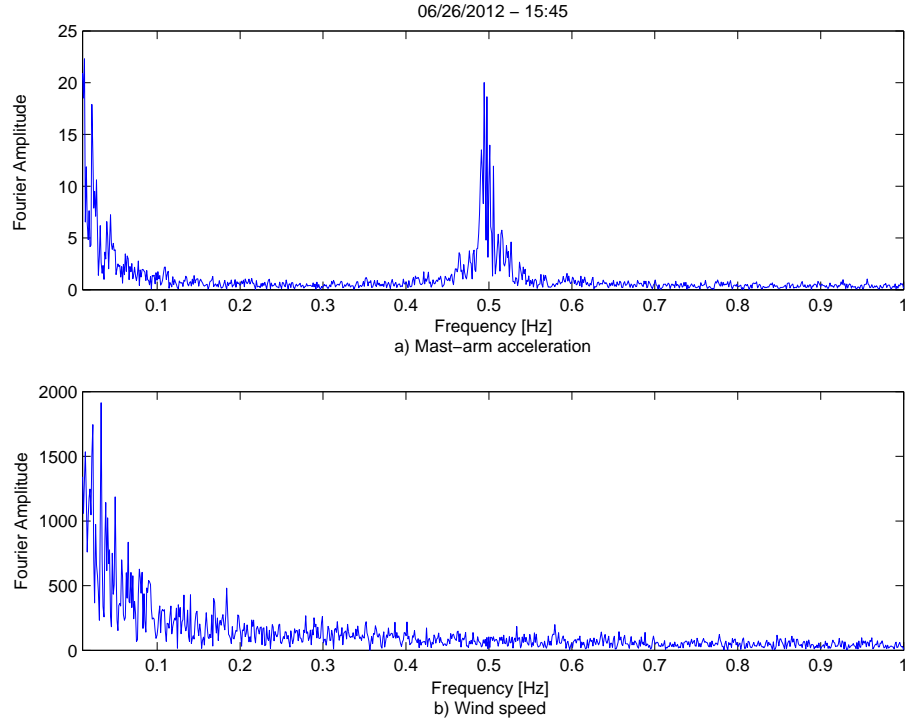


**Figure 6.2: Fourier Amplitude Spectrum: a)Mast arm acceleration, b)Wind speed**

The traffic signals were assumed to act as point masses. The locations of the traffic signals along the length of the mast arm were estimated from a combination of photographs and field measurements since these dimensions were not shown on the plans provided. The masses of the traffic signals were estimated to be 60 lb (27 kg) for the single sets of signals and 120 lb (54 kg) for the multi-sets and were applied along the centerline of the mast arm. The estimated locations and masses of the Malta traffic signals are summarized in Table 6.2.

An ABAQUS/CAE computer model was built using 616 elements - 416 hexagonal elements for the mast-arm and 80 elements for the pole. An eigenvalue analysis (user option within ABAQUS/CAE) gave natural frequency of 0.57 Hz for vertical (Z-direction) and 0.68 Hz for horizontal (Y-direction).





and the frequency domain. These tests were repeated for each direction at which point it was determined that the data collected was consistent.

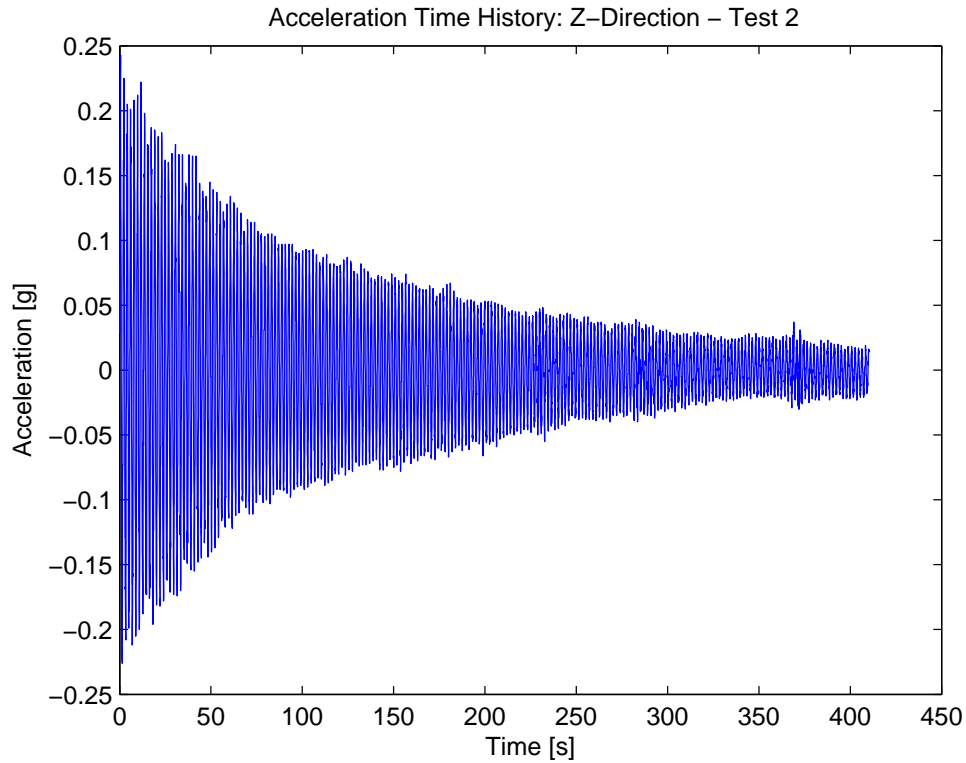


**Figure 6.4: Excitation Test - Z-direction (Test 2): Acceleration Time History Response**

To determine the natural frequency of the traffic signal structure both in the y and z-directions, the data collected from the free vibration tests was converted from the time domain to the frequency domain and Fourier amplitude spectra were plotted. In the case of free vibration, the peak seen on a Fourier amplitude spectrum indicates the natural frequency of the system. From the Fourier amplitude spectra for the excitation ("pluck") tests, it was determined that the traffic signal structure has a natural frequency of 0.49 Hz in the y-direction and 0.52 Hz in the z-direction. The acceleration time history response and corresponding Fourier amplitude spectrum for the (second) free vibration test in the z-direction are shown in Figures 6.4 and 6.5.

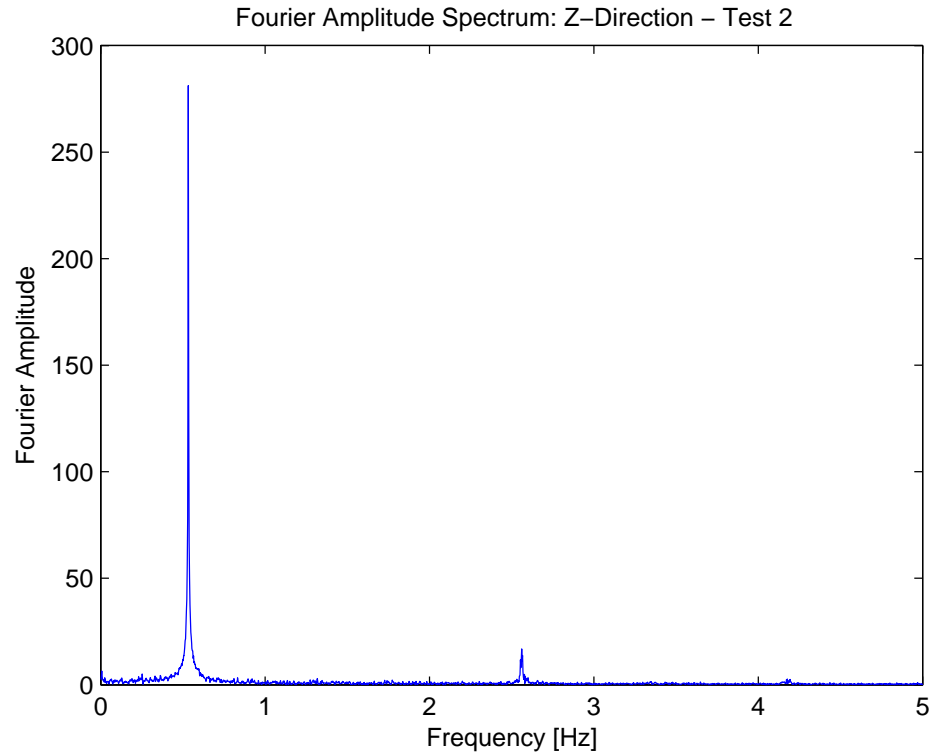


**Figure 6.5: Excitation Test - Z-direction (Test 2): Fourier Amplitude Spectrum**

Note that the SEISMOSIGNAL/ Fourier amplitude spectrum method required that the mast-arm be instrumented. For initial screening purposes, the natural frequency can be roughly estimated by exciting the mast-arm in free vibration as above (boom lift required) and then measuring the time for 20 to 30 complete cycles of motion. The natural frequency is the number of cycles divided by the time period. Such field tests at the Malta site resulted in an estimated natural frequency of approximately 0.5 Hz. Note the "pluck" test is the only way to determine damping of the structure.

If the structure is instrumented, the damping ratio can be determined by fitting an exponential decay to the observed vibration as shown in Chapter 3, as well in Figure 6.4. Alternately, the damping ratio can be estimated by measuring the number of cycles for the free vibration during the pluck test to reduce by half.

From Equation 3.14 the estimated damping ratio is

$$\xi = \frac{0.693}{2\pi n} \quad (6.1)$$

where  $n$  is the observed number of cycles for the free vibration to reduce by a half. For example, in Figure 3.9 the vibration level is about 0.12 at 75 seconds while it drops to about 0.06 (reduction of 1/2) at roughly 160 seconds. Since the natural frequency is about 0.5 Hz (2 second natural period) the 85 seconds to reduce to half the vibration level corresponds to 42.5 cycles. From Equation 6.1 the damping ratio became 0.0026 or 0.26 %.

## 6.4 Approximate Energy Method, Rayleigh's Method

Rayleigh's Method is based on the principle of conservation of energy. A simple analytical model suitable for hand calculation is to approximate the mast-arm as a cantilever with a fixed support at the pole. The cantilever has distributed mass corresponding to the self weight of the arm itself, plus concentrated masses corresponding to the signals. One begins by assuming the deflection shape of the mast-arm,  $\psi(x)$ . Under dynamic vibration, the displacement of any point in the mast-arm can be express as  $u(x, t) = z_0 \sin(\omega_n t) \psi(x)$ , where  $x$  is the distance from the free end,  $z_0$  is the amplitude of the generalized coordinate  $z(t)$  and  $\omega_n$  is natural vibration frequency (in radians per second). The total maximum potential energy of the system over a vibration cycle is equal to its strain energy associated with the maximum displacement  $u_0(x) = z_0 \psi(x)$ :

$$E_s = \int_0^L \frac{1}{2} EI(x) [u_0''(x)]^2 dx. \quad (6.2)$$

where  $E_s$  is total potential energy,  $E$  is Young modulus,  $I(x)$  is moment of

inertia at this point  $x$ ,  $u_0''(x)$  is the curvature or second derivative of  $u_0(x)$  with respect to  $x$ .

The total maximum kinetic energy of the system over a vibration cycle is associated with maximum velocity  $\dot{u}_0(x) = z_0\omega_n\psi(x)$ :

$$E_k = \int_0^L \frac{1}{2}m(x)[\dot{u}_0(x)]^2 dx + \sum_{i=1}^N \frac{1}{2}M_i(x)[\dot{u}_0(x_i)]^2 \quad (6.3)$$

where  $E_k$  is total kinetic energy,  $m(x)$  is the mass per unit length of the mast-arm at distance  $x$  from free end,  $\dot{u}_0(x)$  is maximum velocity at point  $x$ ;  $M_i$  is the  $i$ -th traffic signal mass at the distance  $x_i$  from the free end, and  $\dot{u}_0(x_i)$  is the maximum velocity of the  $i$ -th traffic signal mass. From conservation of energy  $E_s = E_k$  or

$$\int_0^L \frac{1}{2}EI(x)[z_0\psi''(x)]^2 dx = \int_0^L \frac{1}{2}m(x)[z_0\omega_n\psi(x)]^2 dx + \sum_{i=1}^N \frac{1}{2}M_i(x)[z_0\omega_n\psi(x_i)]^2 \quad (6.4)$$

Or

$$\omega_n^2 = \frac{\int_0^L \frac{1}{2}EI(x)[z_0\psi''(x)]^2 dx}{\int_0^L \frac{1}{2}m(x)[z_0\omega_n\psi(x)]^2 dx + \sum_{i=1}^N \frac{1}{2}M_i(x)[z_0\omega_n\psi(x_i)]^2} \quad (6.5)$$

Appendix B presents the application of Rayleigh's method to the Malta mast-arm signal support. Note that the approximate natural frequency from Appendix B is  $f_n = \frac{\omega_n}{2\pi} = 0.55$  Hz which was reasonably close to our results from both the "pluck" test and the finite element model.

## 6.5 Conclusion

The "pluck" test and Rayleigh's method are two easy-to-use methods to determine the natural frequency of a mast-arm structure. It is expected that NYSDOT standard practice will be to perform a "pluck" test on any mast-arm structure un-

der investigated for potential fatigue problems. Rayleigh's method can then be used to check the site measured frequency and/or investigate the effects of adding or subtracting traffic signals.

## CHAPTER 7

### FATIGUE LIFE ESTIMATION

#### 7.1 Introduction

In recent years, fatigue failure of traffic signal has been reported in several states. In-service fatigue cracks in these structures have mostly occurred at the connection of the mast-arm with the vertical pole. This chapter will discuss how to estimate the fatigue life based on the wind climate and the characteristic of the mast-arm.

#### 7.2 Fatigue

For traffic signals, the primary design force is the wind load. Because of its lightweight slender configuration, the long-mast arm structures are quite flexible with a typical fundamental natural frequency on the order of 0.5 Hz. In addition, the structures possess extremely low damping, usually less than 0.6 % of critical. These dynamic characteristics make traffic signals highly susceptible to large amplitude sustained vibrations at their natural frequencies as a result of the aerodynamic effects of vortex shedding as well as buffeting from natural wind gusting. Apart from large deflections, frequent wind-induced vibration can impart numerous cycles of stress at the various welded connections, which conceivably could result in fatigue damage.

The current applicable AASHTO specification for these structures (AASHTO 2009) establishes the Constant-Amplitude Fatigue Limit (CAFL) stress at the connection of the horizontal mast arm to the vertical pole as Category E', irrespective of the specific geometric details of the connection. For the various fatigue categories,

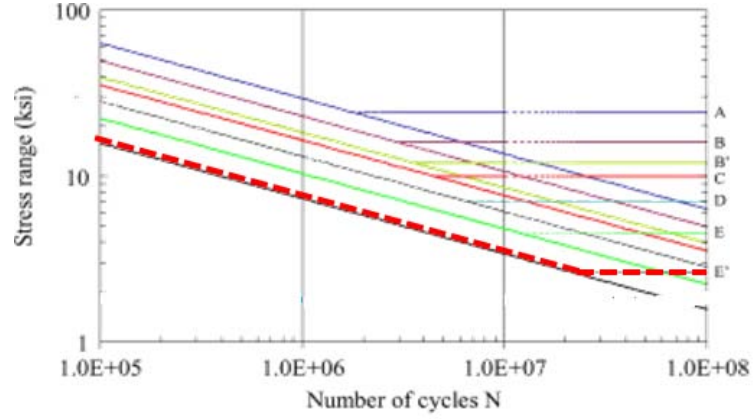


**Figure 7.1: Stress-number of cycles curves for various connection detail catagories of ASTM A572 Gr 65 Steel (from Kacin, Rizzo, Tajari, 2010)**

AASHTO provides the corresponding fatigue limit stress but does not provide the Stress-Number of cycles (S-N) curve. The S-N curves is a plot of the acceptable stress as a function of the number of cycles from Kacin, Rizzo, and Tajari(2010). For example Figure 7.1 present the S-N curve for the ASTM A572 Gr 65 steel from Kacin, Rizzo, and Tajari(2010). Note that the stress range is the difference between the maximum and minimum stress at a point of interest. As one might expect, the allowable stress range is a decreasing function of the number of cycles. However for each fatigue category, there is a stress range (20 MPa or 2.9 ksi for Category E') below which an infinite number of cycles are allowable. Figure 7.2 sketches the stress time history for nominally uniform time varying wind induced stress  $\sigma_w$  with zero mean in combination with constant stress due to mast-arm self-weight,  $\sigma_{sw}$ .

Hence the maximum stress  $\sigma_{max}$

$$\sigma_{max} = \sigma_{sw} + \sigma_w \quad (7.1)$$



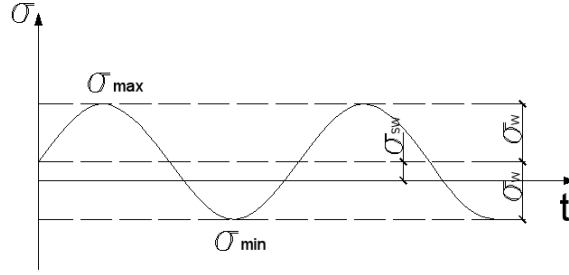


**Figure 7.2: Stress time history**

while the minimum stress  $\sigma_{min}$

$$\sigma_{min} = \sigma_{sw} - \sigma_w \quad (7.2)$$

The stress range  $\Delta\sigma$  is

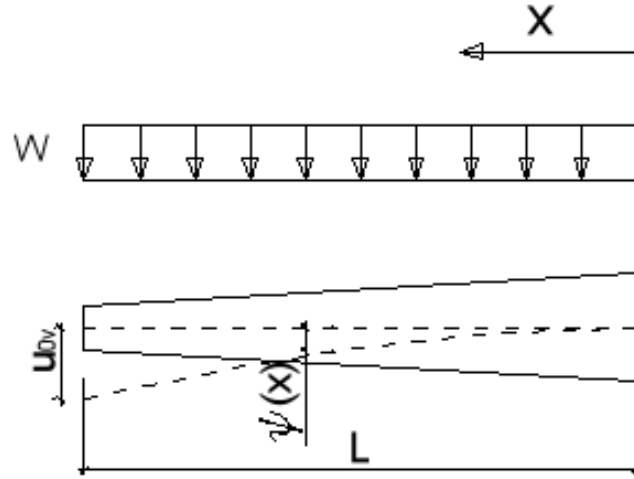
$$\Delta\sigma = \sigma_{max} - \sigma_{min} = 2\sigma_w \quad (7.3)$$

Note that the self weight stress, being constant, does not influence the stress range.

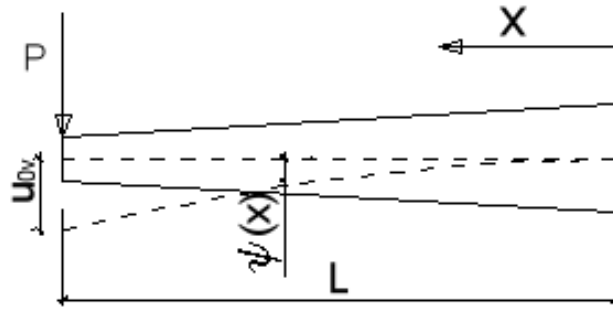
### 7.3 Stress Range

The acceleration response of the mast-arm was measured, however, in order to calculate the stress range, the tip displacement is of particular interest. Based on that tip displacement, the stress at the pole/mast-arm connection was determined by considering two separate load distributions; a uniformly distributed load across the whole mast-arm (see Figure 7.3a), and a concentrated point load at the mast arm tip (see Figure 7.3b). For vertical motion the largest stress is at the top (point A) and the bottom (point D) of the mast-arm cross-section as shown in Figure 7.4

$$\sigma_v = \frac{M_v r_2}{I} \quad (7.4)$$



a) Uniform Load



b) Point Load

**Figure 7.3: Two Load Distributions Considered: a)Uniform Load, b)Point Load**

where  $M_v$  is the bending moment due to vertical loading,  $r_2$  and  $I$  are the outer mast-arm radius and moment of inertia of the mast-arm cross-section at the pole/mast-arm connection. For horizontal motion the largest stress is at the left (point E) and right sides (point C) (mid height) of the mast-arm cross-section as shown in Figure 7.4.

$$\sigma_h = \frac{M_h r_2}{I} \quad (7.5)$$

where  $M_h$  is the bending moment due to horizontal loading.

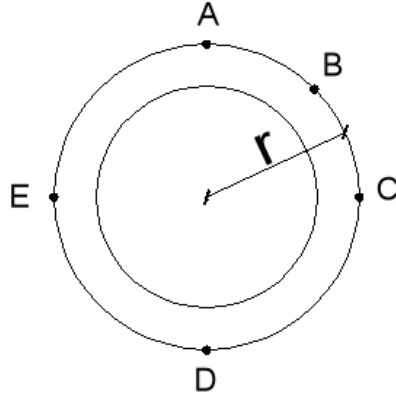


**Figure 7.4: Mast-arm Cross Section**

In general the vertical motion and horizontal motion are not in phase (maximum vertical motion not at the same time as maximum horizontal motion). However herein it is conservatively assumed that the horizontal and vertical motions are in phase. In that case peak stress is at point B.

$$\sigma = \frac{0.707(M_v + M_h)r_2}{I} \quad (7.6)$$

Figure 7.5 shows the frequency content of the mast-arm tip motion as characterized by the Fast Fourier Transform (FFT) of the acceleration response. It clearly indicates that most of the acceleration response is at the natural frequency of the traffic signal support  $f_n=0.5$  Hz. Since the motion is at the natural frequency the displacement can be determined by dividing the acceleration by  $\omega_n^2$  (where  $\omega_n=2\pi \times f_n$ ). Noting that the acceleration was measured in units of  $g$ , the tip displacement in cm,  $u_0$ , becomes

$$u_0 = \frac{\ddot{u}_0}{(2\pi f_n)^2} \times \frac{980cm/s^2}{1g} \quad (7.7)$$

or  $u_0(cm) = 99.4 \times \ddot{u}_0(g)$  ( $u_0(in) = 39.1 \times \ddot{u}_0(g)$ ) where  $\ddot{u}_0$  is the measured tip acceleration in units of  $g$ . Knowing the tip displacement, the the stress range at the

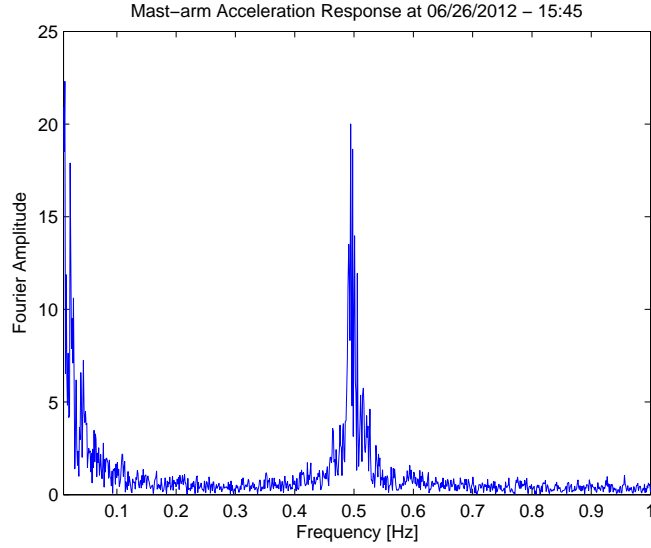


**Figure 7.5: Fourier Amplitude Spectrum for Mast-arm Acceleration Response**

mast-arm pole connection was established by considering two idealized distributions of load on the cantilevered mast-arm: uniform load and point load at the tip.

- Case 1: Uniform load

For an assumed uniform load  $w$  (N/m), the moment in the mast arm is  $M = \frac{(L-x)^2 \times w}{2}$ , where  $x$  is the distance from the pole. From elementary beam theory, the moment curvature relation is  $M = EI \frac{\partial^2 \psi(x)}{\partial x^2}$ , where  $E$  is Young's modulus = 200 GPa (29,000 ksi) and  $I$  is the mast-arm moment of inertia. Assuming the mast-arm is a hollow cylindrical tube with the outer radius ranging from  $r_1 = 0.144$  m (5.67 in) at the tip to  $r_2 = 0.216$  m (8.50 in) at the pole and uniform wall thickness  $t = 0.55$  cm (0.218 in), the moment of inertia  $I$  can be expressed as a function of the distance coordinate  $x$  follows:

$$r(x) = r_2 - \frac{(r_2 - r_1)}{L}x \quad (7.8)$$

$$I_x = \frac{\pi}{4} (r^4(x) - (r(x) - t)^4) \quad (7.9)$$

Double intergration of the curvature gives the mast-arm displacement

$$\frac{\partial^2 \psi(x)}{\partial x^2} = \frac{M}{EI} = \frac{w(L-x)^2}{2EI} \quad (7.10)$$

$$u_0 = \psi(L) = \int_0^L \int_0^L \frac{0.5W(L-x)^2}{EI} dx dx \quad (7.11)$$

where  $\psi(L)$  is the tip displacement. Using Matlab for numerical integration gives the following relationship between the tip displacement (in m) and the uniform load  $w$  (in N/m):

$$u_0(m) = \psi(L) = 1.824 \times 10^{-3} w(N/m) \quad (7.12)$$

in English units:

$$u_0(in) = \psi(L) = 1.05 \times 10^3 w(k/ft) \quad (7.13)$$

Noting that for a constant EI, having the properties of the mast arm at mid span  $r=(r_2+r_1)/2=0.18$  m (7.09 in),  $t=0.55$  cm (0.218 in).

$$I = \frac{\pi}{4}(r^4 - (r-t)^4) = 9.708 \times 10^{-5} m^4 (233.23 in^4) \quad (7.14)$$

$$u_0(m) = \frac{wL^4}{8EI} = 2.515 \times 10^{-3} w(N/m) \quad (7.15)$$

in English units:

$$u_0(in) = \psi(L) = 1.44 \times 10^3 w(k/ft) \quad (7.16)$$

The relation in Equation 7.15 (or equation 7.16) can serve as a "sanity check" for the Matlab value in Equation 7.12 (or equation 7.13). Hence knowing

the mast-arm tip displacement from the measured mast-arm tip acceleration, Equation 7.12 (or equation 7.13) can be use to determine uniform mast-arm load corresponding to the mast-arm tip displacement. Furthermore, the distributed load can then be used to determine the corresponding bending moment and stress range at the mast-arm/pole connection. Combining Equations 7.3 and 7.6 with the relation for the bending moment at the mast-arm/pole connection  $M = wL^2/2$ , the stress range becomes:

$$\Delta\sigma = 2 \times \sigma = 0.707 \frac{(w_v + w_h)L^2}{I} r_2 \quad (7.17)$$

Numerically gives  $\sigma(N/m^2) = 5.646 \times 10^5 (w_v + w_h)(N/m)$

or

$$(u_{0v} + u_{0h})(m) = 3.231 \times 10^{-9} \sigma(N/m^2) \quad (7.18)$$

in English units:

$$(u_{0v} + u_{0h})(in) = 0.88 \sigma(ksi) \quad (7.19)$$

- Case 2: Point load at the tip

For an assumed the point load of  $P$  (N), the moment in the mast-arm is  $M = (L - x) \times P$ , where  $x$  is the distance coordinate measured from the pole. Hence

$$u_0 = \psi(L) = \int_0^L \int_0^L \frac{(L - x)P}{EI} dx dx \quad (7.20)$$

where  $\psi(L)$  is the tip displacement. Using Matlab for numerical integration gives the following relationship between the tip displacement (in m) and the

point load  $P$  (in N):

$$u_0(m) = \psi(L) = 2.078 \times 10^{-4} P(N) \quad (7.21)$$

in English units:

$$u_0(in) = \psi(L) = 36.39 P(kips) \quad (7.22)$$

Noting that for a constant EI, having the properties of the mast arm at mid span  $r = (r_2 + r_1)/2 = 0.18$  m (7.09 in),  $t = 0.55$  cm (0.218 in).

$$I = \frac{\pi}{4} (r^4 - (r - t)^4) = 9.708 \times 10^{-5} m^4 (233.23 in^4) \quad (7.23)$$

$$u_0(m) = \frac{PL^3}{3EI} = 2.683 \times 10^{-4} P(N) \quad (7.24)$$

in English units:

$$u_0(in) = \psi(L) = 46.99 P(kips) \quad (7.25)$$

The relation in Equation 7.24 (or equation 7.25) can serve as a "sanity check" for the Matlab value in Equation 7.21 (or equation 7.22). Hence knowing the mast-arm tip displacement from the measured mast-arm tip acceleration, Equation 7.21 (or equation 7.22) can be use to determine the point load at the mast-arm tip corresponding to the mast-arm tip displacement. Furthermore, the point load can then be used to determined the corresponding bending moment and stress range at the mast-arm/pole connection. Combining Equations 7.3 and 7.6 with the relation for the bending moment at the mast-arm/pole connection  $M = PL$ , the stress range becomes:

$$\Delta\sigma = 2 \times \sigma = 1.414 \frac{(P_v + P_h)L}{I} r_2 \quad (7.26)$$

Numerically gives  $\sigma(N/m^2) = 4.517 \times 10^4 (P_v + P_h)(N)$

Or

$$(u_{0v} + u_{0h})(m) = 4.600 \times 10^{-9} \sigma(N/m^2) \quad (7.27)$$

in English units:

$$(u_{0v} + u_{0h})(in) = 1.25 \sigma(ksi) \quad (7.28)$$

Hence comparing Equation 7.18 (distributed uniform load) and 7.27 (point load), uniform load is more conservative case since the resulting stress for a given tip displacement is larger. Saying use  $(u_{0v} + u_{0h})(m) = 3.231 \times 10^{-9} \sigma(N/m^2)$  (in English units:  $(u_{0v} + u_{0h})(in) = 0.88 \sigma(ksi)$ ).

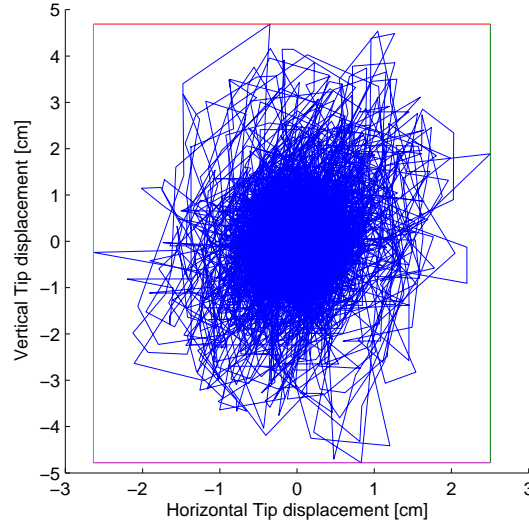


**Figure 7.6: Calculated Tip mast-arm motion for June 26, 2012 Data**

Figure 7.6 shows one example of displacement responses at the tip of the mast-arm during June 26, 2012. The response of the mast arm was quite high that day. Note that if the horizontal and vertical response were in phase, the mast arm tip motion would fall along a straight line going through the origin. This clearly is not the case. However Figure 7.6 suggests that the peak vertical displacement during this time period was about 4.8 cm, while the peak horizontal displacement was



about 2.4 cm. Herein we conservatively assume that the motion are in phase with  $u_{0h}=0.5u_{0v}$  leads to

$$u_{0v}(m) = 2.15 \times 10^{-9} \sigma(N/m^2) \quad (7.29)$$

## 7.4 Probability distribution for mast arm tip displacement

Fatigue life estimation requires information on the likely number of cycles for various stress ranges. This in turn requires the probability density function for the mast-arm tip displacement, particularly in the high displacement tail region. The best fit distribution of the mast-arm responses was established using the Inverse CDF method described in the Chapter 5. Figure 7.7 shows the best-fit distribution of the mast-arm tip displacement is an a Lognormal distribution with parameters  $\lambda=-0.91$  and  $\zeta=0.83$  as this distribution is closest to the 1:1 reference line. Figure 7.8

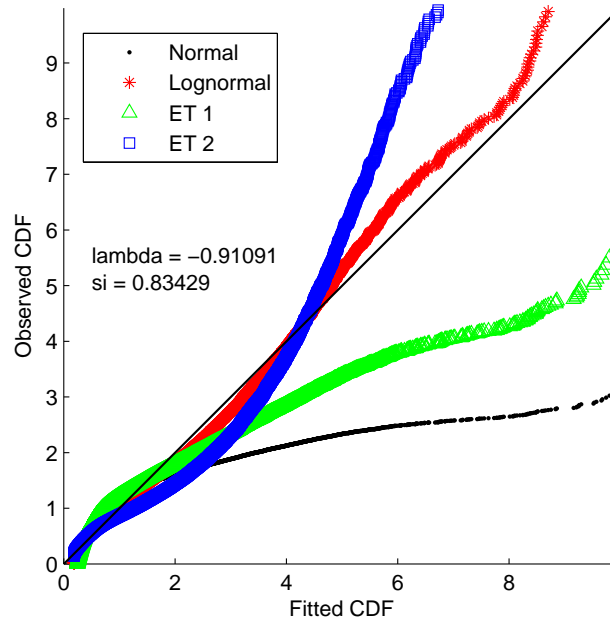


**Figure 7.7: Inverse CDF method**

shows the tip displacement cumulative histogram (for all 14 months data at Malta site) along with the corresponding Lognormal cumulative density function. Note the

reasonable fit of the Lognormal distribution to the actual histogram, particularly in the tail region.

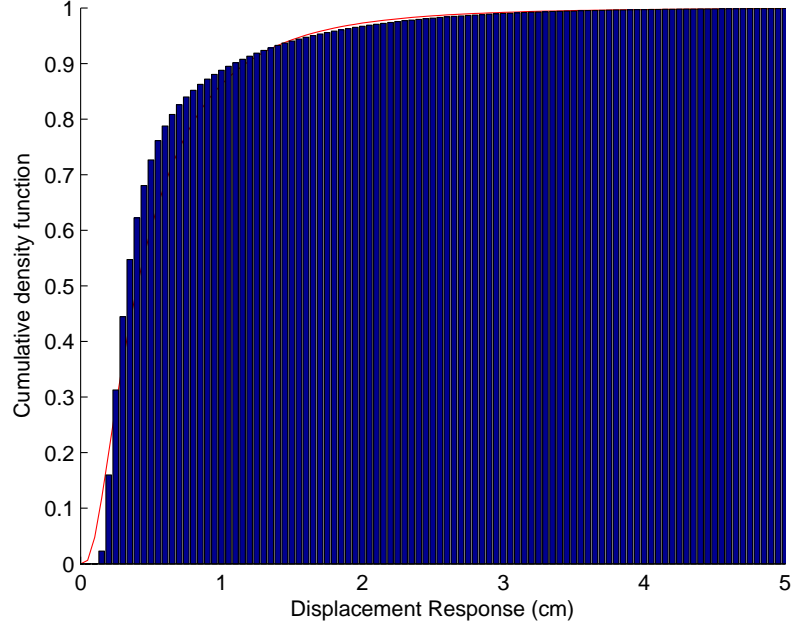


**Figure 7.8: Cumulative Histogram and Cumulative Density Function for tip displacement response**

## 7.5 Fatigue life estimation

The S-N curve characterizes the fatigue strength of a particular material. It can be used directly for situations in which the stress range is constant from cycle to cycle. For mast-arm vibration with different stress ranges from cycle to cycle, Miner's Rule can be used to estimate the fatigue life. Basically, Miner's Rule states that where there are  $k$  different stress ranges in a spectrum,  $S_i$  ( $1 \leq i \leq k$ ), each contributing  $n_i(S_i)$  cycles, and if  $N_i(S_i)$  is the number of cycles to failure for a constant stress range  $S_i$ , failure occurs when

$$\sum_{i=1}^k \frac{n_i}{N_i} = C \quad (7.30)$$

where  $C$  is experimentally determined constant typically between 0.7 and 2.2. Usually for design purposes,  $C$  is somewhat conservatively assumed to be 1.

For computational efficiency, the straight line between point A on the S-N curves for category E' (20 MPa (2.9 ksi)) and the maximum stress range point D (110 MPa (16 ksi)) in Figure 7.9 is replaced by three steps. The first step AB has a stress range varying from 20 MPa to 35.3 MPa (5.12 ksi) and it is represented by the mid point of 26.6 MPa (3.86 ksi) (log scale). The second step BC has a stress range varying from 35.3 MPa to 62.32 MPa (9.04 ksi) and it is represented by the mid point of 46.9 MPa (6.8 ksi) (log scale) while the last step CD has a stress range varying from 62.3 MPa to 110 MPa and is represented by the mid point of 82.8 MPa (12 ksi) (log scale)((as sketched in Figure 7.9). The number of cycles associated with the first step  $N_1$  is the value at the midpoint of the step or  $N_1 = 2.8 \times 10^6$  cycles as shown in Figure 7.1. The equivalent number of cycles for all three steps are presented in Table 7.1.

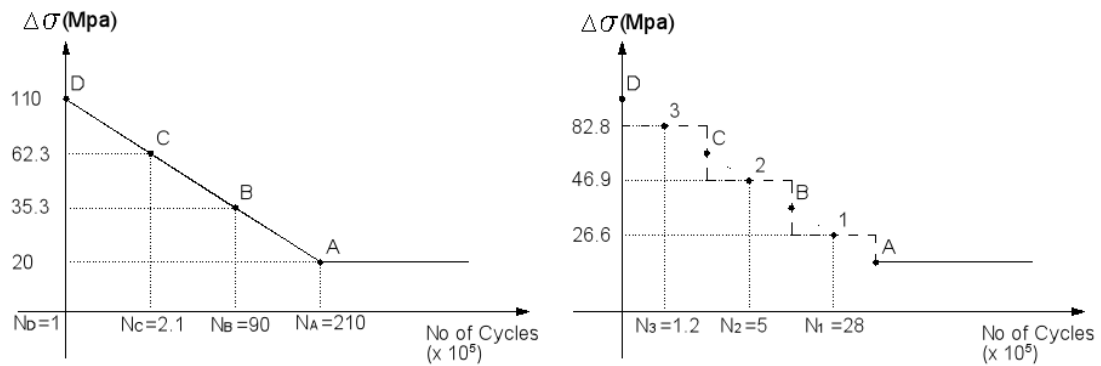


**Figure 7.9: Miner's Rule**

Based on the relationship between the stress range and the displacement at the tip above, gives the threshold tip displacement  $u_{0v}$ , for each value of stress range. Then the probability that the wind speed would cause a mast-arm response greater

**Table 7.1: Stress Range and Number of cycles Values**

Point	Stress Range [MPa]	$N_i$ Number of cycles [cycles]
Point A	20	$2.1 \times 10^7$
Point 1	26.6	$2.8 \times 10^6$
Point B	35.3	$0.9 \times 10^6$
Point 2	46.9	$5 \times 10^5$
Point C	62.3	$2.1 \times 10^5$
Point 3	82.8	$1.2 \times 10^5$
Point D	110	$1 \times 10^5$

than the threshold  $u_{0v}$  can be estimated by using Equation 7.31

$$P_{threshold} = P(u > u_{0v}) \quad (7.31)$$

where  $P(u > u_{0v})$  is the probability that the  $u$  (mast-arm tip displacement response) is greater than the threshold value  $u_{0v}$  which can be determined based on the Lognormal cumulative density function in Figure 7.7.

Since the natural frequency of the mast-arm is roughly 0.52 Hz (cycles per second) the corresponding natural period is  $\frac{1}{f_n} = T_n = 1.92(sec/cycle)$ . Hence the number of cycle per year is

$$N_{cycle} = \frac{(365days) \times (24hr/day) \times (60min/hr) \times (60sec/min)}{T_n} = 16.4 \times 10^6 cycles/year \quad (7.32)$$

The number of cycles per year that the response is greater than threshold (or the number of cycles associating with each stress range) is

$$n_i = N_{cycle} \times P_{threshold_i} \quad (7.33)$$

For example, point A, the stress range is  $\sigma_A=20$  MPa= $20 \times 10^6$  N/m<sup>2</sup>, using the Equation 7.29 gives  $u_{0v}=4.3$  cm. Then, the  $P_{threshold}$  can be calculated by

combining Equation 7.31 and the Lognormal cumulative density function with the parameters  $\lambda=-0.91$  and  $\xi=0.83$ .

$$P_{threshold} = P(u > u_{0v}) = 2.16 \times 10^{-3} \quad (7.34)$$

Finally, Equation 7.33 can be used to estimate  $n_i = 16.4 \times 10^6 \times 2.16 \times 10^{-3} = 3.54 \times 10^4$  (cycles). The results for other point is shown in Table 7.2.

**Table 7.2: Number of cycles associating with each stress range**

Section	$\Delta\sigma$ [MPa]	$N_i$ [cycles]	$u_{0v}$ [cm]	$P_{threshold}$	$n_{pointi}$ [cycles]
Point A	20	$2.1 \times 10^7$	4.3	$2.16 \times 10^{-3}$	$3.54 \times 10^4$
Point B	35.3	$0.9 \times 10^6$	7.6	$2.01 \times 10^{-4}$	$3.3 \times 10^3$
Point C	62.3	$2.1 \times 10^5$	13.4	$1.2 \times 10^{-5}$	198
Point D	110	$1 \times 10^5$	23.7	$4.6 \times 10^{-7}$	8

Finally, the number of cycles for stress ranges larger than point A but less than point B,  $n_1=n_A-n_B=3.21 \times 10^4$ , number of cycles for stress ranges larger than point B but less than point C,  $n_2=n_B-n_C=3.1 \times 10^3$  and number of cycles for stress ranges larger than point C but less than point D,  $n_3=n_C-n_D=190$ . These results are shown in Table 7.3.

**Table 7.3: Number of cycles associating with each equivalent step**

Section	$\Delta\sigma$ [MPa]	$N_i$ [cycles]	$n_i$ [cycles]
Section 1	26.6	$2.8 \times 10^6$	$3.21 \times 10^4$
Section 2	46.9	$5 \times 10^5$	$3.1 \times 10^3$
Section 3	82.8	$1.2 \times 10^5$	190

Assuming the fatigue life of the traffic signal is N (years), using the Miner's rules:

$$N \times \sum_{i=1}^n \frac{n_i}{N_i} = 1 \quad (7.35)$$

gives N=52 years

## 7.6 Conclusion

The estimation of fatigue life of this traffic signal structure is 52 years. Note that in this estimation is based on a number of conservative assumptions that the horizontal and vertical motions were exactly in phase). Moreover, the Miner's Rule with  $C=1.0$  is known to be somewhat conservative. Hence fatigue life of the structure is something in exceed of 52 years and fatigue will not be a problem for the Malta traffic signal. Also this approach does not account for significant large amplitude motion induced by vortex shedding because it was not observed in this case due to the high turbulence in the approach flow.

## LITERATURE CITED

- [1] NYSDOT, “Determining remaining fatigue life of in-situ mast-arm traffic signal structures,” 2010, Request for Proposals SPR No. C-10-07.
- [2] K. W. Johns and R. J. Dexter, “The development of fatigue design load ranges for cantilevered sign and signal support structures,” *J. of Wind Eng. and Ind. Aerodynamics*, vol. 77-78, pp. 315–326, 1998.
- [3] B. A. Hartnagel and M. G. Barker, “Strain measurements on traffic signal mast arms,” in *1999 New Orleans Structures Congr.*, New Orleans, LA, 1999.
- [4] G. Chen, J. Wu, J. Yu, L. R. Dharani, and M. Baker, “Fatigue assessment of traffic signal mast arms based on field test data under natural wind gusts,” *Transportation Research Rec.: J. of the Transportation Research Board*, pp. 188–94, 2001.
- [5] G. Chen, M. Barker, L. R. Dharani, and C. Ramsay, “Signal mast arm fatigue failure investigation,” Missouri Dept. of Transportation, Tech. Rep., 2003.
- [6] H. R. Hamilton, III, G. S. Riggs, and J. A. Puckett, “Increased damping in cantilevered traffic signal structures,” *J. of Structural Eng.*, pp. 530–537, 2000.
- [7] AASHTO, *Standard Specifications for Structural Supports to Highway Signs, Luminaires, and Traffic Signals*. Amer. Assoc. of State Highway and Transportation Officials, 2009.
- [8] J. D. Holmes, *Wind Loading of Structures*. New York: Taylor and Francis, 2007.
- [9] C. Letchford, H. Cruzado, and D. Zuo, “Full-scale controlled tests of wind loads on traffic signal structures,” Texas Dept. of Transportation, Austin, TX, Tech. Rep., 2008.
- [10] J. Hua and D. Zuo, “Wind-induced vibration of mast arm traffic signal support structure of various configurations,” in *3rd Amer. Assoc. for Wind Eng. Workshop*, Hyannis, MA, 2012.
- [11] Google, “Map of Malta, NY,” 2013, Retrieved on April 02, 2013. [Online]. Available: <http://www.maps.google.com>
- [12] T. P. Products, “Traffic signal standards “TR” Series,” 2013.

- [13] A. K. Chopra, *Dynamics of Structures*. Upper Saddle River, NJ: Pearson Prentice Hall, 2007.
- [14] W. D. Callister Jr. and D. G. Rethwisch, *Fundamentals of Materials Science and Engineering*. John Wiley and Sons, 2008.
- [15] H. Nguyen Sinh and C. Letchford, “Long-term spectra of mean wind speeds for wind climate simulation,” in *12th Americas Conf. on Wind Eng.*, Seattle, WA, to be published 2013.
- [16] ASCE, *Minimum Design Loads for Buildings and Other Structures*. Reston, VA: Amer. Soc. of Civil Eng., 2010.
- [17] Google, “Map of Lubbock, TX,” 2013, Retrieved on April 02, 2013. [Online]. Available: <http://www.maps.google.com>
- [18] J. Hua, “RE: Hi from Jieying Hua (Texas Tech Univ.),” Personal E-mail (Mar. 4, 2013).
- [19] R. D. Blevins, *Formulas For Natural Frequency and Mode Shape*. New York: Van Nostrand Reinhold Company, 1979.
- [20] ]. National Oceanic and Atmospheric Administration, Department of Defense, Federal Aviation Administration, United States Navy (1998) , “Automated Surface Observing System (ASOS) Users Guide ”.
- [21] Benjamin, J.R., and C.A. Cornell, *Probability, statistics and decision for civil engineers*. McGraw-Hill, New York, 1970.



**APPENDIX A**  
**NYSDOT PLANS - MALTA, NY MAST-ARM**  
**STRUCTURE**

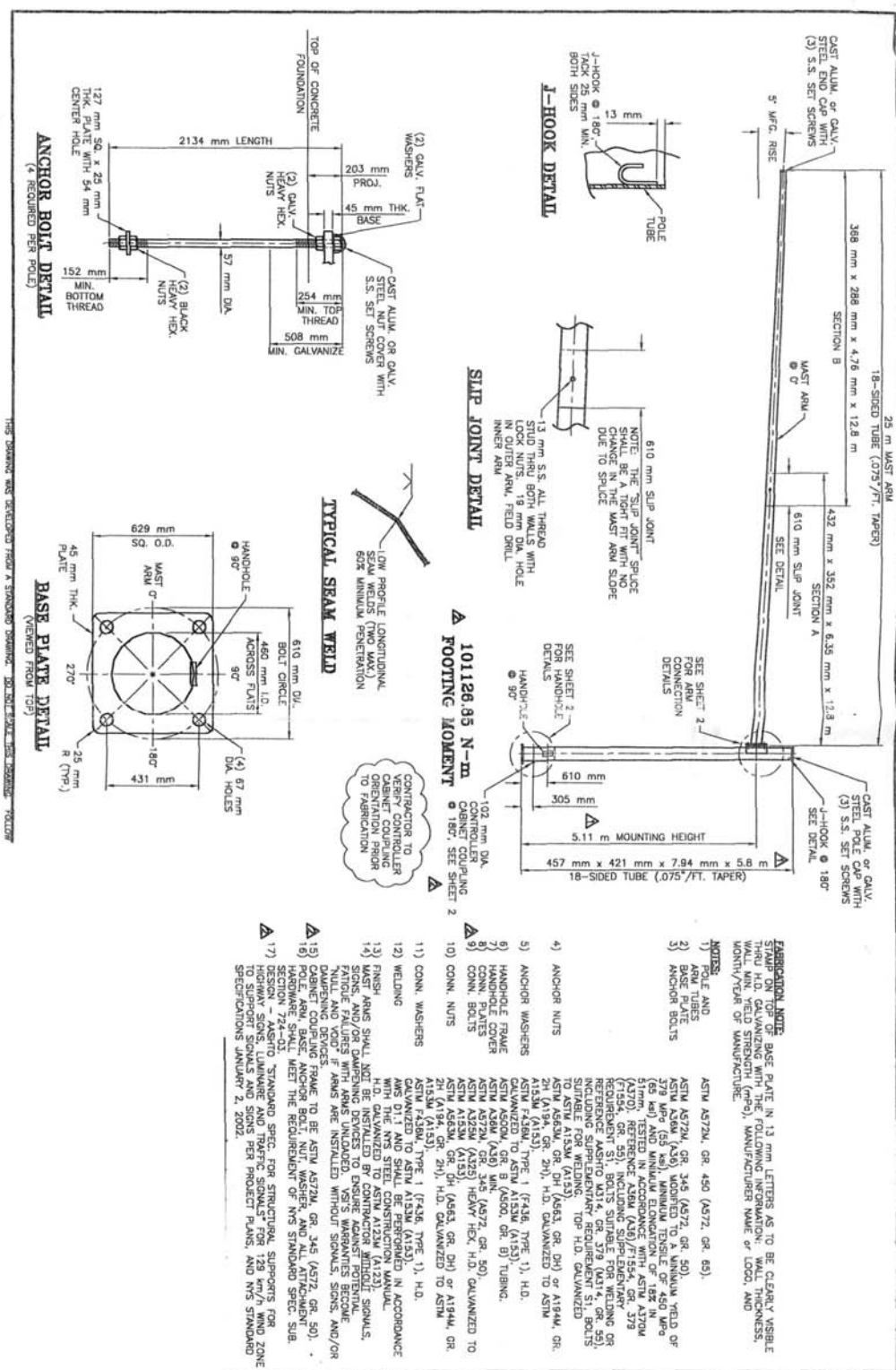


Figure A.1: NYSDOT Plans (1 of 3)

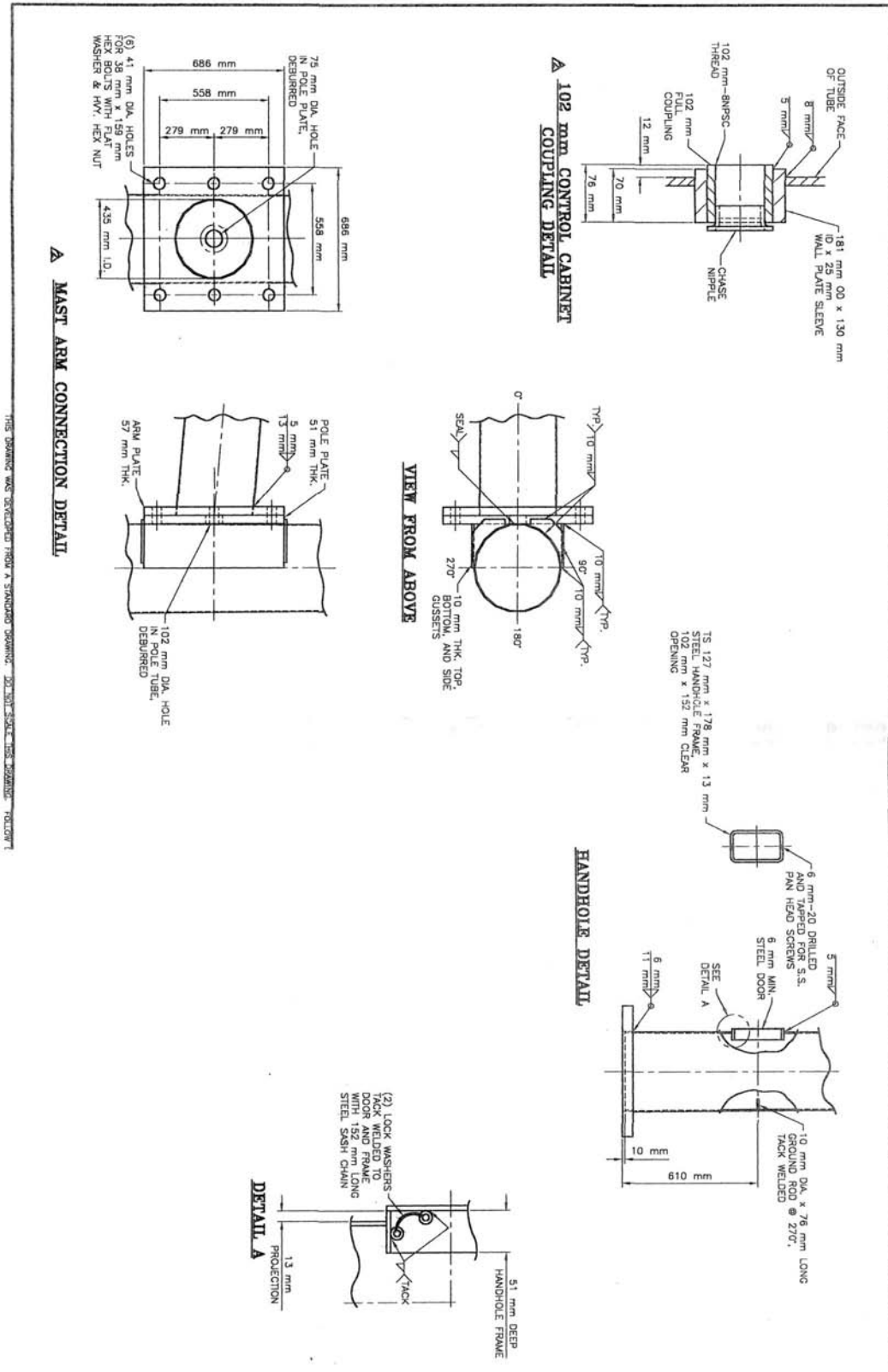


Figure A.2: NYSDOT Plans (2 of 3)

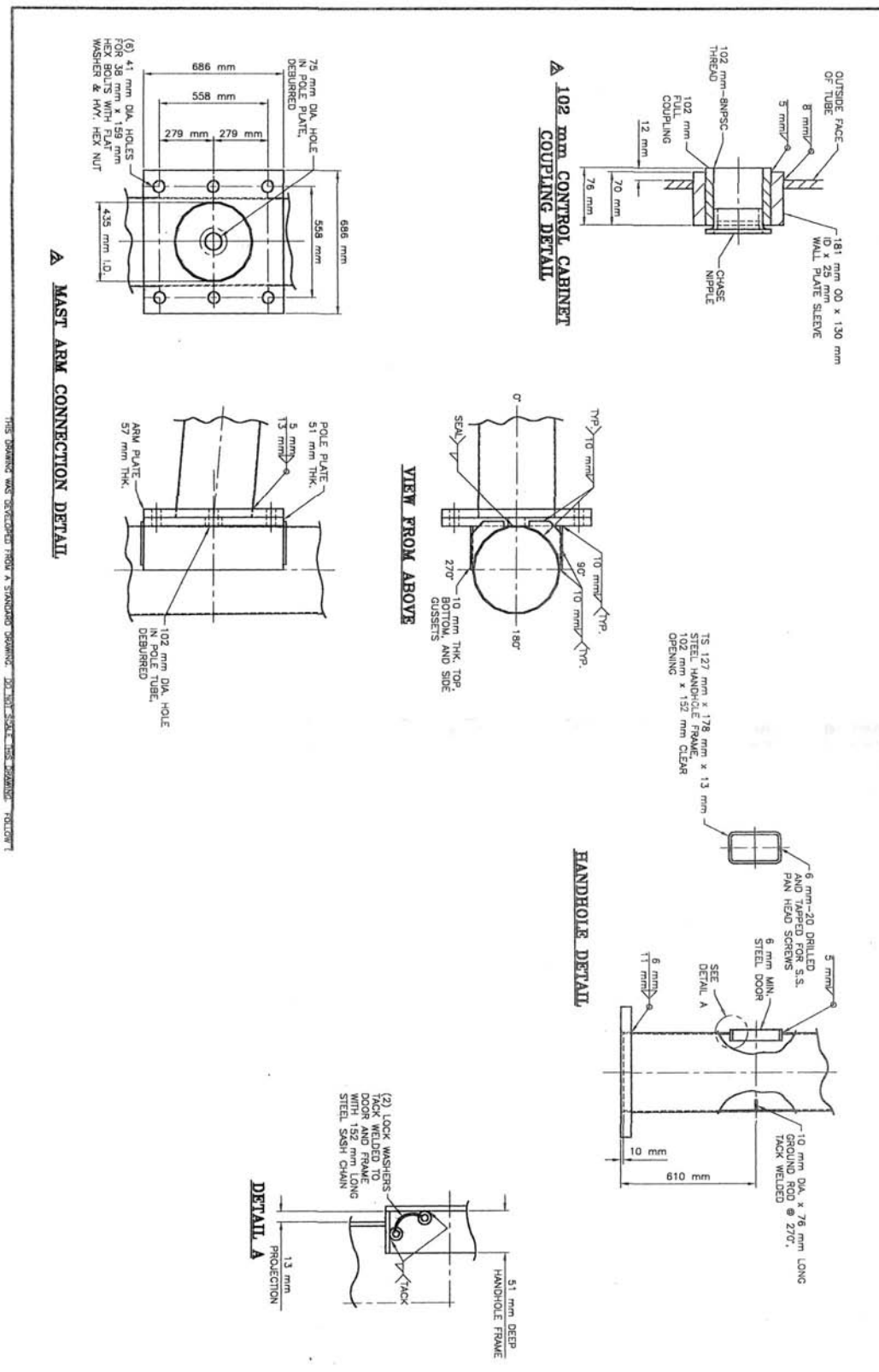


Figure A.3: NYSDOT Plans (3 of 3)

## APPENDIX B

### NATURAL FREQUENCY HAND CALCULATIONS

#### Model Properties:

$\rho$  - Material Density  $[kg/m^3] = 7850 [kg/m^3]$

$E$  - Young's Modulus  $[GPa] = 200 [GPa]$

$r_o$  - Average Outer Radius of Mast Arm  $[m] = 0.18 [m]$

$r_i$  - Average Inner Radius of Mast Arm  $[m] = 0.17445 [m]$

$L$  - Length of Mast Arm  $[m] = 25 [m]$

#### Approximation method

$$a_o = \pi(r_o^2 - r_i^2)$$

$$i_o = \pi/4(r_o^4 - r_i^4)$$

$$m_o = \frac{\rho a_o}{g}$$

$\lambda$  - see figure B.1

The natural frequency for Clamped-Free Beam with Double Linear Taper and Truncated End [19] can be expressed as following equation:

$$f_i = \frac{\lambda_i^2}{2\pi L^2} \left( \frac{ei_o}{m_o} \right)^{1/2} \quad (B.1)$$

Following the above procedure, hand calculations yield an estimated fundamental frequency of 0.76 Hz for the Malta, NY mast-arm. The corresponding natural frequency obtained from the FEM analysis is 0.74 Hz (a 2.4% difference). This close comparison provided an initial validation for the finite element model.

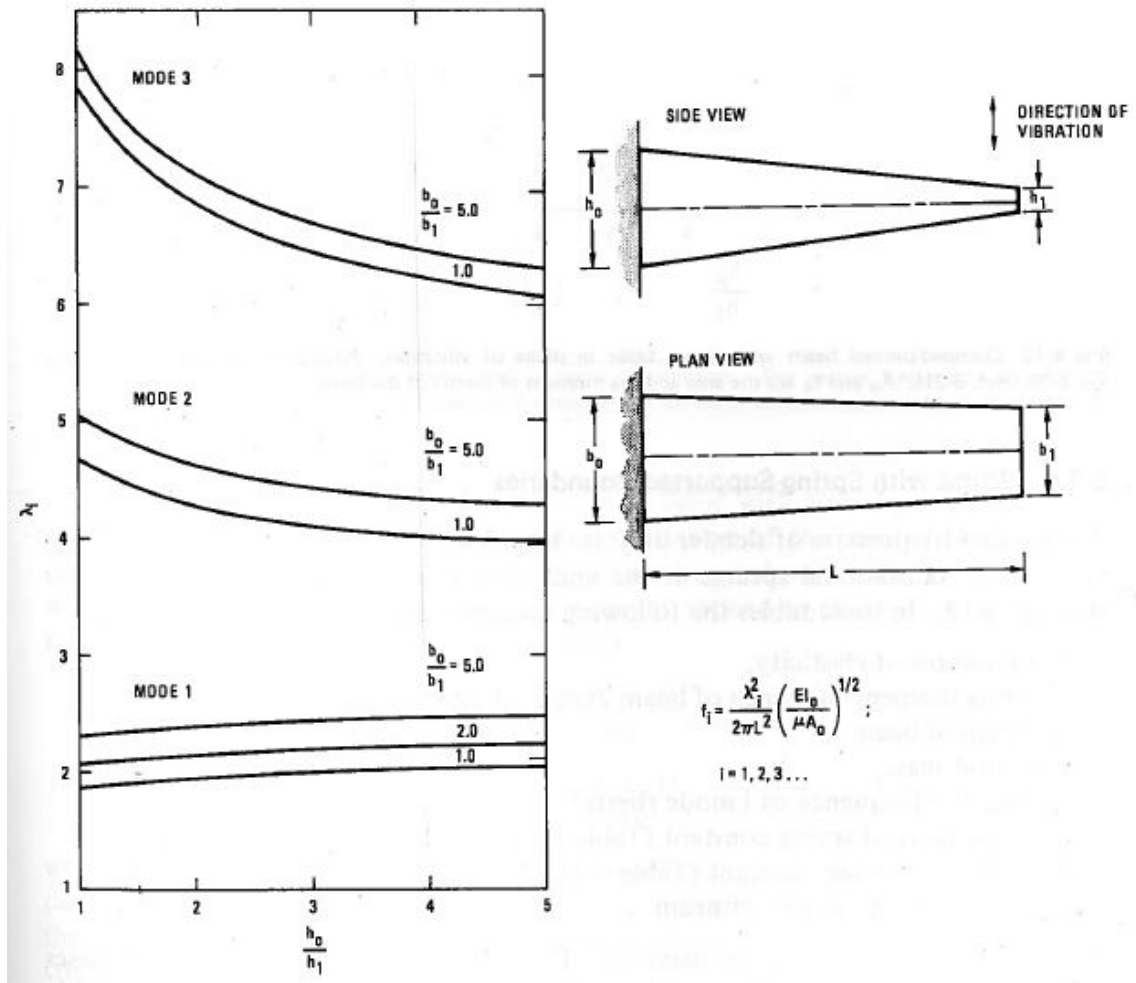


Figure B.1: Lambda Values: Clamped-Free Beam with Double Linear Taper and Truncated End [19]

### Rayleigh's methods

$$I_x = \frac{\pi(r_o^4 - r_i^4)}{4}$$

$$m_x = \frac{\rho(r_o^2 - r_i^2)\pi}{2}$$

$$\psi(x) = \frac{W}{24EI}(x^4 - 4L^3x + 3L^4)$$

$$\omega_n^2 = \frac{\int_0^L \frac{1}{2}EI(x)[z_0\psi''(x)]^2 dx}{\int_0^L \frac{1}{2}m(x)[z_0\omega_n\psi(x)]^2 dx + \sum_{i=1}^N \frac{1}{2}M_i(x)[z_0\omega_n\psi(x_i)]^2} \quad (\text{B.2})$$

$M_i$  and  $x_i$  - See Table 3.2

$$f_n = \frac{\omega_n}{2\pi} \quad (\text{B.3})$$

Following the above procedure, using Matlab for numerical intergration gives:

$$\int_0^L \frac{1}{2} EI(x) [z_0 \psi''(x)]^2 dx = 2,848.1 z_0 (Nm)$$

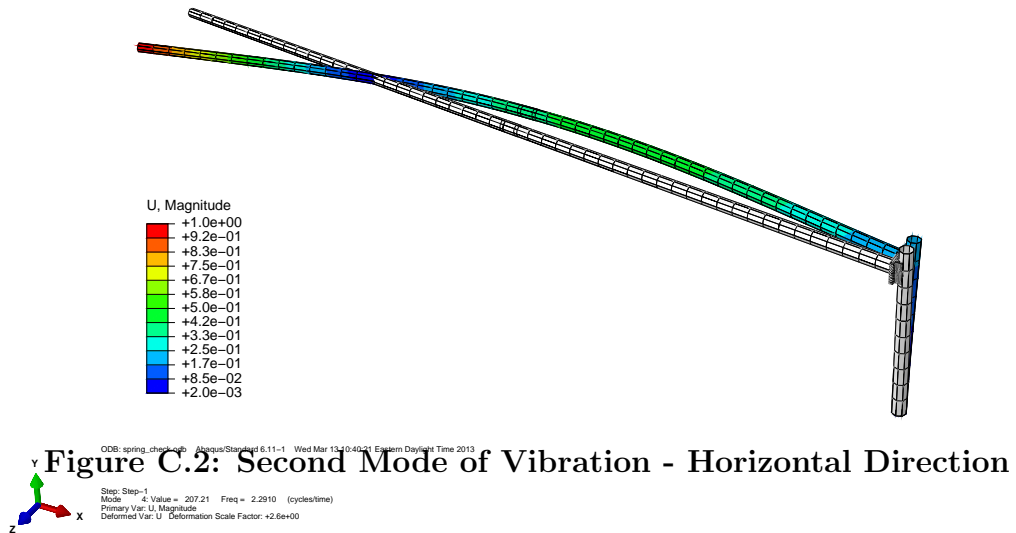
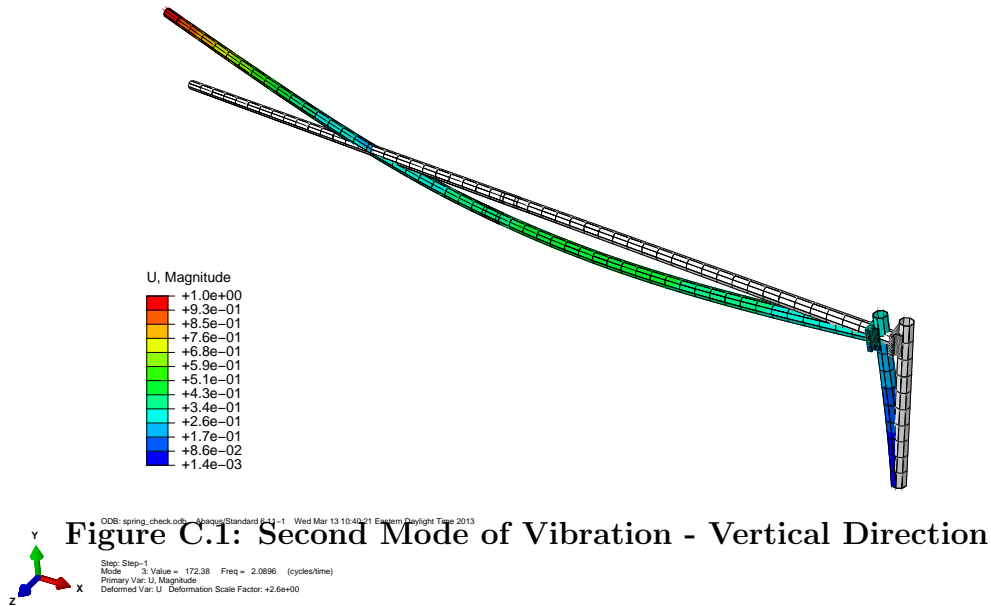
$$\int_0^L \frac{1}{2} m(x) [z_0 \omega_n \psi(x)]^2 dx = 223.08 z_0 (Nm)$$

$$\sum_{i=1}^N \frac{1}{2} M_i(x) [z_0 \omega_n \psi(x_i)]^2 = 15.23 z_0 (Nm)$$

Hence  $\omega_n = 3.457$  (rad/s) yields an estimated fundamental frequency of 0.55 Hz for the Malta, NY mast-arm.

# APPENDIX C

## DYNAMIC CHARACTERISTICS - ADDITIONAL FIGURES





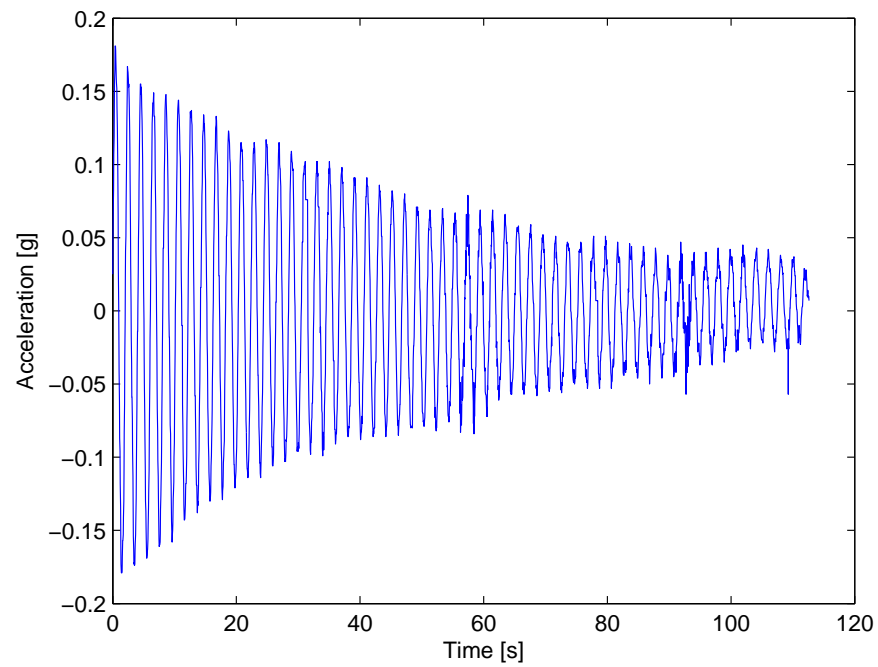
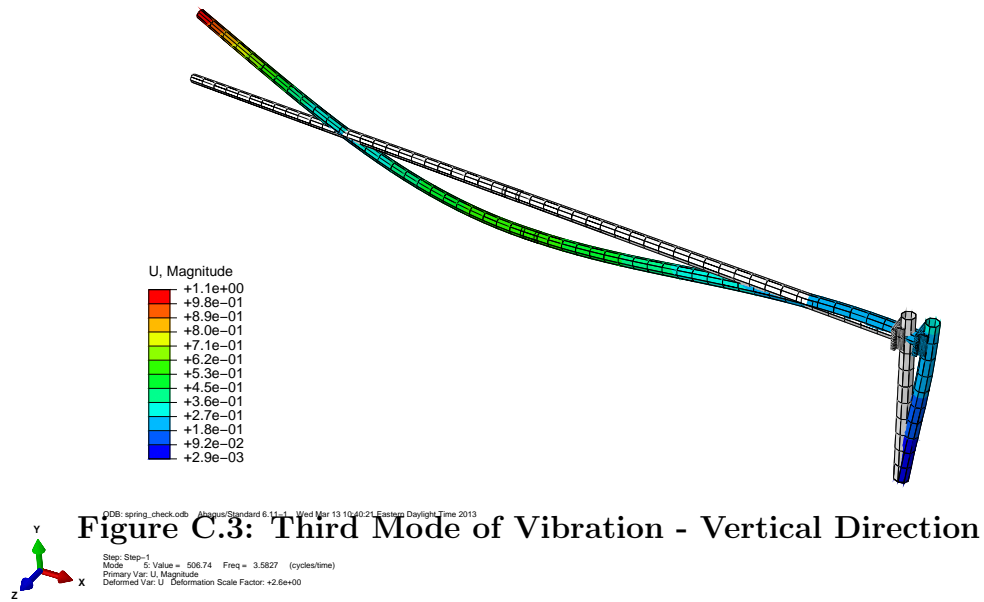


Figure C.4: Pluck Test (Y-Direction, Test 1): Acceleration Time History

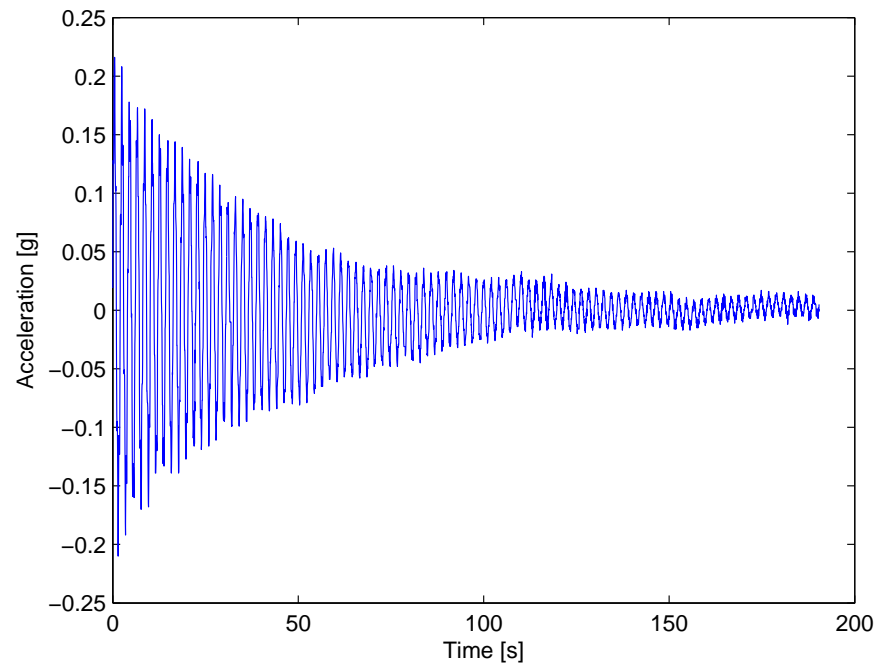


Figure C.5: Pluck Test (Y-Direction, Test 2): Acceleration Time History

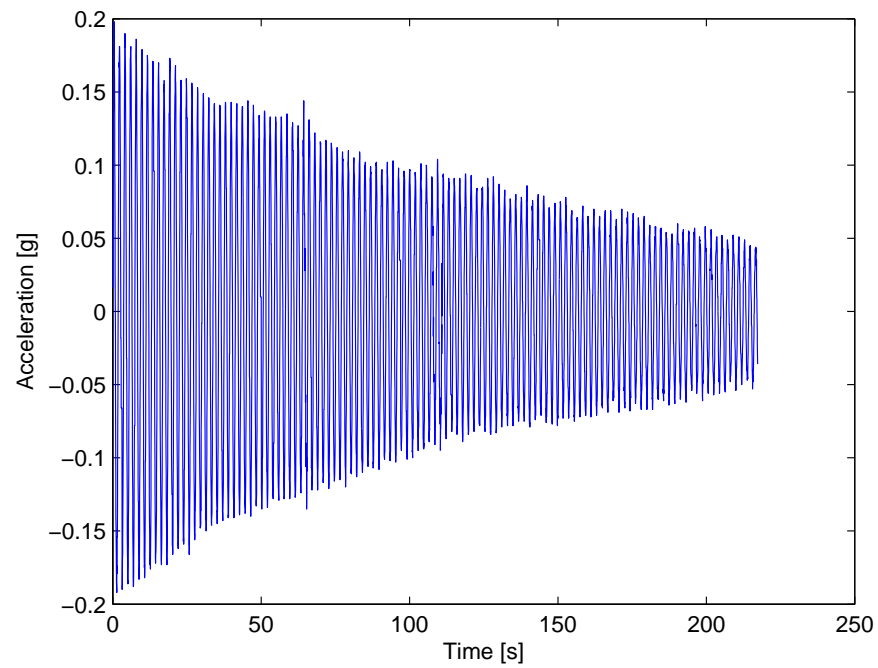


Figure C.6: Pluck Test (Z-Direction, Test 1): Acceleration Time History

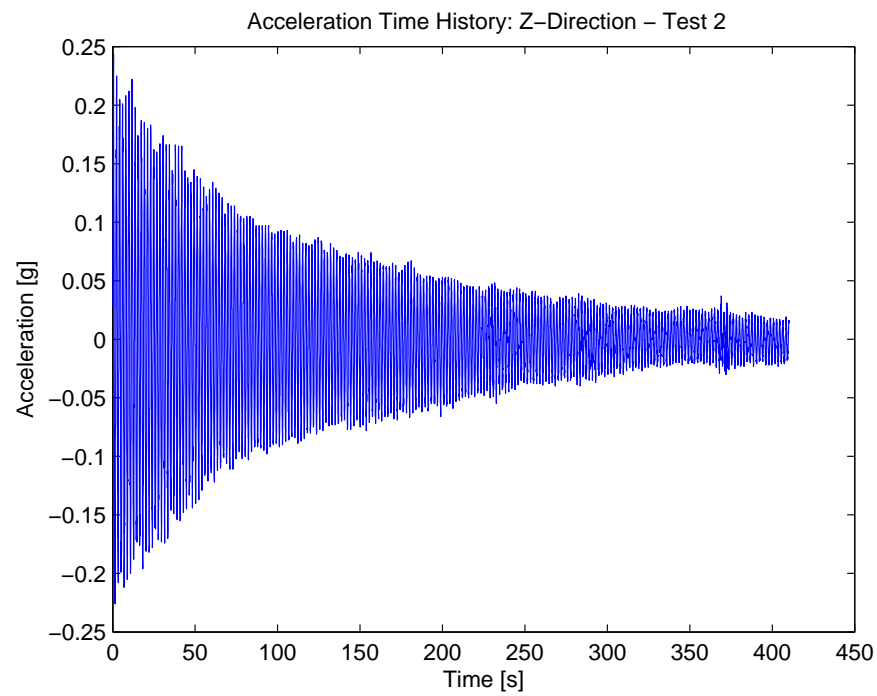


Figure C.7: Pluck Test (Z-Direction, Test 2): Acceleration Time History

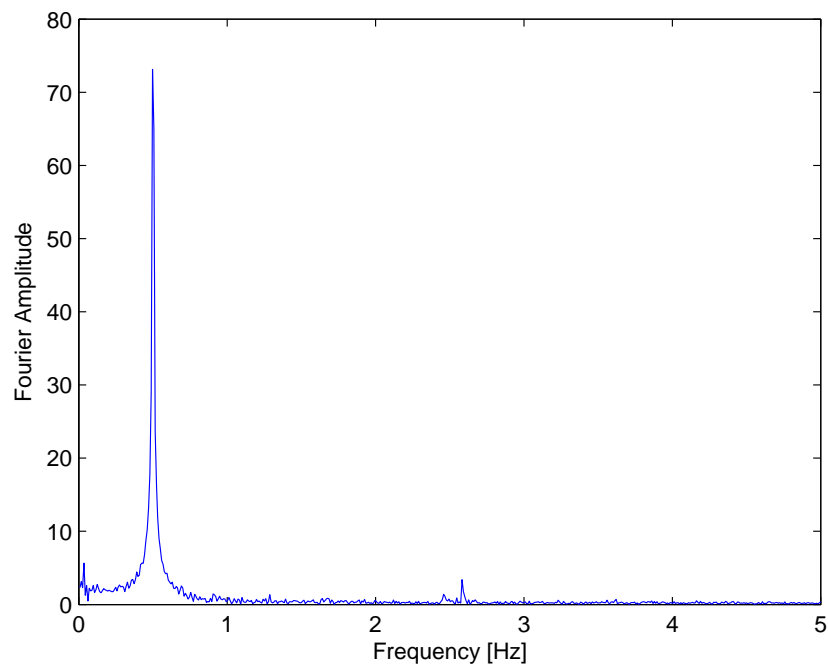
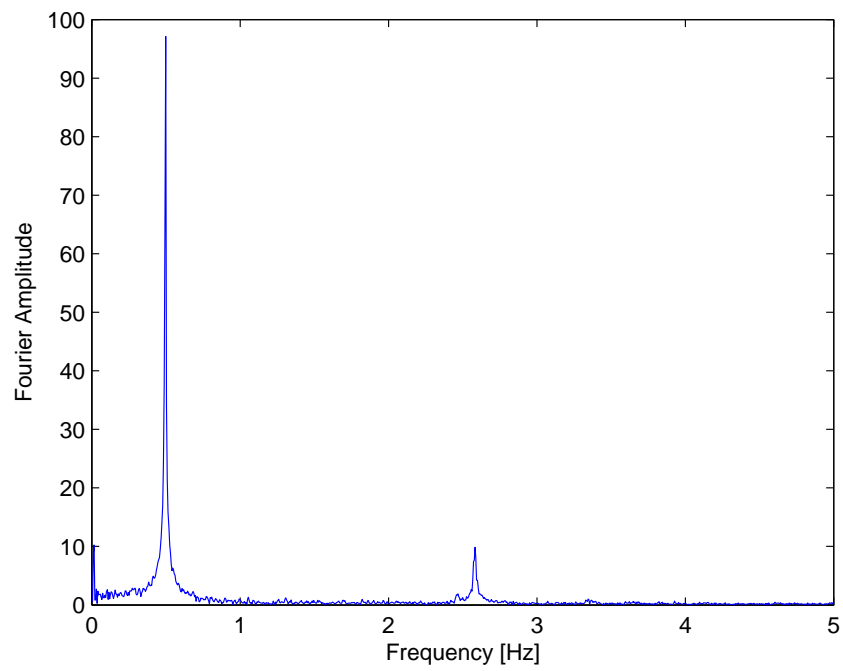
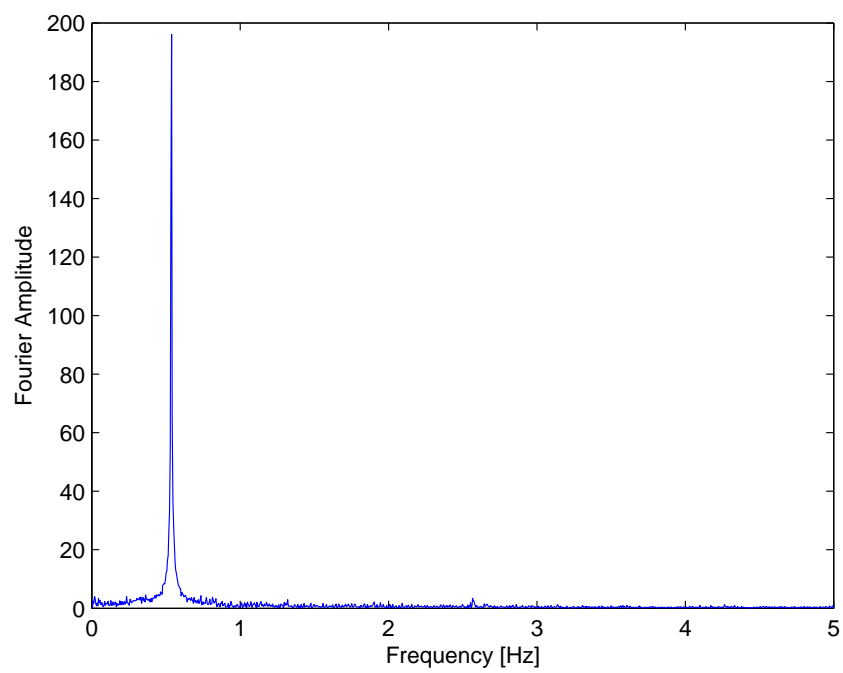


Figure C.8: Pluck Test (Y-Direction, Test 1): Fourier Amplitude Spectrum



**Figure C.9: Pluck Test (Y-Direction, Test 2): Fourier Amplitude Spectrum**



**Figure C.10: Pluck Test (Z-Direction, Test 1): Fourier Amplitude Spectrum**

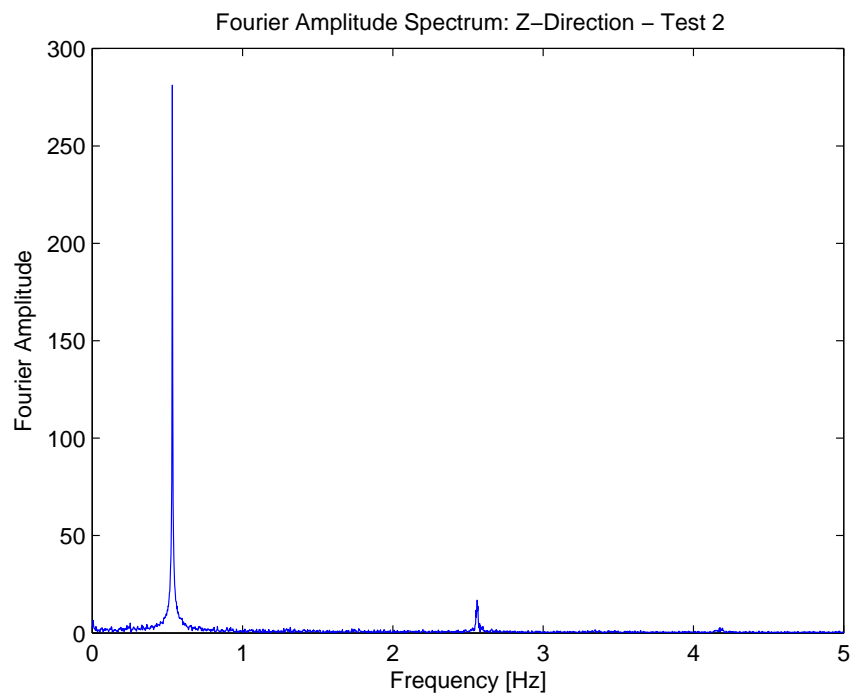


**Figure C.11: Pluck Test (Z-Direction, Test 2): Fourier Amplitude Spectrum**

# APPENDIX D

## WIND ROSES USING NCDC DATA

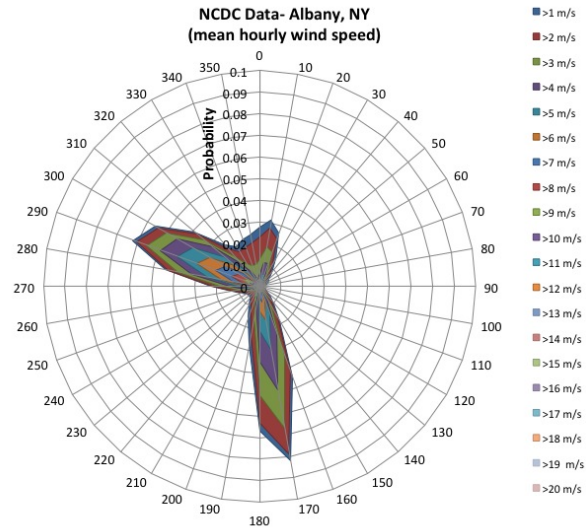


Figure D.1: Observed Wind Rose for Albany, NY

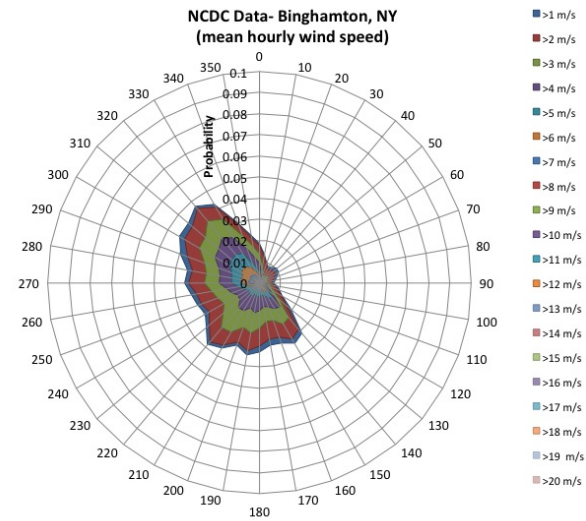


Figure D.2: Observed Wind Rose for Binghamton, NY

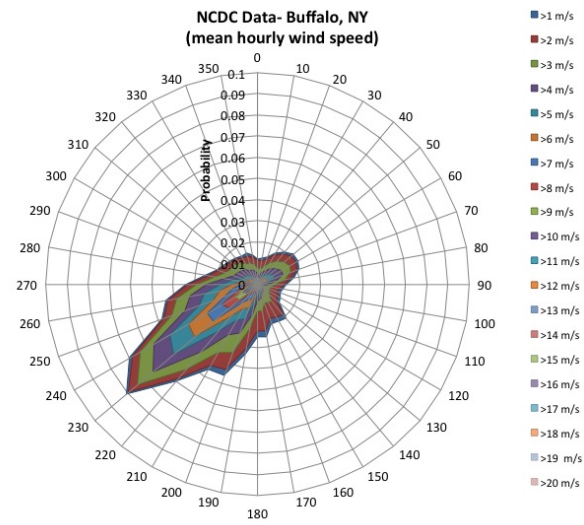


Figure D.3: Observed Wind Rose for Buffalo, NY

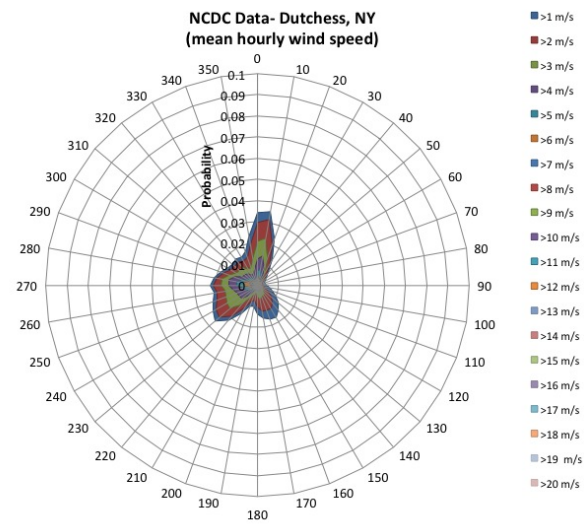


Figure D.4: Observed Wind Rose for Dutchess, NY

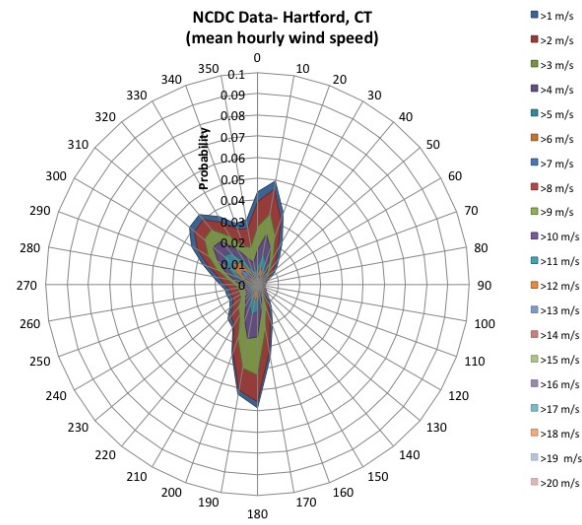


Figure D.5: Observed Wind Rose for Hartford, CT

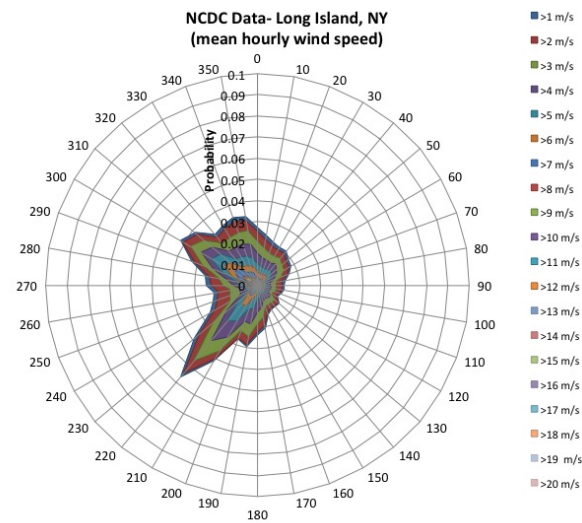


Figure D.6: Observed Wind Rose for Long Island, NY



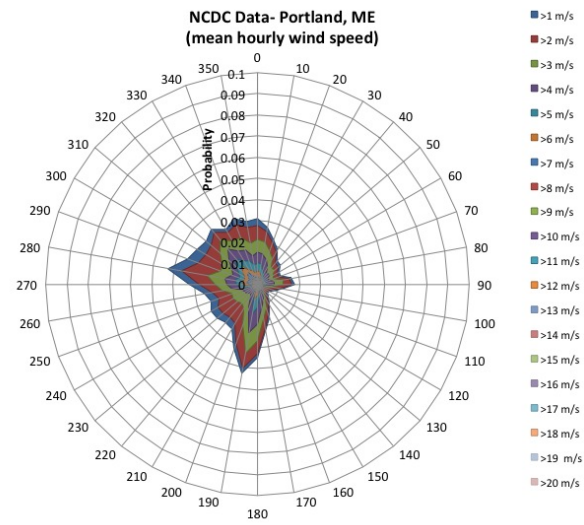


Figure D.7: Observed Wind Rose for Portland, ME

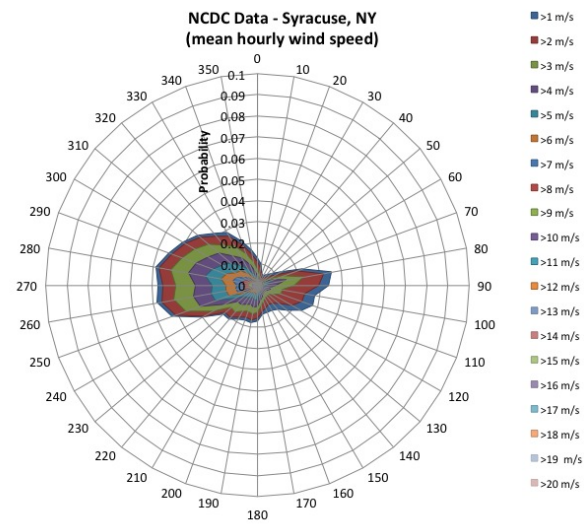


Figure D.8: Observed Wind Rose for Syracuse, NY

## APPENDIX E

### WIND ROSES USING BEST FIT WEIBULL MODEL

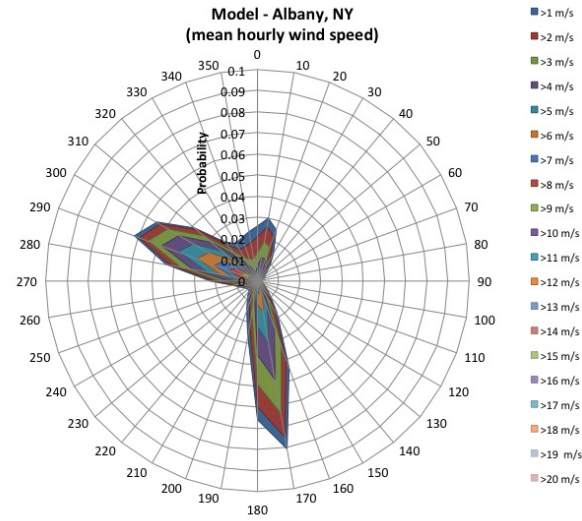


Figure E.1: Model Wind Rose for Albany, NY

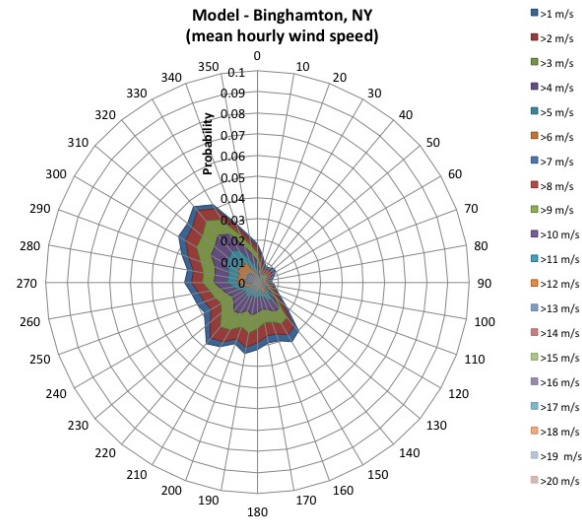


Figure E.2: Model Wind Rose for Binghamton, NY

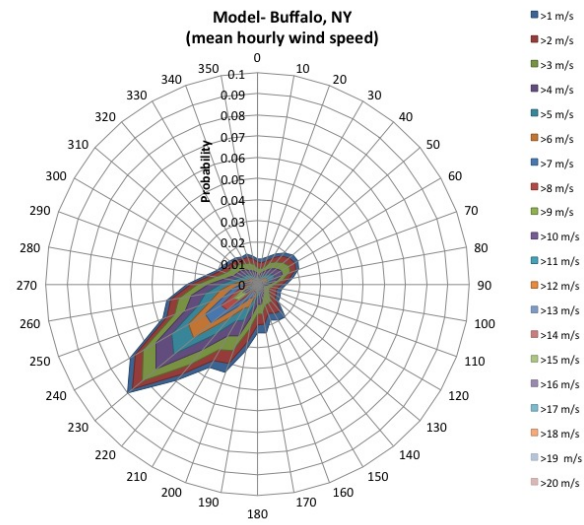


Figure E.3: Model Wind Rose for Buffalo, NY

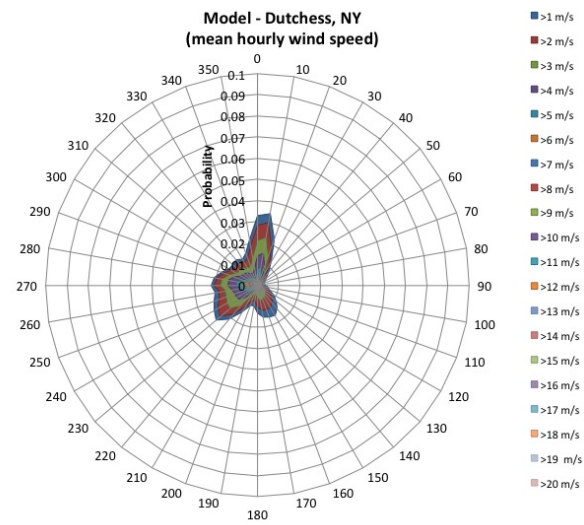


Figure E.4: Model Wind Rose for Dutchess, NY

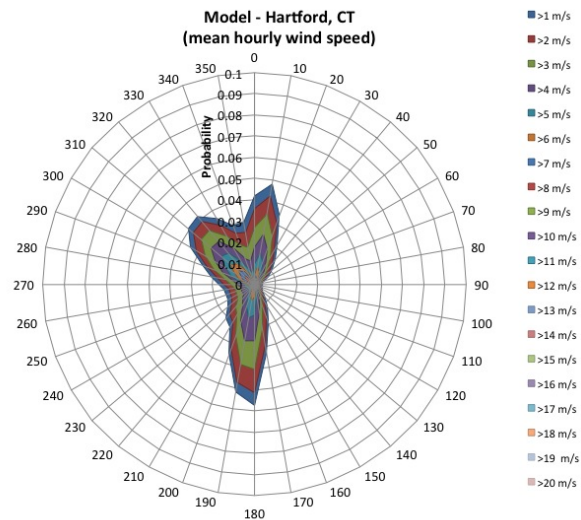


Figure E.5: Model Wind Rose for Hartford, CT

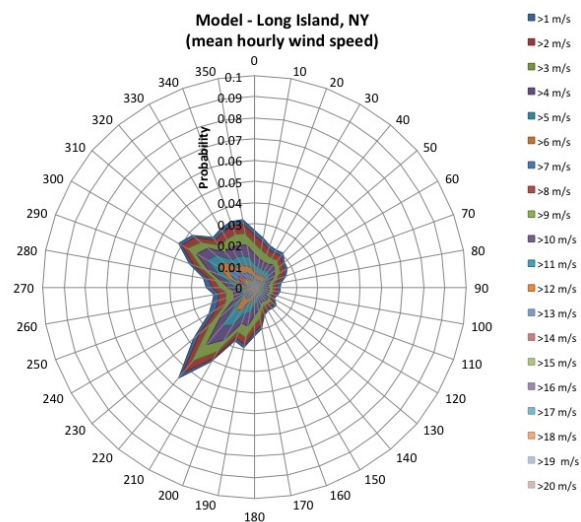


Figure E.6: Model Wind Rose for Long Island, NY

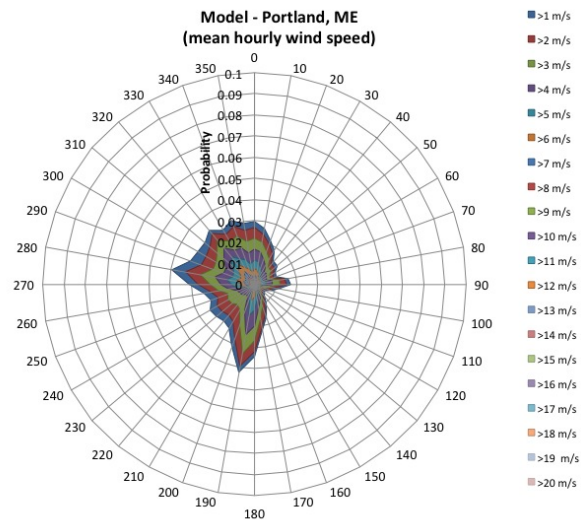


Figure E.7: Model Wind Rose for Portland, ME

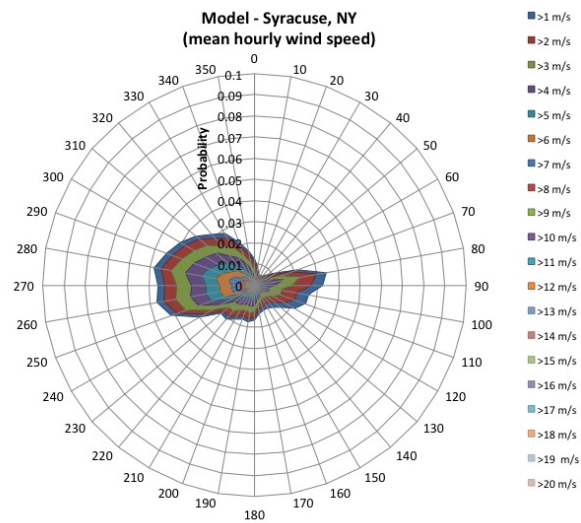


Figure E.8: Model Wind Rose for Syracuse, NY

## APPENDIX F

### CIRCULAR AVERAGE FORMULATION

Note: **Bold** type setting indicates a vector of values

$\Theta$  is a vector containing n seconds of azimuth angle data [units = radians]

$$\Theta_x = \sin(\Theta)$$

$$\Theta_y = \cos(\Theta)$$

$$\bar{\Theta}_x = \text{mean}(\Theta_x)$$

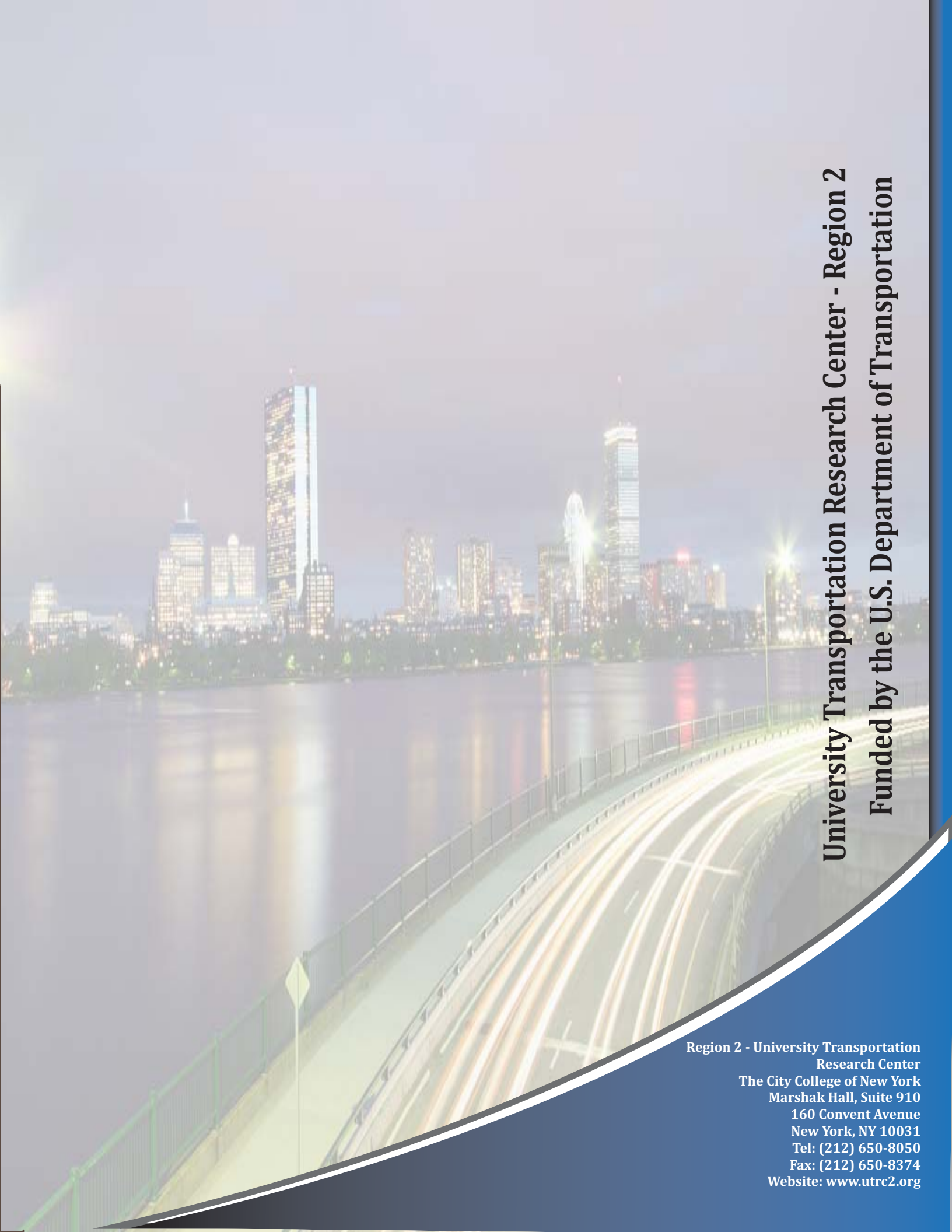
$$\bar{\Theta}_y = \text{mean}(\Theta_y)$$

$$\bar{\Theta}_* = \tan^{-1}(\bar{\Theta}_x/\bar{\Theta}_y)$$

$$\text{if } \bar{\Theta}_y < 0 : \bar{\Theta} = \bar{\Theta}_* + 180$$

$$\text{if } \bar{\Theta}_* < 0 : \bar{\Theta} = \bar{\Theta}_* + 360$$

$$\text{otherwise } \bar{\Theta} = \bar{\Theta}_*$$



# University Transportation Research Center - Region 2

## Funded by the U.S. Department of Transportation

Region 2 - University Transportation  
Research Center  
The City College of New York  
Marshak Hall, Suite 910  
160 Convent Avenue  
New York, NY 10031  
Tel: (212) 650-8050  
Fax: (212) 650-8374  
Website: [www.utrc2.org](http://www.utrc2.org)